Topological Analysis of the Grain Boundary Space

by

Srikanth Patala

B. Tech. Metallurgical and Materials Engineering
Indian Institute of Technology Madras, 2005

S.M. Materials Science and Engineering
Massachusetts Institute of Technology, 2008

SUBMITTED TO THE DEPARTMENT OF MATERIALS SCIENCE & ENGINEERING IN
PARTIAL FULFILLMENT OF THE REQUIREMENTS FOR THE DEGREE OF

DOCTOR OF PHILOSOPHY IN MATERIALS SCIENCE & ENGINEERING
AT THE
MASSACHUSETTS INSTITUTE OF TECHNOLOGY

JUNE 2011

Signature of Author: _____

Department of Materials Science & Engineering
May 20, 2011

Certified by: _____

Christopher A. Schuh
Danae and Vasilios Salapatas Associate Professor of Metallurgy
Thesis Supervisor

Accepted by: _____

Christopher A. Schuh
Danae and Vasilios Salapatas Associate Professor of Metallurgy
Chair, Department Committee on Graduate Students

Topological Analysis of the Grain Boundary Space

by

Srikanth Patala

Submitted to the Department of Materials Science & Engineering on May 20, 2011 in Partial Fulfillment of the Requirements for the Degree of Doctor of Philosophy in Materials Science & Engineering

ABSTRACT

Grain boundaries and their networks have a profound influence on the functional and structural properties of every class of polycrystalline materials and play a critical role in structural evolution and phase transformations. Recent experimental advances enable a full crystallographic characterization, including the boundary misorientation and inclination parameters, of grain boundaries. Despite these advances, a lack of appropriate analytical tools severely undermines our ability to analyze and exploit the full potential of the vast amounts of experimental data available to materials scientists. This is because the topology of the grain boundary space is unknown and even a well-studied part of the complete grain boundary space, the misorientation space, is relatively poorly understood. This thesis summarizes efforts to improve the representation of misorientation information and to understand the topology of the complete grain boundary space. First, the topology of the space of misorientations is discussed with a focus on the effect of symmetries on the minimum embedding dimensions in Euclidean space. This opens the door to a new method of representation of misorientation information in which grain boundaries can be uniquely colored by their misorientations. Second, conditions under which the topology of the grain boundary space has been resolved are presented. Resolving the topology of the complete grain boundary space not only facilitates statistical analysis of grain boundaries, but can also help describe the structure-property relationships of these interfaces.

Thesis Supervisor: Christopher A. Schuh

Title: Danae and Vasilios Salapatas Professor of Metallurgy

Acknowledgements

I am extremely grateful to the many wonderful people I have met during my time here, without whom this thesis would not have been possible. I would like to begin by expressing my heartfelt gratitude to my advisor, Professor Christopher Schuh, who is one of the most dedicated and hard-working people I have ever met. He has been an excellent mentor and a constant source of energy, ideas, and enthusiasm. I cannot thank him enough for the support he has given me and for his patience as I worked through this thesis.

I would also like to thank the members of my thesis committee for their time and many suggestions: Professors Samuel Allen, Carl Thompson, and David Parks. Throughout my graduate career, Professor Allen has always been there to help me and give me the direction I needed, and for that I am very grateful. I am also extremely grateful to Professor Thompson for all the comments and suggestions that helped me make my work more intuitive and practical.

I would like to thank all the members of the Schuh Research Group for their help during my time at MIT. I owe a great deal to Dr. Jeremy Mason for helpful discussions; his guidance in the initial stages of this project has been invaluable. I am extremely grateful for his invitation to the Institute of Advanced Study at Princeton to share my work. I also thank Dr. Koichi Kita, another past member of the Schuh Research Group, for providing me with the experimental EBSD data. Special thanks are owed to Eric Homer and Tiffany Ziebell, who reviewed manuscripts and gave insightful comments. Dr. Stuart I. Wright from EDAX-TSL Inc. has helped me incorporate some of my code into the commercial OIM^{TM} Analysis software.

Graduate school would not have been the same without the amazing people whom I was fortunate enough to meet and become friends with at MIT. My roommates, Sukant Mittal, Dipanjan Sen, and Vivek Sharma, were always there when I needed their help and made my experiences at MIT very enjoyable. They created one of the most friendly and relaxed environments that I could hope for. Special thanks are owed to Dipanjan for helping me prepare for my qualifying exams. I am grateful to Vilsa Curto for all her support over the last year and for her help with editing innumerable documents. I would also like to thank one of my closest friends, Srujan Linga, with whom I had many memorable moments and who still remains a constant source of encouragement. There are many others, whose names I will not be able to mention due to limited space, who helped me finish this thesis.

Finally, this thesis is dedicated to my family. I am extremely grateful for their constant love, support, and encouragement. I would not be where I am today without their efforts and countless sacrifices. I thank my sister and brother-in-law for all their help throughout my time in the US. I owe my family more than I am able to express.

Table of Contents

List of Figures

Figure 2.3: Path connectivity in the 432-orientation space. The dashed black line represents a continuous path completely contained within the space. The dashed blue lines represent paths with a jump (shown using green and red dashed lines).

Figure 2.4: Grain boundary misorientation space of point group $C_1(1)$. (a) Represents the symmetry $\vec{q} \sim -\vec{q}$ in the rotation space introduced by the grain exchange symmetry ($M \sim M^{-1}$). (b) The fundamental zone of $C_1(1)$ grain boundary misorientation space. (c) Represents the symmetry $(q_1, q_2, 0) \sim (-q_1, -q_2, 0)$ on the plane $q_3 = 0$ of the fundamental zone. This symmetry is equivalent to a two-fold rotational symmetry in the plane $q_3 = 0$.

Figure 2.5: The character of the surfaces of $C_1(1)$ grain boundary misorientation space: (a) the dashed blue lines represent closed paths and the discontinuity in the path $PQ_1Q_1'P$ can be removed by continuously moving point Q_1 towards the origin. (b) The hemispherical surface $(q_1^2 + q_2^2 + q_3^2 = 1)$ of the misorientation space acts as a *boundary*. Any path that intersects this surface gets reflected back into the fundamental zone at the same point.

Figure 2.6: Grain boundary misorientation spaces with surface symmetries of point groups (a) $C_2(2)$, (b) $C_3(3)$, (c) $C_4(4)$, (d) $C_6(6)$ and (e) $D_3(32)$. (i),(ii) & (iii) show the fundamental zones from different views to illustrate the symmetries on their surfaces. The surfaces with rotational and mirror-line symmetries are colored red and blue respectively and the boundary surfaces are colored grey.

Figure 2.7: (a),(b),(c) and (d) represent misorientation fundamental zones of systems $C_6(6)$, $C_4(4)$, $C_3(3)$ and $C_2(2)$, respectively, stretched along the q_3 axis. A continuous deformation in the angular direction illustrates the topological equivalence between these spaces.

Figure 2.8: A continuous deformation sequence illustrating topological equivalence between $C_2(2)$ and $C_1(1)$ grain boundary misorientation spaces.

Figure 2.9: A continuous deformation sequence illustrating topological equivalence between $D_3(32)$ and $C_2(2)$ grain boundary misorientation spaces.

Figure 2.10: Fundamental zones in orthographic projection of quaternion space for (a) $D_2(222)$ (b) $D_4(422)$ (c) $D_6(622)$ systems. These systems have three surfaces with mirror-line symmetries on them. The surfaces with mirror symmetries are colored (yellow, pink and magenta) and the surfaces with no symmetries are colored grey. Fundamental zones for (d) $T(23)$ and (e) $O(432)$ systems with the surface containing mirror symmetry colored blue.

Figure 2.11: The (a) $D_2(222)$ and (b) $O(432)$ grain boundary misorientation spaces are simply connected. The dashed blue lines represent closed paths and the discontinuity in the path $PQ_1Q_1'P$ can be removed by continuously moving point Q_1 onto the line (a) AG in $D_2(222)$ fundamental zone and the line (b) AC in $O(432)$ fundamental zone.

11

Figure 4.5: The equivalence relations corresponding to Equations (4.4) and (4.6) for even-fold rotational symmetry systems (a) Grain boundary information using (θ, ϕ) parameters. The path ABC_1 in the upper hemisphere is equivalent to the path C_2DE in the lower hemisphere. This equivalence is better represented in its (ii) projection. (b) Grain Boundary information using (θ', ϕ') parameters. In this parameterization the paths ABC_1 and C_2DE and are related by an inversion about the origin. The space is defined as the real projective plane ($\mathbb{R}P^2$).

Figure 4.6: Single-axis grain boundary space for point group C_1. (a) Grain boundary misorientation fundamental zone for C_1 point group in orthogonal projection and with misorientations along the z-axis highlighted. (b) There is a boundary inclination space (2-sphere) associated with every boundary misorientation. This is represented by attaching the north-pole of a sphere (of radius $C(q) = \sqrt{1 - q_0^2}$) to each boundary misorientation. Shown here is a 2-sphere of radius $\frac{1}{\sqrt{2}}$ attached to the misorientation corresponding to $(\omega, \vec{a}) = \left(\frac{\pi}{2}, [0\ 0\ 1]\right)$, .i.e. $\vec{q} = \left(0, 0, \frac{1}{\sqrt{2}}\right)$. (c) A solid parametric ball obtained by considering all the boundary inclinations with z-axis as the misorientation axis. (d) A schematic illustration of the mirror symmetry on the surface of the parametric ball; any vector $[r_1 \quad r_2 \quad r_3] \sim [r_1 \quad r_2 \quad -r_3]$.

Figure 4.7: The equivalence relations on the boundary space can used to determine the symmetries associated with the boundary inclination space (2-sphere). (a) Corresponding to any misorientation with angle $\omega \in [0, \pi)$, the boundary inclination space has no symmetries (C_1). (b) Corresponding to misorientation angle $\omega = \pi$, the boundary inclination space has the symmetry C_s.

Figure C.1: Symmetries associated with the boundary inclination space for crystals with point group symmetry C_2, (a) corresponding to any misorientation with angle $\omega \in [0, \pi/2)$ and misorientation axis $\vec{a} = [0\ 0\ 1]$, the boundary inclination space has a two-fold rotational symmetry (C_2). (b) Corresponding to misorientation angle $\omega = \pi/2$, the boundary inclination space has the symmetry $\overline{4}$.

Figure C.2: Symmetries associated with the boundary inclination space for misorientations along the z-axis for crystals with point group C_n: (a) $C_3 (n = 3)$, (b) $C_4 (n = 4)$, and (c) $C_6 (n = 6)$. (i) Corresponding to any misorientation with angle $\omega \in [0, \pi/n)$, the boundary inclination space has no symmetries (C_n). (ii) Corresponding to misorientation angle $\omega = \pi/n$, the boundary inclination space has the symmetry $\overline{2n}$.

Figure C.3: Symmetries associated with the boundary inclination space for crystals with point group symmetry D_2, (a) corresponding to any misorientation with angle $\omega \in [0, \pi/2)$ and misorientation axis $\vec{a} = [0\ 0\ 1]$, the boundary inclination space has the symmetry C_{2v}. (b) Corresponding to misorientation angle $\omega = \pi/2$, the boundary inclination space has the symmetry D_{2d}.

Figure C.4: Symmetries associated with the boundary inclination space for misorientations along the z-axis for crystals with point group D_n: (a) D_3 $(n = 3)$, (b) $D_4 (n = 4)$, and (c) $D_6 (n = 6)$. (i) Corresponding to any misorientation with angle $\omega \in [0, \pi/n)$, the boundary inclination space has no symmetries (C_{nv}). (ii) Corresponding to misorientation angle $\omega = \pi/n$, the boundary inclination space has the symmetry D_{3h} $(n = 3)$, D_{4d} $(n = 4)$ and D_{6d} $(n = 6)$.

List of Tables

1. Introduction

Over the past few decades, materials scientists have come to an increasing realization that the distribution and connectivity of different grain boundary types play a very important role in governing various mechanical and functional properties of materials. While the role of the structure of grain boundaries in various transport and failure mechanisms in polycrystalline materials has been investigated for more than half a century [1-4], there has been a renewed interest in this field over the past few decades following the suggestion of Watanabe [5] that grain boundary types can be 'designed and controlled'. Revolutionary improvements in the properties of some FCC metals have been gained by increasing the proportion of twin-related, highly symmetric grain boundaries. Various processing routes, such as thermo-mechanical "grain boundary engineering" processing [6-12] and application of magnetic fields [13, 14], have been used to increase the frequency of coincidence site lattice (CSL) boundaries [15], and can dramatically improve resistance to intergranular and transgranular degradation in polycrystalline materials. Some examples include a 50-fold increase in weldability [16], a 16-fold decrease in creep rate [17], a four-fold increase in service life of battery electrodes [18], and a seven-fold increase in critical current density in high-T_c superconductor $YBa_2Cu_3O_7$ [19]. The engineering of grain boundary types has also been combined with the control of microstructural length scales, as in the case of so-called "nano-twinned" materials, which comprise an extreme density of twin-related boundaries with characteristic spacing on the nanometer scale [20-23].

Recently, there has been considerable evidence [24-26] indicating that not just the population of individual interfaces, but also the global connectivity among them, is important in governing properties. This is especially true in cases where grain boundaries act as transport pathways or as barriers to transport, as for conductivity [27-29], diffusivity [30, 31], corrosion resistance [32], creep [33], and embrittlement [34]. The propagation of interfacial failure depends strongly upon the extent of connectivity among the susceptible interfaces, whereas transport across a polycrystal requires a network of transport paths across "low-barrier" boundaries, avoiding "high-barrier" boundaries that tend to block it. In either case, the statistical and spatial distributions of the boundary types are central to the structure-property relationship, and it has

been shown that grain boundary engineered materials with remarkable property enhancements described above in fact exhibit dramatically altered connectivity among different boundary types [35, 36].

Along with the increasing recognition that grain boundary types and their networks are key to structure-property connections, the materials community has developed an impressive suite of experimental tools to study them. From the earliest studies using manual mapping in the transmission electron microscope [37], to automated two-dimensional spatial orientation mapping by electron backscatter diffraction (EBSD) [38], to the present toolkit that includes three-dimensional x-ray diffraction [39, 40] and automated serial sectioning methods [41-43], the field has progressed to the point where the materials scientist now has a quantitative view of the boundary network in full crystallographic detail [44, 45]. The three-dimensional characterization of grain boundaries has enabled numerous studies investigating the role of grain boundary plane distributions in grain boundary engineering [46, 47]. Recent activity elucidating the full five-parameter space of grain boundaries in various common materials [48-53] also speaks to the growing appreciation that the distribution of boundary types must be a focus for the future of microstructural science in general and for microstructure design in particular.

However, the experimental capabilities of the field have outpaced our ability to interpret and represent boundary information. One of the great difficulties in the effort to understand and control grain boundary types is that the space of boundaries is vast and somewhat complicated [54]. The structure of a grain boundary is determined by five crystallographic parameters that represent both the misorientation between the two neighboring grains (3 parameters) and the boundary inclination (2 parameters). Understanding the topology of the complete grain boundary space is crucial not only for defining the notion of distributions of grain boundaries but also for formulating continuous analytical functions relating the structure of grain boundaries to properties such as energy and mobility [52, 55]. From a topological point of view, the five-parameter space is complex: it contains a singularity at the zero-misorientation point, where there is no longer any boundary [54], and involves various symmetries from the crystals and the required invariance to an exchange of the two grains at the boundary [56]. As a result of these complexities, the topology of the complete grain boundary space is currently unclear. However, the problem is even more dire than this: even a well-studied part of the five-parameter space—

the three parameters of the grain boundary misorientation— remains relatively poorly understood because of various shortcomings of existing parameterizations and visualization methods [57-59].

To be able to analyze and exploit the full potential of the vast amounts of experimental data available to materials scientists, it is crucial to develop tools that help resolve or remove some of the complexities of the grain boundary space. Since the difficulties associated with the representation and analysis of the grain boundary parameters are largely mathematical, it is beneficial to first establish the conventions necessary to properly define misorientations and the boundary parameters. We also explore some relevant topological notions that will be useful in the analysis of these abstract mathematical parameters.

1.1. Definitions and Conventions

Experimentally, the determination of grain boundary parameters begins with measuring the orientation difference between adjoining grains. The symmetries of grain boundary parameters are closely related to the symmetries of individual crystals that make the grain boundary. The analysis of grain boundary parameters, therefore, begins with an examination the orientation space, which in turn requires the definition of the rotation space.

1.1.1. Rotation Space

An ordinary rotation operation (also known as a proper rotation) is defined as a rigid-body transformation around a fixed axis called the *axis of rotation*. Since infinitesimal rotation operations are well-defined (i.e. rotations of infinitesimally small rotation angles), the set of all rotations has a continuous structure and is defined as the rotation space. It is necessary to clearly specify the frame of reference and the convention, active or passive [60], to be able to relate the rotation to the orientation of a particular grain or to the misorientation between two objects. While we use the active convention to describe rotations in this work, the conventions for the reference coordinate frame will be discussed in detail in the definitions of orientation and misorientation spaces.

To work with the abstract notion of a rotation, a variety of parameterizations have been conceived, which can be broadly classified as:

(a) Rotation matrices: 3×3 matrices with special properties, such as orthogonality and positive unit determinant, represent proper rotations. The group of matrices with these properties belong to the Special Orthogonal Group [61] denoted as $SO(3)$. There is a one-to-one correspondence between the rotation space and the group $SO(3)$, therefore, the entire space of rotations is often represented by $SO(3)$. In the case of two-dimensional rotations, 2×2 special orthogonal matrices belonging to the group $SO(2)$ are used to specify rotations.

(b) Euler angles [62, 63]: The Euler angle triplet (ϕ_1, Φ, ϕ_2), which describes any rotation as a sequence of three successive rotations, has been routinely used by crystallographers because of their use in diffraction (three-circle goniometry [64]) and in pole figure inversion methods [63, 65-67].

(c) Axis-angle parameters [58, 68]: The axis-angle parameters denote the axis $\vec{a}$ and angle ω of rotation and hence are naturally intuitive. Two-dimensional rotations correspond to rotations around a fixed axis and we consider the axis of rotation to be the z-axis and the crystals being rotated to reside in the x-y plane (without loss of generality). Hence, in the special case of two-dimensional rotations it suffices to specify just the rotation angle ω. The primary drawback of the axis-angle parameters, in the description of three-dimensional rotations, is the degeneracy that exists as the rotation angle approaches zero, since the axis of rotation is not defined when $\omega = 0$. However, this degeneracy disappears when the axis-angle parameters are mapped to unit-quaternions.

(d) Quaternions [58, 69-71]: A unit quaternion **q** is a four-dimensional vector of the following form:

$$\mathbf{q} = (q_0, \bar{q}) = (q_0, q_1, q_2, q_3), \qquad \text{satisfying} \sum_{i=0}^{3} q_i^2 = 1 \qquad (1.1)$$

It is related to the axis-angle parameters through the relation:

$$\mathbf{q} = \left(\cos\left(\frac{\omega}{2}\right), a_x \sin\left(\frac{\omega}{2}\right), a_y \sin\left(\frac{\omega}{2}\right), a_z \sin\left(\frac{\omega}{2}\right) \right) \qquad (1.2)$$

where $\vec{a} = (a_x, a_y, a_z)$ represents the axis and ω denotes the angle of rotation.

The correspondence between rotations and four-dimensional unit vectors suggests the possibility of a representation of the rotation space using unit four-dimensional sphere (called the 3-sphere). Indeed, the rotation space is equivalent to the 3-sphere S^3 with antipodal points *identified*[1]. The topological consequences of this equivalence are explained in section 2.3.1. In the case of two-dimensional rotation space, any rotation operation can be specified by the angle of rotation $\omega \in [0, 2\pi]$, which can be represented by points on a circle with coordinates $(\cos \omega, \sin \omega)$. Hence, the 2D rotation space is equivalent to a circle (S^1) and the topological aspects of the 2D rotation space are deduced from the topology of the circle (refer to section 2.2.1).

In this entire thesis, we will use the quaternion parameterization extensively. This is not only due to the convenient mathematical properties of the unit-quaternions [56, 59, 72-75] but also because the topological properties of the rotation space are better appreciated when represented as a 3-sphere using the quaternion parameterization. But the matrix representation is also useful, especially in expressing rotations of vectors, which can be conveniently represented using matrix multiplication of a vector. Hence, we define a matrix representation **g**, which is a function that converts any parameterization into a matrix representation. For example, the matrix representations of rotations represented by M, and by a quaternion **q**, and an axis-angle pair $(\omega, \vec{a})$ are given by $\mathbf{g}(M)$, $\mathbf{g}(\mathbf{q})$ and $\mathbf{g}(\omega, \vec{a})$ respectively.

1.1.2. Orientation Space

An orientation (denoted as O) is simply an active rotation operation that relates a fixed right-handed reference coordinate axes, usually aligned along the sample edges, and a right-handed crystal coordinate axes embedded in the grain whose orientation is of interest. Hence, the orientation space is equivalent to the rotation space, but is modified by a number of *equivalence relations*[2] [76] that arise due to symmetries of the underlying crystals. For example, a right-handed orthogonal coordinate system can be embedded in two different ways in a crystal with two-fold rotational symmetry ($C_2(2)$ point group symmetry), as illustrated schematically in

---

[1] Antipodal points refer to diametrically opposite points on the surface of the sphere. In this case, the points $\mathbf{q} = (q_0, q_1, q_2, q_3)$ and $-\mathbf{q} = (-q_0, -q_1, -q_2, -q_3)$ are the antipodal points on the 3-sphere. By identification of antipodal points, we mean gluing together the diametrically opposite points on the 3-sphere.

[2] An equivalence relation is a relation defined on a set with the properties of reflexivity, symmetry and transitivity. It is indicated by "~".

Figure 1.1. This results in two distinct rotations that describe the same orientation (and hence are defined to be symmetrically equivalent).
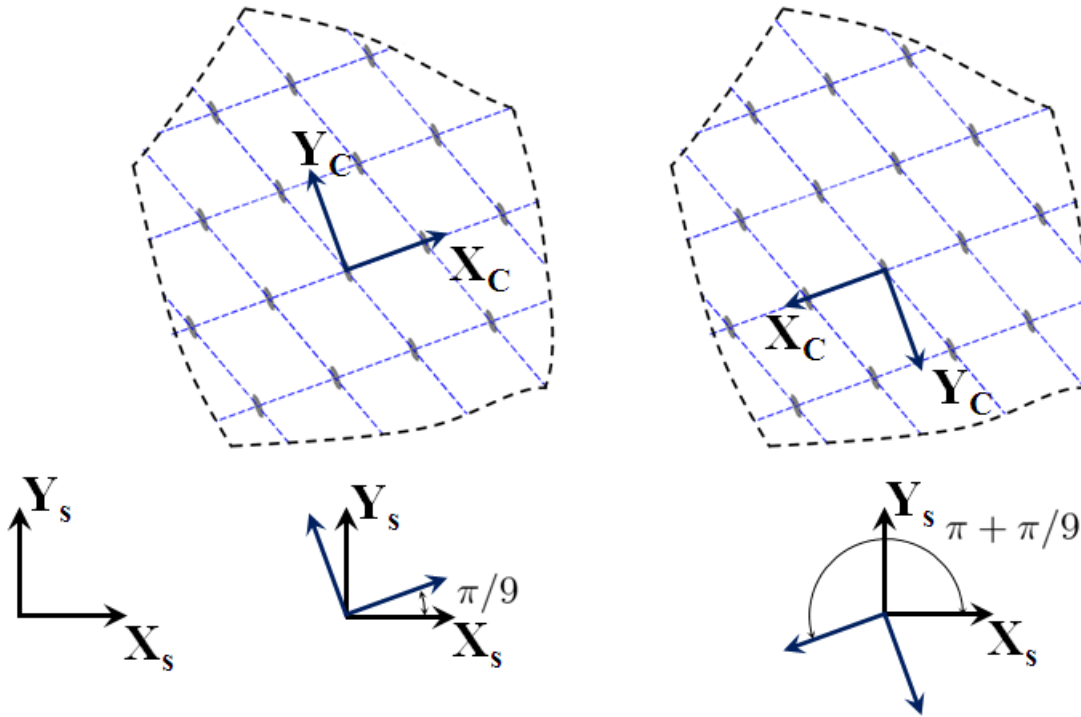
Figure 1.1 Schematic illustrating equivalent descriptions of the orientation of a grain with two-fold rotational symmetry. Because of the underlying crystal symmetry, there are two distinct ways of embedding the crystal coordinate axes (denoted by subscript C). Hence, there are two distinct rotations $\pi/9$ and $10\pi/9$, measured with respect to the reference coordinate axes (denoted by subscript S), that describe the orientation of this grain.

In the general case, the rotational symmetry operations that belong to the crystallographic point group of the crystal, indicated by S_i, give rise to symmetrically equivalent descriptions:

$$O \sim OS_i, \qquad where\ i = 1, \dots, n. \tag{1.3}$$

where n is the *order* of the corresponding rotational point group (i.e., the number of non-equivalent rotational symmetry operations in a point group). The orientation space is defined as the rotation space with all the symmetrically equivalent orientations identified. From a topological perspective, the orientation spaces are *quotient spaces*[3] [76] of the rotation space, and it is important to note that the topology of a quotient space is not inherited in an obvious way

---

[3]A quotient space is a space derived from another space X (referred to as the parent space) by identifying all the equivalent points defined by the set of equivalence relations E. The quotient space is denoted as X/E.

from the parent space; the quotient topology depends on the equivalence relations that result in the quotient space. The symmetry operations that appear in the equivalence relations of Equation (1.3) depend on the rotational point group G of the underlying crystal. The topological properties of the orientation spaces are discussed in section 2.3.2.

1.1.3. Misorientation Space

A misorientation between two grains A and B is defined as an active rotation operation that brings a crystal aligned with the coordinate axes of one grain (suppose grain A) into coincidence with the crystal coordinate axes of the other grain (suppose grain B). Suppose the orientation of grain A is O_A and that of grain B is O_B, then the misorientation measured with respect to the crystal coordinate axes of grain A (the reference frame) is denoted as M_{AB} and is given by $M_{AB} = O_A^{-1}O_B$. It is now evident that distinct (yet symmetrically equivalent) orientation descriptions of grains A and B result in distinct rotations that describe the same misorientation. These distinct descriptions of the same misorientation are deemed equivalent and the equivalence relations for the misorientations are expressed as:

$$M_{AB} = O_A^{-1}O_B \text{ and } M_{AB}^{ij} = \left(O_A S_A^i\right)^{-1}\left(O_B S_B^j\right) = \left(S_A^i\right)^{-1}\left(O_A^{-1}O_B\right)\left(S_B^j\right) \Rightarrow$$

$$M_{AB} \sim \left(S_A^i\right)^{-1}M_{AB}\left(S_B^j\right) \qquad where \ i = 1, \dots, n \ and \ j = 1, \dots, m$$

(1.4)

where S_A, S_B refer to the rotational symmetry operations and n, m refer to the order of the rotational point groups of crystals A and B respectively. Similarly, the misorientation with respect to grain B is denoted as M_{BA} and can be expressed in terms of M_{AB} as $M_{BA} = M_{AB}^{-1}$. If grains A and B belong to distinct phases, a convention is adopted, for example, the phase with lower symmetry is assigned to be grain A and the misorientation is always measured with respect to the crystal coordinate axes embedded in grain A. But if grains A and B belong to the same phase, they are physically indistinguishable from each other, and it is not possible to explicitly select a reference grain. Misorientations associated with such boundaries, referred to as *grain boundary misorientations*, will be the focus of this work and hence will be elaborated in section 1.1.5.

Analogous to the definition of the orientation space, the misorientation space is defined as the rotation space with all the symmetrically equivalent misorientations identified. The symmetry operations that appear in the equivalence relations in Equation (1.4) depend on the crystallographic point groups of grains A and B and hence misorientation spaces are classified according to the crystallographic point groups of the adjoining grains.

1.1.4. Boundary Space

In addition to misorientations, the structure of a boundary is determined by the boundary plane normal and other microscopic degrees of freedom. It has been usually argued that it suffices to consider only the macroscopic degrees of freedom, the boundary misorientation and the inclination, to establish structure-property correlations [46]. As previously discussed, three independent variables are required to uniquely specify a misorientation and the normal vector (denoted as $\vec{n}$) can be represented using two variables. A boundary thus has five macroscopic degrees of freedom, which are referred to as the boundary parameters, and is denoted by $\boldsymbol{B} = (M, \vec{n})$.

The usual method of determining grain boundary parameters, e.g. for a boundary as shown in Figure 1.2, first involves the selection of a grain as a reference and then the misorientation and the boundary inclination are measured with respect to the crystal coordinate axes of the reference grain. Suppose that grain A is selected as the reference; the boundary misorientation is well-defined. But the direction of the boundary normal vector is not determined a priori, i.e. the vector can be directed towards or away from grain A. A convention is necessary (especially important for crystals without an inversion center) and the direction of the boundary normal is fixed to be directed away from the reference grain (i.e. grain A) [77]. The boundary between two grains A and B, measured with reference to grain A, is indicated as $\boldsymbol{B_{AB}} = (M_{AB}; \vec{n}_{AB})$. Using this convention, the boundary parameters between grain B and grain A are given by $\boldsymbol{B_{BA}} = (M_{BA}; \vec{n}_{BA})$, where $M_{BA} = (M_{AB})^{-1}$ and $\vec{n}_{BA} = \mathbf{g}(M_{BA}) * (-\vec{n}_{AB})$ is the corresponding normal vector.
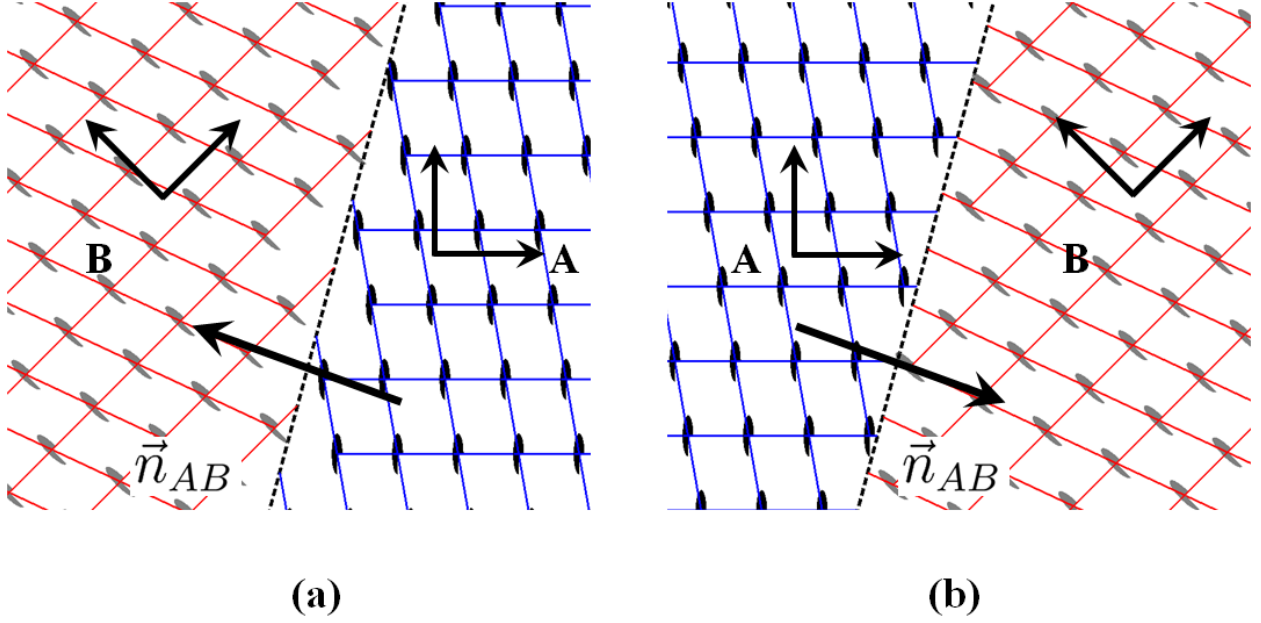
Figure 1.2 Boundary (a) is physically different from boundary (b) and this difference can be reflected in the measured parameters only if a fixed convention is followed in assigning the boundary plane normal. The convention here is that if the boundary parameters are measured with respect to grain A, then the boundary normal is always directed away from the reference grain A. Using this convention, the two boundaries in (a) and (b) are defined by distinct parameters $(M; \vec{n})$ and $(M; -\vec{n})$ respectively.

As was the case with misorientation space, owing to various symmetries of the boundary and the underlying crystals, there are distinct parameters that describe the same physical boundary and hence are symmetrically equivalent. Due to rotational point group symmetries of the underlying crystals, a grain boundary with parameters $\boldsymbol{\mathcal{B}_{AB}} = (M_{AB}; \vec{n}_{AB})$ has distinct representations that are considered to be symmetrically equivalent and are expressed as:

$$\boldsymbol{\mathcal{B}_{AB}} = (M_{AB}; \vec{n}_{AB}) \sim \boldsymbol{\mathcal{B}_{AB}^{ij}} = \left(\left(S_A^i\right)^{-1} M_{AB} \left(S_B^j\right); \ \mathbf{g}\left(\left(S_A^i\right)^{-1} \right) * \vec{n}_{AB} \right)$$

(1.5)

where $i = 1, \dots, n$ and $j = 1, \dots, m$

The conventions for the case where grains A and B belong to the same phase will be specified in the next section under the discussion of grain boundaries.

The boundary space refers to the collection of these geometric parameters that determine the structure of a grain boundary along with the equivalence relations. The boundary inclination space is the unit-sphere in three dimensions (2-sphere, S^2) since any normal vector can be represented as a point on the unit-sphere. The space of misorientations is the quotient space of

the rotation space $\left(SO(3)\right)$. Since the complete boundary inclination space (S^2) is accessible for any boundary misorientation, the boundary space is the quotient space of the *product space* of misorientations $\left(SO(3)\right)$ and boundary inclinations (S^2), i.e. $\mathcal{B} = SO(3) \times S^2/E$, where E denotes the set of equivalence relations that arise due to various symmetries.

1.1.5. Grain Boundary Space

Grain boundaries are referred to as the interfaces between grains of the same phase, i.e. the grains are physically indistinguishable from one another. All other interfaces are referred to as interphase boundaries [78]. In the case of crystals that do not contain the inversion center symmetry, the convention by Morawiec is followed and the enantiomorphic forms of this crystal are treated as distinct phases and hence an interface between them is an interphase boundary [79]. According to this definition, any grain boundary misorientation can be specified by a proper rotation.

The specification of grain boundary parameters requires an explicit selection of a reference grain. Since grains A and B that adjoin a grain boundary belong to the same phase and are physically indistinguishable, there is an uncertainty associated with the selection of the reference coordinate axes. This uncertainty results in what is called as the "grain exchange symmetry"[4] [56, 78] which results in the identification of the grain boundary parameters $\mathcal{B}_{AB}$ and $\mathcal{B}_{BA}$ measured with respect to both the adjoining grains, i.e.

$$\mathcal{B}_{AB} = \mathcal{B} = (M; \vec{n}) \sim \mathcal{B}_{BA} = \mathcal{B}^{-1} = \left(M^{-1}; \mathbf{g}(M^{-1}) * (-\vec{n})\right) \qquad (1.6)$$

The set of equivalence relations obtained by combining Equation (1.5) and the grain exchange symmetry can be described as:

$$(M; \vec{n}) \sim \left(\left(S^i\right)^{-1} M(S^j); \ \mathbf{g}\left(\left(S^i\right)^{-1}\right) * \vec{n}\right) \sim \left(M^{-1}; \mathbf{g}(M^{-1}) * (-\vec{n})\right)$$
$$\sim \left(\left(S^j\right)^{-1} M^{-1}(S^i); \ \mathbf{g}\left(\left(S^j\right)^{-1} M^{-1}\right) * (-\vec{n})\right) \qquad (1.7)$$

---

[4] The grain exchange symmetry is analogous to the rotational symmetries present in a crystal. The rotational symmetries result in an uncertainty in fixing unique right-handed coordinate-axes to the crystal. For example, there are 24 distinct ways of embedding a right-handed coordinate system in a crystal with cubic point group symmetry which result in 24 symmetrically equivalent descriptions for grain orientations.

If only the grain boundary misorientations are of interest, the set of equivalence relations on the grain boundary misorientation space can be expressed as:

$$M \sim \left(S^i\right)^{-1} M\left(S^j\right) \sim M^{-1} \sim \left(S^j\right)^{-1} M^{-1}\left(S^i\right) \qquad (1.8)$$

There is an additional condition in the case of the grain boundary space, i.e. when the boundary inclination is considered, which manifests itself as a singularity, known as the 'no-boundary' singularity. The 'no-boundary' singularity refers to the zero misorientation boundaries. For interphase boundaries, at $M = I$ (where I represents the zero misorientation) there still exists a physical boundary that separates the two phases, and thus different boundary inclinations are physically distinguishable. However, in the case of grain boundaries, zero misorientation implies that there is no boundary at all; there are no additional inclination degrees of freedom for $M = I$. This condition is expressed as:

$$\mathcal{B}_I = (I; \vec{n}) \sim \mathcal{B}'_I = \left(I; \overrightarrow{n'}\right) \qquad \forall \, \vec{n}, \overrightarrow{n'} \in S^2 \qquad (1.9)$$

Therefore, the grain boundary space is defined as the collection of grain boundary parameters with the set of equivalence relations consisting of those described in Equation (1.5), the grain exchange symmetry and the 'no-boundary' singularity. It is noted that the equivalence relations that arise due to the grain exchange symmetry (Equation (1.6)) and the 'no-boundary' singularity (Equation (1.9)) significantly complicate the topology of the grain boundary space and severely undermine our ability to perform mathematical analysis on this space.

1.1.6. Classification of Misorientation and Boundary Spaces

The orientation and grain boundary misorientation spaces are quotient spaces of the rotation space $SO(3)$ and the complete grain boundary space is the quotient space of the product space $SO(3) \times S^2$. The topology of the quotient space depends upon the type of equivalence relations imposed on the parent space. In the case of orientation and misorientation spaces, it is observed that only the rotational symmetry elements (in addition to the grain exchange symmetry for grain boundary misorientations) of a crystallographic point group appear in the equivalence relations (Equations (1.3) and (1.4)). Hence the topology of these spaces is determined entirely by the rotational point group of a corresponding crystallographic point group. For example, the

grain boundary misorientation spaces of crystallographic point groups 432, $\bar{4}3m$ and $m\bar{3}m$ are identical and are completely determined by the rotational symmetry operations that belong to point group 432. Since, there are 11 rotational point group symmetries (corresponding to the 11 Laue Groups) that are allowed in three-dimensional crystal systems (tabulated in Table 1.1), the orientation and grain boundary misorientation spaces are classified into 11 categories.

However, the topology of complete grain boundary spaces not only depends on the rotational point group symmetries of the underlying crystals but also on the mirror and inversion symmetries. It suffices to consider the equivalence relations shown in Equations (1.7) and (1.9) for point groups with only proper rotational symmetry elements. The topological aspects of the boundary spaces of the remaining crystallographic point groups are obtained by considering the following equivalence relation in addition to the relations in Equations (1.7) and (1.9):
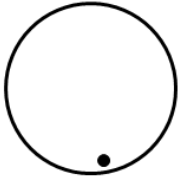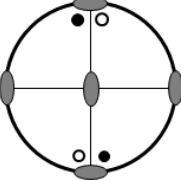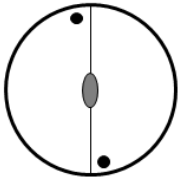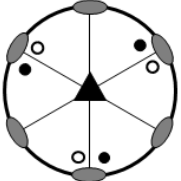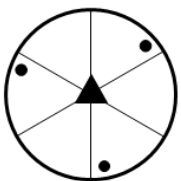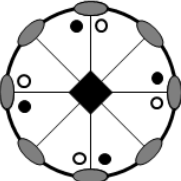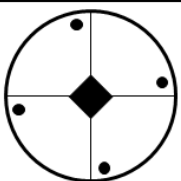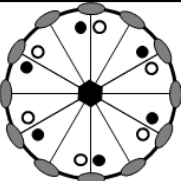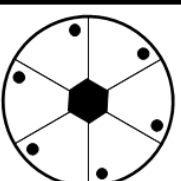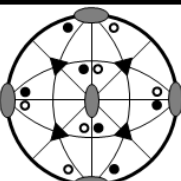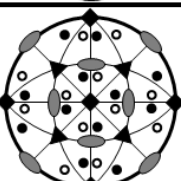
$$(M_{AB}; \vec{n}_{AB}) \sim \left((A_\omega^{-1})M_{AB}(A_\omega); \mathbf{g}(A_\omega^{-1}) * (-\vec{n}_{AB})\right) \tag{1.10}$$

where A_ω, when expressed in axis-angle parameters, is $(2\pi, [0 \quad 0 \quad 1])$ for the 11 Laue groups, $A_\omega = (\pi, [0 \quad 0 \quad 1])$ for point groups with a horizontal mirror plane (crystallographic point groups $C_s(\bar{2})$ and $C_{3h}(\bar{6})$). If the crystallographic point group consists of a vertical mirror plane then $A_\omega = (\pi, [0 \quad 1 \quad 0])$ ($C_{2v}(m\,m\,2)$, $C_{3v}(3\,m)$, $C_{4v}(4\,m\,m)$, $C_{6v}(6\,m\,m)$, $D_{3h}(\bar{6}\,m\,2)$) and $A_\omega = (\pi, [1 \quad 1 \quad 0])$ if the point group consists of the diagonal mirror plane ($D_{2d}(\bar{4}\,2\,m)$ and $T_d(\bar{4}\,3\,m)$). Finally, $A_\omega = (\pi/2, [0 \quad 0 \quad 1])$ for the crystallographic point group $S_4(\bar{4})$. Note that in systems where the crystallographic point groups of the crystals belong to one of the Laue groups, Equation (1.10) simplifies to the relation:

$$(M_{AB}; \vec{n}_{AB}) \sim (M_{AB}; -\vec{n}_{AB}) \tag{1.11}$$

In this thesis, we investigate the topology of grain boundary spaces of crystals with only proper rotational symmetries and hence the grain boundary misorientation spaces and complete grain boundary spaces are classified into the 11 point groups tabulated below.

Table 1-1 The eleven crystallographic point groups with only proper rotational symmetry elements, which are used to classify orientation and grain boundary misorientation spaces.

Schönflies (International)	Symmetry Axes	Order	Schönflies (International)	Symmetry Axes	Order
C_1 (1)		1	D_2 (222)		4
C_2 (2)		2	D_3 (32)		6
C_3 (3)		3	D_4 (422)		8
C_4 (4)		4	D_6 (622)		12
C_6 (6)		6	T (23)		12
			O (432)		24

1.2. Problem Statement

Given the high-dimensionality of the grain boundary space, there is an immediate need for theoretical tools to better visualize and analyze the vast amount of experimental data available to materials scientists. For example, even though misorientations can be represented using three independent variables, many conceptual difficulties regarding the misorientation space arise due to the higher dimensionality of the rotation space [57]. Due to these complexities, much of the misorientation information is discarded during simple graphical representations, which is the first step in the analysis of grain boundary networks.

Figure 1.3 shows some examples of these common methods of representing grain boundary types, using EBSD maps of specimens of polycrystalline copper-chromium alloy (Lattice: Face Centered Cubic, Point Group: $m3m$) and Rhenium (Lattice: Hexagonal, Point Group: $6/mmm$). Figure 1.3(a) shows the microstructure with grain boundaries highlighted in black. Figure 1.3(b) and Figure 1.3(c) show the same dataset, with grain boundaries differentiated by categories based on misorientation: Figure 1.3(b) classifies boundaries according to the misorientation angle differentiated by shading, and Figure 1.3(c) adds colors corresponding to some 'special' misorientations corresponding to coincidence site lattice numbers ($\Sigma 3$, $\Sigma 9$, and $\Sigma 27$ for Cu-Cr and $\Sigma 13$ and $\Sigma 17$ for Rhenium).

Both of these types of maps are common in the literature, and abandon most of the available misorientation information captured in the original EBSD dataset. In discarding most of the misorientation information, such maps are of little lasting value to the community, which can never recover the original data. Additionally, the physical significance of the binning procedure is almost certainly deficient, and the binning procedure can in fact suppress important intuitive features of the data. For example, the coloring schemes in Figure 1.3 lack an intuitive notion of "distance" in the misorientation space in these representations; it is not possible to appreciate how similar or dissimilar boundaries are in terms of both the axis and angle of the misorientation.
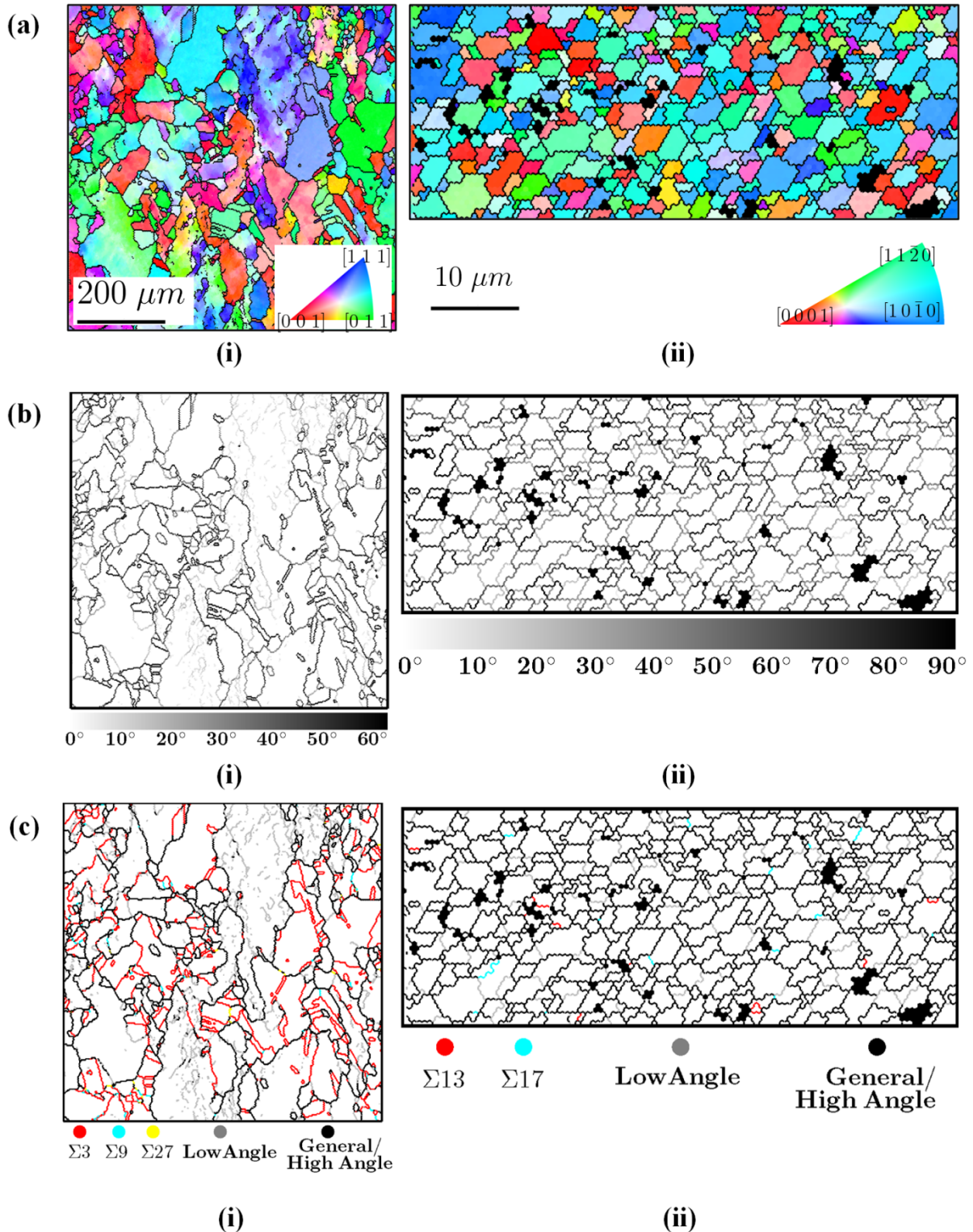
Figure 1.3 Deficiencies in existing grain boundary maps are illustrated using samples of (i) Cu-Cr and (ii) Rhenium alloys. (a) EBSD micrographs with grain boundaries highlighted. (b) Grain boundaries colored according misorientation angle alone (low- vs. high-angle). (c) Grain boundary map showing the specific coincidence misorientations (colored), as well as low angle (grey) and high angle (black) boundaries. These maps do not represent complete misorientation information and the coloring does not capture misorientation distances between the various boundaries.

31

The reason grain boundary networks are viewed with such rudimentary classification schemes is largely mathematical: the full spectrum of misorientations is not presented in such maps because there is no known method of doing so. The difficulty of establishing a mapping between misorientations and colors arises because of the apparent mismatch in topology between these two spaces. Color spaces, like the ones illustrated in Figure 1.4, are *simply connected*[5] [76] spaces in three-dimensional Eculidean space ($\mathbb{R}^3$), and are represented as, e.g., a cube (the well-known red-green-blue or RGB space, Figure 1.4(a)), a solid ball (the so-called hue-saturation-lightness or HSL space, Figure 1.4(b)), or a cone (the hue-saturation value HSV space, Figure 1.4(c)). On the other hand, rotation space is not simply connected and is of higher dimensionality [80].
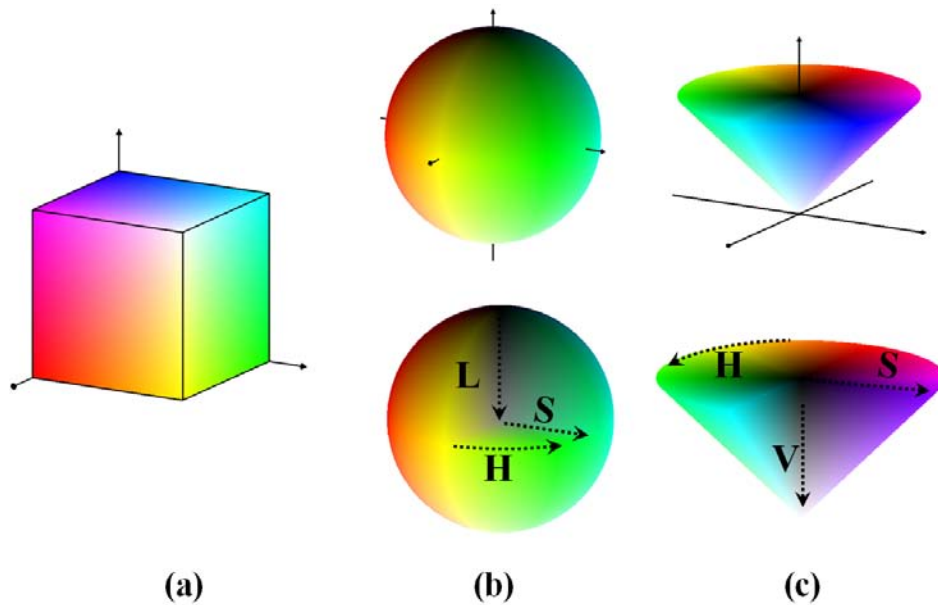
Figure 1.4 Common representations of the color space. (a) RGB Color cube (b) HSL Color sphere (c) HSV color cone. Color spaces are simply connected in $\mathbb{R}^3$.

It is also evident from the definition of the complete boundary space that the conditions imposed on the parameter space by the physical boundary space, i.e. the equivalence relations on the parameter space due to various crystal symmetries, the grain exchange symmetry and the 'no-boundary' singularity, play a major role in the interpretation and analysis of experimentally obtained three-dimensional grain boundary information. The complications that arise during

---

[5] A topological space with the property that any closed path (a path that originates and ends at the same point) in the space can be continuously shrunk to a single point is said to be simply connected

analysis of the complete grain boundary space due to the equivalence relations of Equations (1.6) and (1.9) are better appreciated by comparing the grain and interphase boundary spaces.

The space of interphase boundaries is essentially the product space $SO(3) \times S^2$ and the relevant equivalence relations arise only due to the crystal symmetries (Equation (1.5)). It is not necessary to consider the grain exchange symmetry since the two adjacent phases are physically distinguishable. Even the 'no-boundary' singularity does not exist since at the zero-misorientation there exists a physical boundary that separates the two phases, and thus different boundary inclinations are physically distinguishable. The product space $SO(3) \times S^2$ is well understood, and metrics and measures on this space have been recently developed [77]. Analysis on the space of interphase boundaries is facilitated by the standard basis functions on the rotation space $(SO(3))$ and the 2-sphere (S^2).

However, the grain boundary space is equivalent to the product space of the misorientation space and the unit vector space but with the significant added caveat that all the normal vectors corresponding to the zero-misorientation boundary are collapsed into a single point. In order to define basis functions on the space of grain boundaries, it is necessary to resolve the singularity in the grain boundary space and understand the role of the grain exchange symmetry. The existence of basis functions is extremely beneficial not only because it facilitates harmonic analysis but also because any analytical function (e.g. a continuous grain boundary energy function) can be expanded as a linear combination of the basis functions.

1.3. Layout of this thesis

As described in section 1.2, there are a number of limitations related to analyzing grain boundary information that can be addressed uniquely through a rigorous topological analysis of the grain boundary parameter space.

The thesis can be broadly classified into two parts. The central goal of the first part of the thesis is to address the deficiencies in the visualization of grain boundary misorientation information. In Chapter 2, we present an unexpected mathematical discovery about grain boundary misorientation spaces, which in turn leads to a new method of coloring grain boundary networks such as those shown in Figure 1.3. We develop a method to label each boundary segment with a single color that uniquely (one-to-one) identifies its misorientation, with no part of the

misorientation information neglected, and where similar misorientations have similar colors (continuous). Mathematically, we present an embedding [76] (defined as a continuous and one-to-one mapping) of the grain boundary misorientation spaces for crystals of $D_2(222)$, $D_4(422)$, $D_6(622)$, $T(23)$ and $O(432)$ point symmetries in three-dimensional Euclidean space (since the color space is embedded in $\mathbb{R}^3$). In Chapter 3, we put these mappings to practical use by developing grain boundary misorientation maps, which provide an intuitive (unique and continuous) way to represent grain boundary networks without discarding any of the misorientation information.

In the second part of the thesis, conditions under which the topology of the grain boundary space has been resolved are presented. In chapter 4, we initially focus on the topology of the grain boundary space of two-dimensional crystal systems. The analysis of 2D grain boundary space emphasized the necessity of a new parameterization that naturally accounts for the 'no-boundary' singularity and simplifies the equivalence relation associated with the grain exchange symmetry. Therefore, we develop a new parameterization that simplifies, to some extent, the equivalence relations on the grain boundary space. With the aid of this new parameterization, we resolve the topology of a subspace of the grain boundary space, i.e. the collection of grain boundary parameters with the misorientation axis confined to lie along a particular crystal direction. This development provides a rigorous framework for the description of statistics of grain boundaries with misorientations along a single axis.

2. Topology of Grain Boundary Misorientation Spaces

2.1. Introduction

We are interested in embedding the grain boundary misorientation spaces in three-dimensional Euclidean space ($\mathbb{R}^3$) to obtain a coloring scheme that is both continuous and one-to-one. The minimum number of Euclidean dimensions in which a space can be embedded is a topological property. The purpose of this chapter is to investigate the topology of the grain boundary misorientation spaces with a focus on the effect of symmetry operations on their minimum embedding dimensions in Euclidean space. In addition to the embedding properties, a key property we use to investigate the topology of these quotient spaces is the fundamental group [76]. A topological space with the property that any closed path (one that originates and ends at the same point) in the space can be continuously shrunk to a point has a trivial fundamental group [76] and is said to be simply connected. For example, the color spaces are simply connected spaces in $\mathbb{R}^3$ and hence, for an embedding in the color space, it is necessary for the misorientation space to be simply connected.

Since the misorientation space is obtained by sequentially applying equivalence relations to the rotation and the orientation spaces, we provide a systematic analysis of the rotation, orientation and grain boundary misorientation spaces in this chapter. First, the topological properties of orientation and misorientation spaces of two-dimensional (2D) crystal systems are presented. This case of 2D crystal systems, albeit simple, provides an intuitive interpretation of various topological concepts that are relevant in this chapter. We show that the topologies of the 2D grain boundary misorientation spaces are very different and much simpler than that of the 2D rotation and 2D orientation spaces. Then, we investigate the embedding properties of the three-dimensional rotation and misorientation spaces.

2.2. Two-Dimensional Crystal Systems

2.2.1. Two-Dimensional Rotation Space

Embedding: Even though only one independent variable (ω) is required to uniquely represent 2D rotations, a minimum of two variables (coordinates of a circle) are required for a one-to-one and continuous representation. Any bijective mapping $f: \mathbf{R_{2D}} \rightarrow [0,2\pi)$, where $\mathbf{R_{2D}}$ represents

the 2D rotation space, is not continuous [76]. The discontinuity arises due to the equivalence of the rotations ω and $\omega + 2\pi$. However, there exist bijective mappings $f: \mathbf{R_{2D}} \rightarrow SO(2)$ and $f: \mathbf{R_{2D}} \rightarrow S^1$, which are continuous with a continuous inverse. This implies a topological equivalence of the 2D rotation space, $SO(2)$ and S^1. $f: \mathbf{R_{2D}} \rightarrow S^1$ represents an *embedding* in $\mathbb{R}^2$ because a circle resides in $\mathbb{R}^2$ (the two-dimensional Euclidean plane). S^1 is the quotient space of a line segment with its end points identified. If the domain $\omega = [0, 2\pi]$ is used to represent rotations, the rotations $\{0\}$ and $\{2\pi\}$ are equivalent (connected in a topological sense). The minimum number of Euclidean dimensions required to establish this connectivity is two. Figure 2.1(a) is a graphical representation of the rotation space using colors; each color uniquely determines the rotation (one-to-one) and similar colors represent similar rotations (continuity).

Fundamental Group: The 2D rotation space has a non-trivial fundamental group, which is to say that there exist closed paths that cannot be continuously deformed into a single point. The 2D rotation space is *homeomorphic* to a circle and any closed path on a circle covers the entire circle and cannot be deformed into a single point without moving the path out of the circle. The fundamental group of S^1 and hence the 2D rotation space is $\mathbf{Z}$ (the additive group of integers) [76].

2.2.2. Orientation Spaces of Two-Dimensional Crystal Systems

The 2D orientation space is obtained by applying the equivalence relations in Equation (1.3) to the 2D rotation space. When expressed using the ω parameterization the equivalence relations take the form: $\omega \sim \omega + 2\pi/n$. In this case the unique representatives of ω (fundamental zone) belong to the interval $[0, 2\pi/n)$. The quotient space of rotations obtained after applying this equivalence relation is equivalent to the rotation space with the same connectivity, except that the domain is scaled by n. Thus, from a topological point of view, the orientation space in 2D crystal systems is equivalent to the 2D rotation space. Figure 2.1(b) shows a graphical representation of the orientation space of the C_2 system. It is color coded in a similar fashion to the rotation space in Figure 2.1(a). The coloring represents the connectivity and the topological equivalence. The topological equivalence implies that the minimum embedding dimension for the orientation spaces is two and the fundamental group is $\mathbf{Z}$.
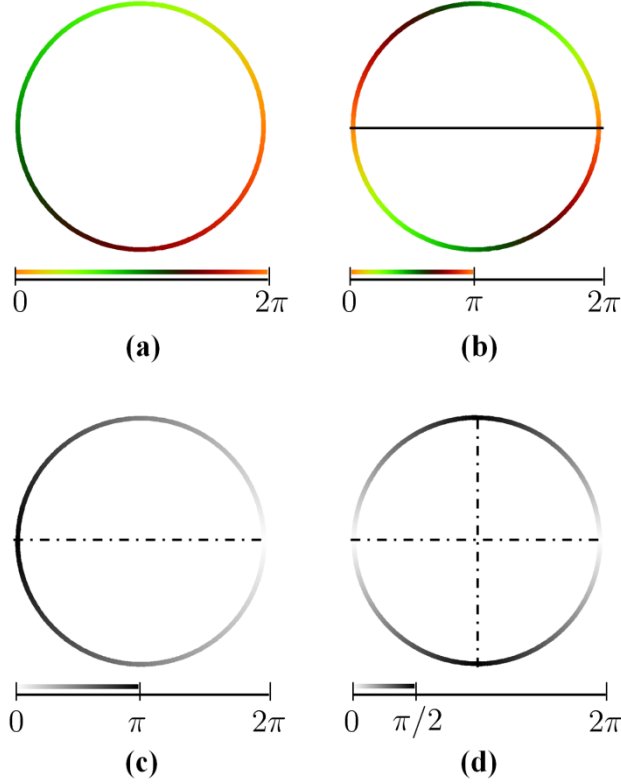
Figure 2.1 The rotation, orientation and misorientation spaces represented on a circle and using ω parameterization, color coded to show the inherent connectivity of these spaces. (a) The 2D rotation space: $\omega \in [0, 2\pi)$ and the coloring indicates that $\omega \sim 2\pi + \omega$. (b) Orientation space of C_2 system: $\omega \in [0, \pi)$ and $\omega \sim \pi + \omega$. (a) & (b) are topologically equivalent. (c) Grain boundary misorientation space of C_1 system: $\omega \in [0, \pi]$ and $\omega \sim 2\pi - \omega$. The crucial difference is that the end points of the domain 0 and π are not identified. (d) Grain boundary misorientation space of C_2 system: $\omega \in [0, \pi/2]$.

2.2.3. Grain Boundary Misorientation Spaces of Two-Dimensional Crystal Systems

In the case of grain boundary misorientations, the grain exchange symmetry (Equation (1.8)) is added to the equivalence relations. We find that this additional equivalence relation reduces the embedding dimensions for the representation of grain boundary misorientations and also results in a trivial fundamental group for grain boundary misorientation space. The equivalence relations for the grain boundary space, when expressed using the ω parameterization, take the following form:

$$\text{(a) } \omega \sim \frac{2\pi i}{n} + \omega; \quad where\ i = 1, \dots, n \tag{2.1}$$

$$\text{(b) } \omega \sim 2\pi - \omega$$

Since the domain for unique representation (the fundamental zone) of the 2D rotation space is $[0, 2\pi)$, if only the rotational symmetries are considered the fundamental zone is $[0, 2\pi/n)$. But applying the additional grain exchange symmetry equivalence relation reduces the fundamental zone to $[0, \pi/n]$. The connectivity in this case is very different from the case of rotation and orientation spaces. The end points of the fundamental zone $\omega = 0$ and $\omega = \pi/n$ represent distinct misorientations. Hence, the misorientation space represented using ω is a one-to-one and continuous mapping with a continuous inverse. The grain boundary misorientation space can therefore be embedded in one-dimensional Euclidean space $\mathbb{R}^1$.

The grain boundary misorientation spaces for systems C_1 and C_2 are color coded using only one variable (contrast) and shown in Figure 2.1(c&d). The purpose of this illustration is to point out the role of symmetry in the representations. For grain boundary misorientations, the coloring indicates the presence of mirror-lines at the boundaries (points in this case) of the fundamental zone. In contrast, for rotation and orientation spaces, the boundaries of the fundamental zone are connected as indicated by the coloring scheme. The grain boundary misorientation space is equivalent to a closed interval on the real line and admits a trivial fundamental group. Any closed path can be continuously deformed into a single point. Hence the grain exchange symmetry leads to a simpler topology of the misorientation space for grain boundaries.

2.3. Three-Dimensional Crystal Systems

2.3.1. Three-Dimensional Rotation Space

Embedding: None of the parameterizations mentioned in section 1.1.1, except for the group of special orthogonal matrices $SO(3)$, provide a one-to-one and continuous mapping for the rotation space. The rotation matrices parameterize the group of rotations in a one-to-one, continuous manner with a continuous inverse. This establishes an embedding of the rotation space in $\mathbb{R}^9$, but nine is not the minimum Euclidean dimension for an embedding of the rotation space. An embedding in six-dimensional Euclidean space [57] can be obtained from the orthogonality property of the rotation matrices. Eventually, Hopf [81] showed that five is the minimum number of variables required to parameterize the rotation space in a continuous and bijective manner.

This embedding property of $SO(3)$ is most easily appreciated using the quaternion parameterization, which relates the rotation space to the 3-sphere (S^3). The group of unit

quaternions is related to $SO(3)$ by a two-to-one homomorphism [82]. Since $+\mathbf{q}$ represents the rotation $(\omega, \vec{a})$ and $-\mathbf{q}$ represents $(2\pi + \omega, \vec{a})$, and the rotation $(\omega, \vec{a})$ is equivalent to the rotation $(2\pi + \omega, \vec{a})$, the equivalence relation $\mathbf{q} \sim -\mathbf{q}$ holds. There therefore exists a two-to-one homomorphism between unit quaternions and the rotation space. Using this equivalence, it is observed that the topology of the rotation space $SO(3)$ is the 3-sphere with diametrically opposite points (antipodal points) identified. Such a topological space is called the real projective space $\mathbb{RP^3}$ and is topologically equivalent to the rotation space. Hopf [81] showed that $\mathbb{RP^3}$ embeds in $\mathbb{R}^5$ and five is the minimum number of variables required to parameterize the rotation space in a continuous and bijective manner.

Fundamental Group: To understand the property of simply connectedness, it is first necessary to visualize the rotation space. We prefer the quaternion parameterization for the representation of the rotation space not only because it is valuable for understanding the embedding property of the rotation space, but also because of other advantageous properties such as absence of singularities [59] and intuitiveness due its direct relation to the axis-angle parameters (Equation (1.2)). The only caveat of working with the quaternion representation is that it contains a redundant fourth variable, with the sum of squares of the quaternion parameters equal to unity. This raises the issue of projecting the 4-dimensional quaternion space into three dimensions.

Visualization of the rotation space: Since there exists a two-to-one homeomorphism between the quaternion space and the rotation space ($\mathbf{q} \sim -\mathbf{q}$) it is enough to project only half of the 3-sphere to completely visualize the rotation space in $\mathbb{R}^3$. Commonly used projection schemes include:

(a) Orthogonal projection: $\vec{q} \equiv (q_1, q_2, q_3) \equiv \vec{a} \sin\frac{\omega}{2}$

(b) Geodesic projection (Rodrigues-vector map): $\vec{r} \equiv \left(\frac{q_1}{q_0}, \frac{q_2}{q_0}, \frac{q_3}{q_0}\right) \equiv \vec{a} \tan\frac{\omega}{2}$

(c) Stereographic projection: $\vec{r} \equiv \left(\frac{q_1}{1+q_0}, \frac{q_2}{1+q_0}, \frac{q_3}{1+q_0}\right) \equiv \vec{a}\left[2\tan\frac{\omega}{4}\right]$

(2.2)

(d) Homochoric (volume-preserving) projection: $\vec{r} \equiv \vec{a}\left[\frac{3}{2}\left(\frac{\omega}{2} - \sin\frac{\omega}{2}\cos\frac{\omega}{2}\right)\right]^{1/3}$

These projections are appropriate for visualization of rotations in $\mathbb{R}^3$ because of their direct relation to the axis-angle parameters; any vector $\vec{r}$ lies along the axis of rotation and its

magnitude is directly proportional to a monotonously increasing function, $f(\omega)$, of the rotation angle. It is important to note that these projections involve no loss of information and no sectioning of the space: they simply remove the redundant fourth variable in the quaternion parameterization, and present rotations (which comprise three independent parameters) in three-dimensional space. In each case the result is essentially a solid ball (shown in Figure 2.2(a)) where the origin represents the identity (no rotation), the outer surface represents a rotation of π, and the distance along any vector from the origin follows the rotation angle as $f(\omega)$. Each projection scheme in Equation (2.2) has its own merits, and the selection of a preferred mapping depends on the type of information that needs to be presented. Since the topological aspects of the rotation space do not depend on the projection scheme, the orthogonal projection will be used in this chapter because of its simplicity.
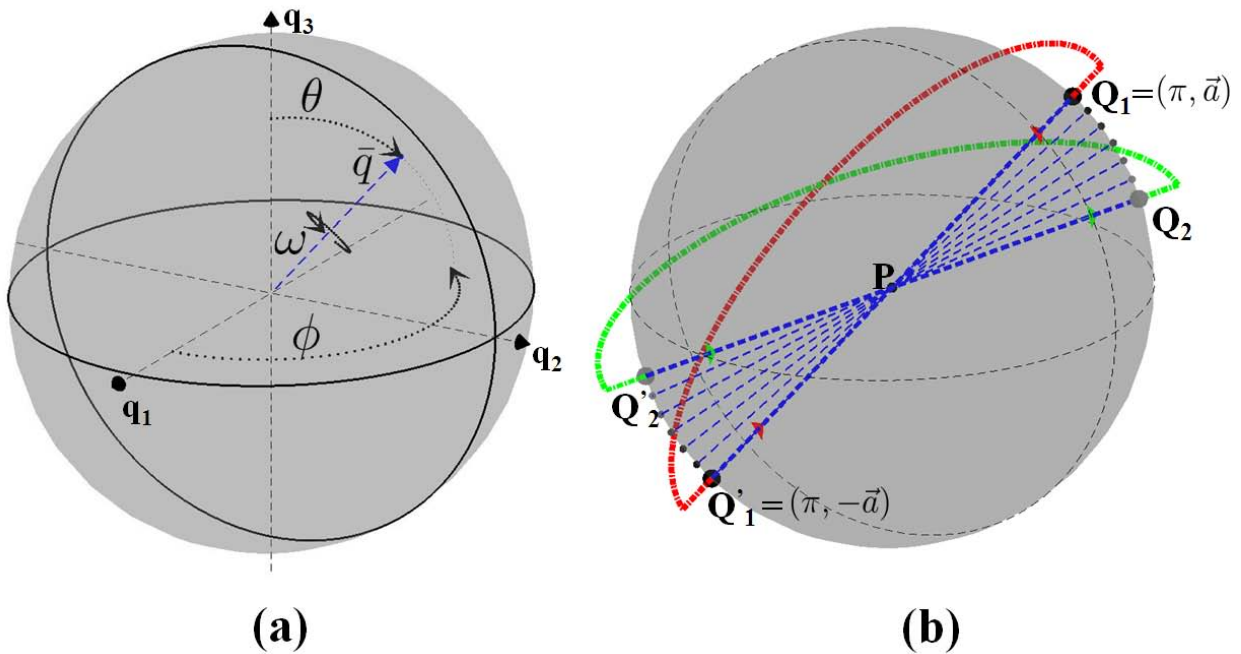
Figure 2.2 (a) A parametric ball built using the quaternion vector parameter $\vec{q} = \vec{a}\,sin\left(\frac{\omega}{2}\right)$ that represents the rotation space in $\mathbb{R}^3$. The polar coordinates (θ, ϕ) define the axis of rotation $\vec{a}$ and ω is the angle of rotation. (b) The antipodal points, on the surface of the parametric ball, $Q_1 = (\pi, \vec{a})$ and $Q'_1 = (\pi, -\vec{a})$ represent the same rotation and are identified. The closed path $PQ_2Q'_2P$ is obtained by continuously deforming the path $PQ_1Q'_1P$.

Every point in the solid ball represents a unique rotation except for the points on its surface. Each surface point corresponds to a rotation of π about the axis defined by the vector that joins it to

the origin. And, since any rotation $\pi, \vec{a}$ is equivalent to the rotation $(\pi, -\vec{a})$, the diametrically opposite surface points of the parametric ball represent the same rotation; these points (shown in Figure 2.2(b) as points Q_1 and Q_1') are identified, resulting in a space that is not simply connected.

To illustrate this property, we use a construction, developed by Wigner [83], for the rotation space to examine closed paths. Shown in Figure 2.2(b) are paths of two kinds: one that comprises a discontinuity or a *jump* (blue paths with colored jumps) and the other that is continuous and completely contained within the space (dashed black line). It is indeed possible to continuously shrink the dashed black line into the origin. To shrink the path $PQ_1Q_1'P$ to a point, first, the discontinuous jump in the path needs to be removed. As shown in Figure 2.2(b), the initial path $PQ_1Q_1'P$ can be distorted continuously to a great extent, for example to the path $PQ_2Q_2'P$, but the two surface points that define the jump (Q, Q') are always diametrically opposite and the jump can never be removed. Hence, the path $PQ_1Q_1'P$ cannot be continuously shrunk to a point illustrating that the rotation space is not simply connected.

To evaluate the fundamental group of the rotation space explicitly, the class of manifolds called as the spherical 3-manifolds [84, 85] is introduced. A spherical 3-manifold is defined as the quotient space obtained by a *properly discontinuous* [86] action of a finite subgroup Γ of the four-dimensional rotation group $SO(4)$ on the 3-sphere, and are denoted by S^3/Γ. Such a spherical 3-manifold has a finite fundamental group Γ and is not simply connected. The simplest example of a spherical 3-manifold is the rotation space itself. The rotation space $SO(3)$ is equivalent to S^3/Γ where Γ is the binary cyclic rotation group C_2^* consisting of the identity (I_4) and the inversion $(-I_4)$ operations. Hence, the fundamental group of $SO(3)$ is the binary cyclic rotation group C_2^* and is not simply connected. This topological property makes the embedding of the rotation space in three-dimensional Euclidean space impossible.

2.3.2. Orientation Spaces for three-dimensional crystal systems

The orientation spaces have a finite fundamental group as well and are not simply connected. A graphical interpretation of this property for orientation spaces is shown in Figure 2.3 for the case of the octahedral $O(432)$ orientation space. The jump in 432-orientation space has a similar character as the discontinuity observed in the closed paths of the rotation space. When a path

intersects the surface at point Q it reenters the space at a point that is obtained by rotating point Q through a certain angle and reflecting it onto the opposite surface (Q'); this jump has a skewed character reminiscent of a Möbius strip [58]. No amount of distortion can remove the jump as the points Q, Q' are always on opposite faces of the orientation space. The closed path $PQ_1Q_1'P$ can never be continuously shrunk into a point and hence the 432-orientation space is not simply connected.
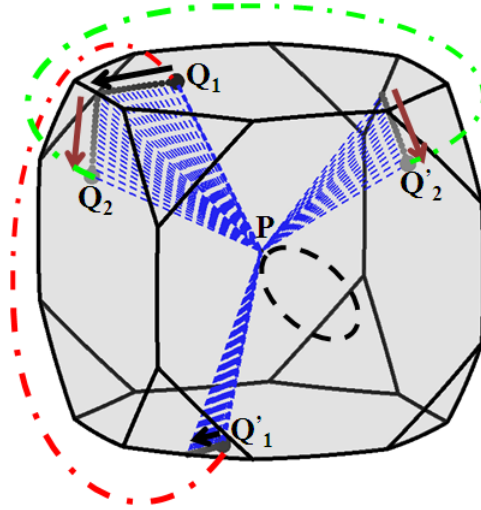
Figure 2.3 Path connectivity in the 432-orientation space. The dashed black line represents a continuous path completely contained within the space. The dashed blue lines represent paths with a jump (shown using green and red dashed lines).

The explicit fundamental group of the orientation spaces is obtained by observing that the orientation spaces of all crystal systems can be classified as spherical 3-manifolds, i.e. the orientation spaces can be expressed as S^3/Γ by a suitable choice of Γ. The relation between subgroups of $SO(3)$ and the finite subgroup Γ of $SO(4)$ is obtained by using the following property of $SO(4)$: the quotient space of $SO(4)$ about its centre ($\pm I_4$: the identity and inversion operation) is isomorphic to the product group $SO(3) \times SO(3)$. Hence a finite subgroup Γ of $SO(4)$ can be determined from the finite subgroups G_L and G_R of $SO(3)$ which correspond to the point groups of the phases involved. For example, in the case of the orientation space of $D_2(222)$, G_L is the identity element (I_3) and G_R is the dihedral group D_2 of $SO(3)$. Since Γ is the preimage of the product group $I_3 \times D_2$ (which is equivalent to D_2) in $SO(4)$, it is the binary dihedral group D_2^*. Similarly, the orientation spaces of point groups $C_1(1)$, $C_2(2)$, $C_3(3)$, $C_4(4)$ and $C_6(6)$ belong to the class of spherical 3-manifolds where the subgroup Γ (and hence the

fundamental group) corresponds to binary cyclic groups $C_2^*, C_4^*, C_6^*, C_8^*$ and C_{12}^* respectively (note that C_1-orientation space is the rotation space). The orientation spaces of D_2 (222), D_3 (32), D_4 (422) and D_6 (622) are spherical 3-manifolds obtained by action of corresponding binary dihedral groups. The orientation spaces of point groups $T(23)$ and $O(432)$ are obtained by the action of binary tetrahedral and binary octahedral group respectively [85].

Regarding embedding of the spherical 3-manifolds, literature only exists [87] for the orientation spaces of point groups $C_1(1)$, $C_2(2)$, $C_3(3)$, $C_4(4)$ and $C_6(6)$. The orientation spaces of these point groups belong to a class of spherical 3-manifolds called the lens spaces $L(p,q)$, and are $L(2,1)$, $L(4,1)$, $L(6,1)$, $L(8,1)$ and $L(12,1)$ respectively. According to [88], these lens spaces do not embed into $\mathbb{R}^4$; however they all smoothly embed in $\mathbb{R}^5$ [89]. To summarize, prior work has established that the fundamental groups of the orientation spaces are isomorphic to the corresponding Γ, the finite subgroup of $SO(4)$, and hence are not simply connected. The lens spaces require a minimum of five Euclidean dimensions for embedding. The orientation spaces are all closed 3-manfiolds which are not simply connected and cannot be embedded in three dimensions.

2.3.3. Grain boundary Misorientation Spaces for three-dimensional Crystal Systems

In the case of grain boundary misorientations, the equivalence relations shown in Equation (1.8) apply. The crucial relation here is the grain exchange symmetry $M \sim M^{-1}$. This symmetry relation cannot be expressed in terms of a rotation operation on S^3. In order to realize the effect of the grain exchange symmetry on the topological properties of the 3D rotation space we again consider the parametric ball of Figure 2.2(a). In the absence of equivalence relations, every point inside the solid parametric ball represents a unique rotation, while for rotations that correspond to the surface ($\omega = \pi$) there exist two points (antipodal points) that represent the same rotation as illustrated in Figure 2.2(b). In what follows we discuss the changes in this situation that arise when the grain exchange symmetry is added to the crystal symmetries.

2.3.3.1. Point Group $C_1(1)$

Since the solid parametric ball considered here is an orthographic projection of the four-dimensional quaternion space (i.e. the q_0 component of the quaternion is dropped), every point is given by the q_1, q_2, q_3 components of the quaternion. The equivalence relation $M \sim M^{-1}$ implies

that $(q_0, q_1, q_2, q_3) \sim (q_0, -q_1, -q_2, -q_3)$. In the orthographic projection this relation is equivalent to $(q_1, q_2, q_3) \sim (-q_1, -q_2, -q_3)$, so the grain exchange symmetry $M \sim M^{-1}$ introduces an inversion center at the origin in the solid parametric ball, as shown in Figure 2.4(a). Due to this additional equivalence relation, the fundamental zone can now be represented in a hemisphere with positive q_3 component (Figure 2.4(b)), as any misorientation corresponding to a negative q_3 component has an equivalent description in the top half of the hemisphere.
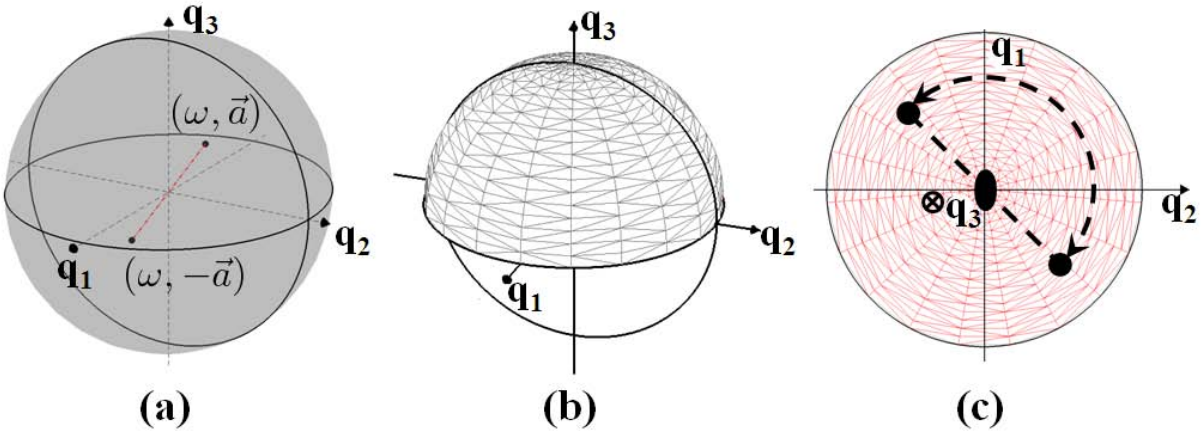
Figure 2.4 Grain boundary misorientation space of point group $C_1(1)$. (a) Represents the symmetry $\vec{q} \sim -\vec{q}$ in the rotation space introduced by the grain exchange symmetry ($M \sim M^{-1}$). (b) The fundamental zone of $C_1(1)$ grain boundary misorientation space. (c) Represents the symmetry $(q_1, q_2, 0) \sim (-q_1, -q_2, 0)$ on the plane $q_3 = 0$ of the fundamental zone. This symmetry is equivalent to a two-fold rotational symmetry in the plane $q_3 = 0$.

The connectivity of this system can be understood by looking at the surfaces of this fundamental zone. The fundamental zone is bounded by two surfaces: (a) the top hemispherical shell and (b) the bottom plane $(q_3 = 0)$. Every point inside the fundamental zone is unique in the sense that there are no equivalent descriptions in the fundamental zone. This is also true for the points on the hemispherical surface, where distinct points represent distinct misorientations. But for the points on the bottom plane, the inverse of any point $(q_1, q_2, 0)$ is $(-q_1, -q_2, 0)$ and lies in the same plane. Therefore, there exist two distinct points that represent equivalent misorientations corresponding to the $q_3 = 0$ plane of the fundamental zone as illustrated in Figure 2.4(c). The inversion center in the plane can also be considered as a two-fold rotation, since the action of an inversion center and two-fold rotation are the same in a plane. A path that intersects this plane, such as the path $PQ_1Q_1'P$ shown in Figure 2.5(a), can be continuously deformed into a point.

Another crucial difference here is that the top hemispherical surface acts as a *boundary* (defined as the surface with the property that a path that intersects this surface gets reflected back into the fundamental zone at the same point; this is illustrated graphically for two paths in Figure 2.5(b)) for this space. The rotation and the orientation spaces are boundary free. The grain exchange symmetry thus results in a simply connected space with a boundary. The fundamental zone is equivalent to a cone space on the real projective plane $\mathbb{R}P^2$ [90] which admits a trivial fundamental group [91]. Hence the rotation space with just the grain exchange symmetry applied, which is the grain boundary misorientation space of the C_1 system, is simply connected.
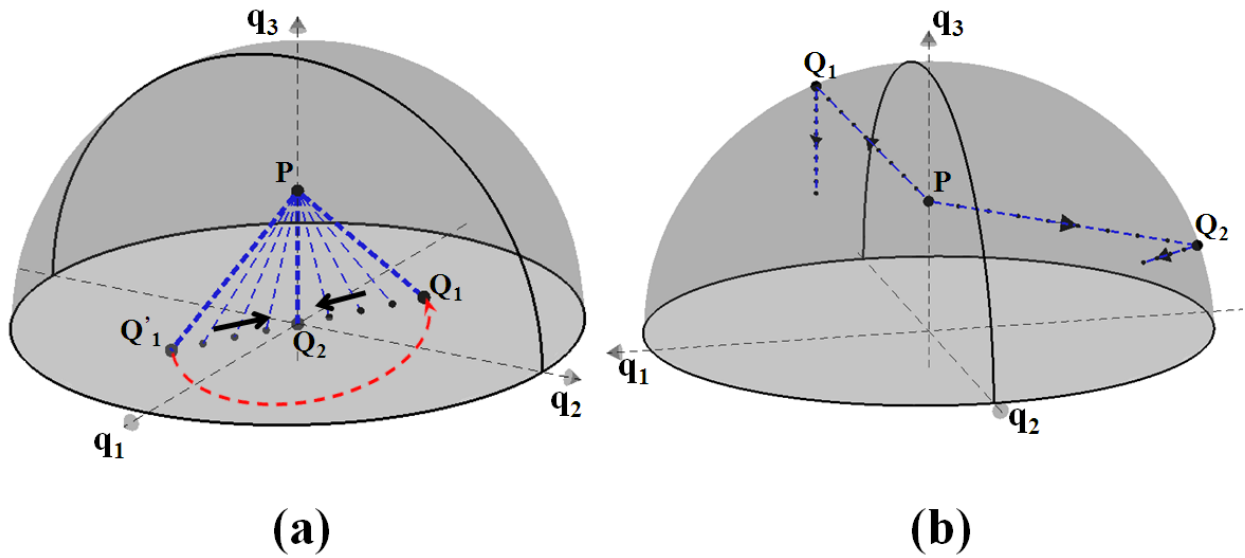
Figure 2.5 The character of the surfaces of $C_1(1)$ grain boundary misorientation space: (a) the dashed blue lines represent closed paths and the discontinuity in the path $PQ_1Q_1'P$ can be removed by continuously moving point Q_1 towards the origin. (b) The hemispherical surface $\left(q_1^2 + q_2^2 + q_3^2 = 1\right)$ of the misorientation space acts as a *boundary*. Any path that intersects this surface gets reflected back into the fundamental zone at the same point.

2.3.3.2. Point Groups $C_2(2)$, $C_3(3)$, $C_4(4)$, $C_6(6)$ and $D_3(32)$

For the misorientation spaces of systems that exhibit crystal symmetries, the equivalence relations involve the symmetry operations that belong to the point symmetry group of the crystal in addition to the grain exchange symmetry. In this section we show that the topologies of misorientation spaces of point groups C_2 (2), C_3 (3), C_4 (4), C_6 (6) and D_3 (32) are all equivalent to that of the C_1 (1) misorientation space. The fundamental zones of the

misorientation spaces for these point groups are derived by Grimmer [72] and are shown in Figure 2.6, in three different perspective views labelled (i), (ii) and (iii). As we shall develop in the following, the colors used to plot the surfaces of the fundamental zones correspond to the type of symmetries present on them. The surfaces with rotational symmetries are colored red and boundary surfaces are colored grey; other colors (blue, cyan, magenta and pink) are used to represent surfaces with mirror-line symmetries.

The fundamental zone for C_2 (2) misorientation space is shown in Figure 2.6(a). Every distinct point inside the fundamental zone represents a unique misorientation. The fundamental zone is bounded by three surfaces: a) the plane OAB ($q_3 = 0$) b) the plane $OACB$ ($q_2 = 0$) and c) the curved surface ABC. The symmetries on these surfaces are shown in Figure 2.6(a)(ii) & Figure 2.6(a)(iii). The plane $q_3 = 0$ does not have any symmetry (hence represents a boundary). The plane $OACB$ has a mirror-line symmetry along the line OC. The surface ABC has a four-fold rotational symmetry along the q_3 axis.

The fundamental zones for systems C_3 (3), C_4 (4) and C_6 (6) with symmetries on their surfaces are shown in Figure 2.6(b), Figure 2.6(c) and Figure 2.6(d), respectively. It can be seen that the fundamental zones for these systems are also bounded by the same three types of surfaces as we have just seen for the C_2 system: the planes of type OAB ($q_3 = 0$) are surfaces that represent boundaries, those of type $OACB$ have mirror-line symmetry along OC, and the curved surfaces of type ABC have rotational symmetries (six-fold symmetry for C_3, eight-fold for C_4 and twelve-fold symmetry for C_6). The similarity between these four spaces is consequential; they are in fact topologically equivalent. This is illustrated through a series of continuous deformations in Figure 2.7. We begin with an object that is topologically equivalent to the fundamental zone of the C_6 system. Figure 2.7(a) is obtained by stretching Figure 2.6(d)(i) continuously in the radial direction. Hence, Figure 2.6(d)(i) and Figure 2.7(a) are topologically equivalent. The next step of deformation is along the angular direction. The object in Figure 2.7(a) is stretched such that only the φ (angular) coordinate of the points change. The deformation from Figure 2.7(a) to Figure 2.7(b) is such that if the fundamental zone is expressed in polar coordinates (r, θ, φ), then the mapping is $\varphi \to \frac{4}{6}\varphi$. The object in Figure 2.7(b) is topologically equivalent to Figure 2.7(c)(i) and they differ only by a stretch along the radial direction.
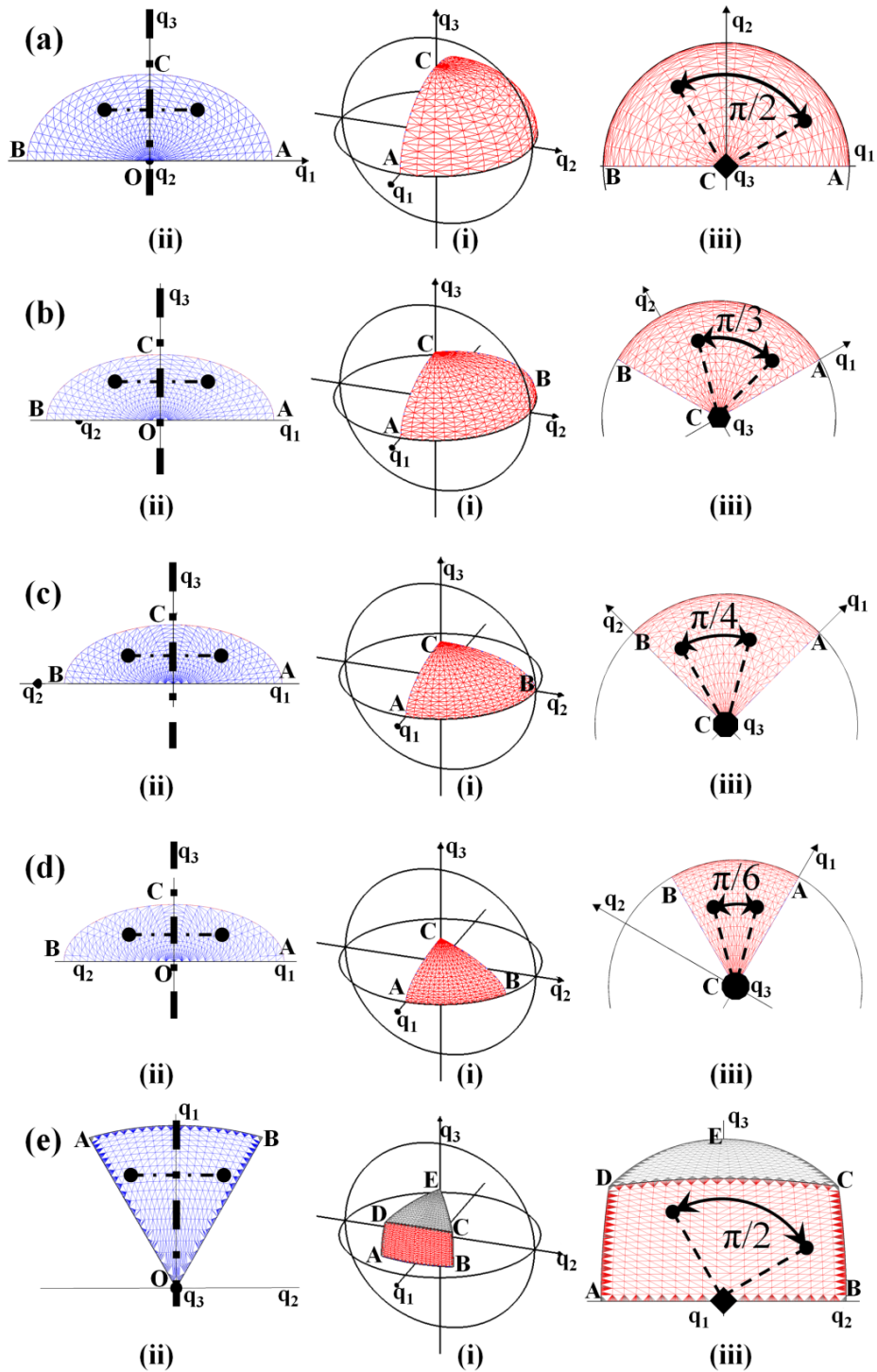
Figure 2.6 Grain boundary misorientation spaces with surface symmetries of point groups (a) $C_2(2)$, (b) $C_3(3)$, (c) $C_4(4)$, (d) $C_6(6)$ and (e) $D_3(32)$. (i),(ii) & (iii) show the fundamental zones from different views to illustrate the symmetries on their surfaces. The surfaces with rotational and mirror-line symmetries are colored red and blue respectively and the boundary surfaces are colored grey.

Hence, the misorientation space of the C_6 system is topologically equivalent to that of the C_4 system. Similar deformations establish the topological equivalence between systems C_4 (Figure 2.6(b)), C_3 (Figure 2.6(c)) and C_2 (Figure 2.6(d)).
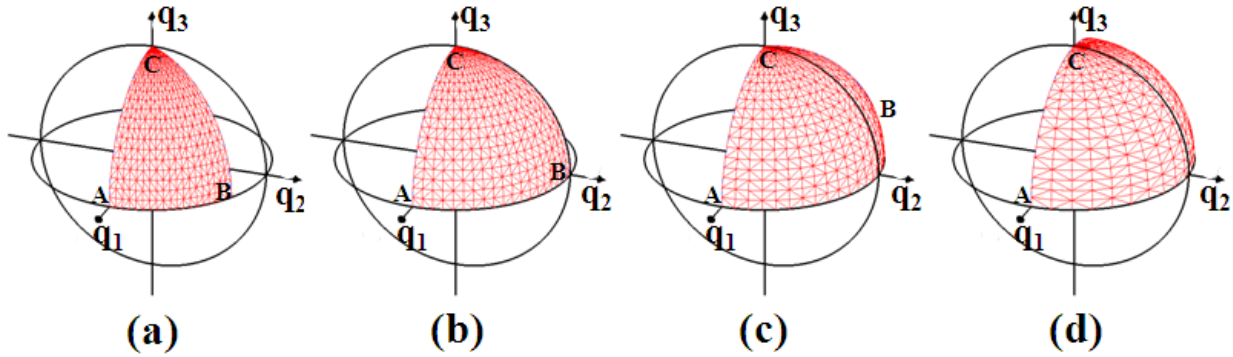
Figure 2.7 (a),(b),(c) and (d) represent misorientation fundamental zones of systems $C_6(6)$, $C_4(4)$, $C_3(3)$ and $C_2(2)$, respectively, stretched along the q_3 axis. A continuous deformation in the angular direction illustrates the topological equivalence between these spaces.

The topological equivalence between the C_2 and C_1 misorientation fundamental zones can be established by additional continuous deformation steps as shown in Figure 2.8. The first sequence of steps (Figure 2.8 (a) to Figure 2.8(c)) involve angular stretching similar to that seen earlier in Figure 2.7. The object in Figure 2.8(c) is a hemisphere with two-fold symmetry on the spherical surface of the hemisphere. Other points inside the volume and on the surface $q_3 = 0$ represent distinct misorientations. The planes OAC and OBC are glued together, which is allowed because of the mirror symmetry on the plane $OACB$. Further deformation steps (Figure 2.8 (c) to Figure 2.8(h)) involve impressing the top hemispherical solid into the bottom half such that the top hemispherical surface now becomes the plane $q_3 = 0$ and the plane $q_3 = 0$ is deformed into the bottom hemispherical surface. A rotation of π along the x-axis will now result in an object identical to the misorientation fundamental zone of the C_1 system with a two-fold rotational symmetry on the $q_3 = 0$ plane. This demonstrates the topological equivalence between the misorientation spaces of the point groups C_1, C_2, C_3, C_4 and C_6.

Figure 2.8 A continuous deformation sequence illustrating topological equivalence between $C_2(2)$ and $C_1(1)$ grain boundary misorientation spaces.

The misorientation space for point group D_3 is more complicated than those described above. The fundamental zone and the symmetries on its surfaces are shown in Figure 2.6(e), and we note that they consist of similar symmetries as the surfaces of the fundamental zone of C_2. The surface $ABCD$ consists of a four-fold rotational symmetry (similar to the surface ABC of C_2 as shown in Figure 2.6(a)(iii)) and the surface OAB contains a mirror-line (similar to the surface $OACB$ of C_2 as shown in Figure 2.6(a)(ii)). This fundamental zone can be continuously deformed into the C_2 fundamental zone as shown through various deformation steps in Figure 2.9. Hence, the misorientation space of the point group D_3 is topologically equivalent to C_2. This implies that the minimum dimension of Euclidean space in which the misorientation spaces for systems $C_1(1)$, $C_2(2)$, $C_3(3)$, $C_4(4)$, $C_6(6)$ and D_3 (32) can be embedded is the same and they are all topologically equivalent.

The mappings between the various misorientation spaces of these point groups are given in **Appendix A** in analytical form (Equations (A1),(A2),(A3) and (A4)), corresponding to the specific deformations illustrated in Figure 2.7, Figure 2.8 and Figure 2.9. The minimum dimension which these systems can be embedded into is still unclear and is a topic for future research. However, these spaces cannot be embedded in the three-dimensional Euclidean space.

49

As already mentioned, the C_1 misorientation space is equivalent to a cone of $\mathbb{R}P^2$ and an embedding of C_1 in $\mathbb{R}^3$ would give an embedding of $\mathbb{R}P^2$ in $\mathbb{R}^3$ which is impossible [92].
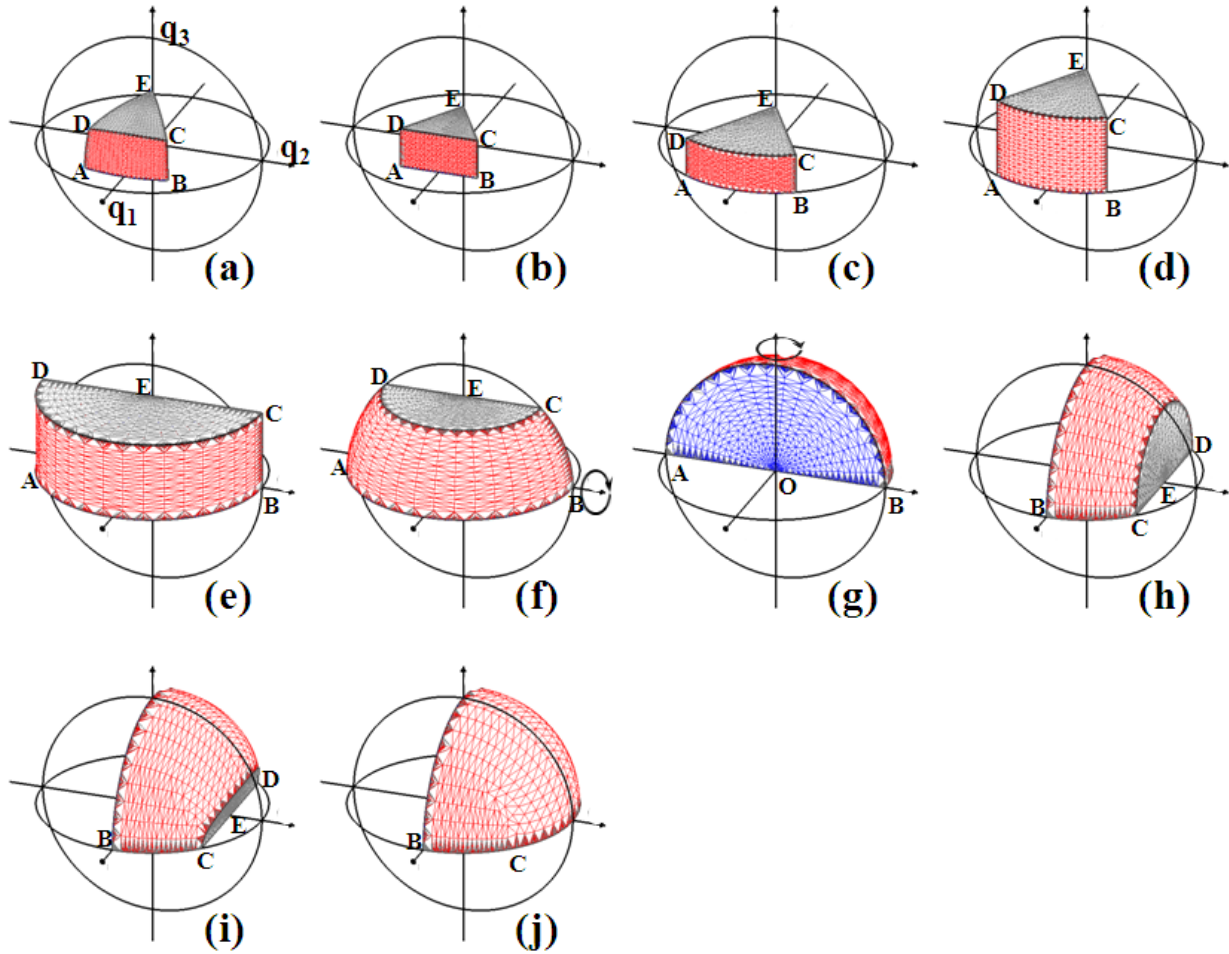
Figure 2.9 A continuous deformation sequence illustrating topological equivalence between $D_3(32)$ and $C_2(2)$ grain boundary misorientation spaces.

2.3.3.3. Point Groups D_2(222), D_4(422), D_6(622), T(23) and O(432)

The fundamental zones for the misorientation spaces of point groups D_2 (222), D_4 (422), D_6(622) and O(432) were derived by Grimmer [72], while that for point group T(23) was illustrated by Morawiec [93]. Figure 2.10 shows the fundamental zones for these point groups, along with the symmetries on their surfaces. The topology of these fundamental zones is highlighted by the fact that the surfaces either have no symmetry on the surface (i.e. a boundary)

or they contain only mirror-line symmetries; in Figure 2.10 colored surfaces are those with mirror-line symmetries, while grey surfaces are boundaries. Fundamental zones with only mirror-line symmetries on their surfaces are simply connected spaces, as the path discontinuities that occur on these surfaces can be removed by a continuous deformation of the path. Shown in Figure 2.11 are illustrations of closed paths of the type $PQ_1Q_1'P$ in the $D_2(222)$ and $O(432)$ fundamental zones. This path can be continuously deformed such that the points Q_1 and Q_1' converge onto Q_2 on the symmetry line AG (or AC) and the path PQ_2P can now be continuously shrunk to the point P. Hence the misorientation spaces of D_2 and O are simply connected. The same holds for the misorientation spaces of D_4, D_6 and T.

Figure 2.10 Fundamental zones in orthographic projection of quaternion space for (a) $D_2(222)$ (b) $D_4(422)$ (c) $D_6(622)$ systems. These systems have three surfaces with mirror-line symmetries on them. The surfaces with mirror symmetries are colored (yellow, pink and magenta) and the surfaces with no symmetries are colored grey. Fundamental zones for (d) $T(23)$ and (e) $O(432)$ systems with the surface containing mirror symmetry colored blue.

Figure 2.11 The (a) $D_2(222)$ and (b) $O(432)$ grain boundary misorientation spaces are simply connected. The dashed blue lines represent closed paths and the discontinuity in the path $PQ_1Q_1'P$ can be removed by continuously moving point Q_1 onto the line (a) AG in $D_2(222)$ fundamental zone and the line (b) AC in $O(432)$ fundamental zone.

As observed in the deformation sequences for the C_2, C_3, C_4, C_6 and D_3 grain boundary misorientation spaces, the surfaces with mirror-line symmetries can be glued together and this removes path discontinuities that occur on these surfaces. However, since the grain boundary misorientation spaces of point groups D_2 (222), D_4 (422), $D_6(622)$, $T(23)$ and $O(432)$ consist of surfaces with only mirror-line symmetries these spaces can be deformed continuously so that all the discontinuities that occur in them can be removed; for these spaces it is possible to obtain an explicit one-to-one continuous mapping into $\mathbb{R}^3$. Both the grain exchange symmetry and the crystal symmetries are necessary to embed these spaces in $\mathbb{R}^3$. Application of the grain exchange symmetry simplifies the topology and results in simply connected spaces for $C_1(1)$, $C_2(2)$, $C_3(3)$, $C_4(4)$, $C_6(6)$ and D_3 (32) systems, but they cannot be embedded in $\mathbb{R}^3$; apparently it is only when a sufficient number of crystal symmetries are introduced that the spaces can be embedded in $\mathbb{R}^3$.
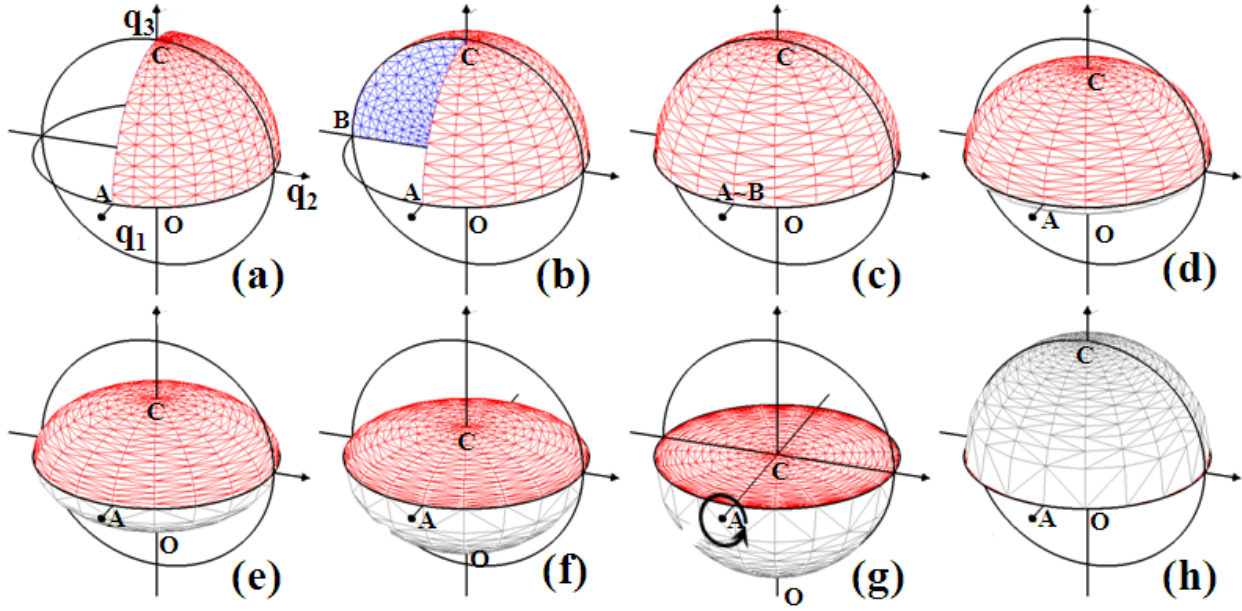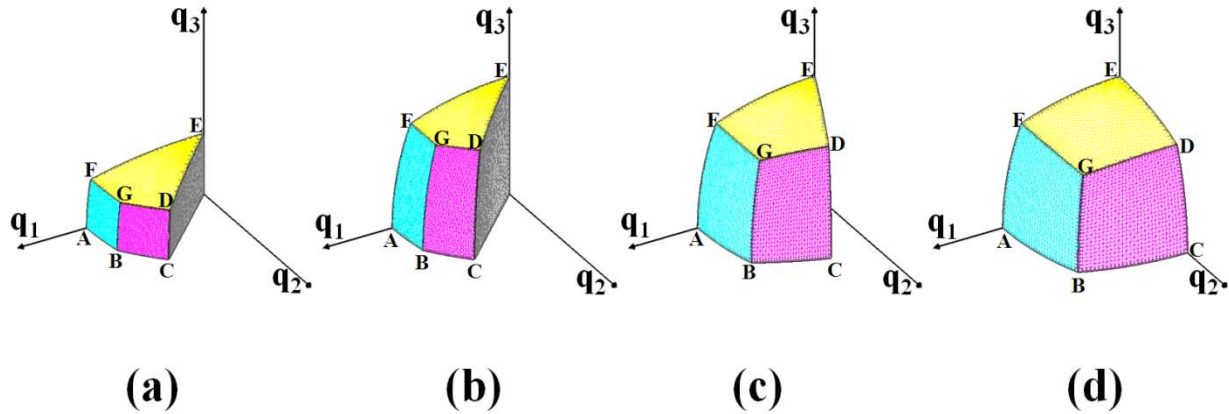
Figure 2.12 A continuous deformation sequence illustrating the topological equivalence between the grain boundary misorientation spaces of point groups $D_4(422)$ and $D_2(222)$.

To obtain an explicit one-to-one continuous mapping into $\mathbb{R}^3$, we deform these spaces by folding the surfaces with mirror-line symmetries. The misorientation fundamental zones of point groups D_2, D_4 and D_6 are very similar and their topological equivalence can be established through simple deformation steps from one space to the other as illustrated in Figure 2.12 for D_4 and D_2. The mappings from D_4 to D_2 and D_6 to D_2 are given in **Appendix A** as Equation (A6) and Equation (A7) respectively.

Since all three of these spaces are equivalent, establishing a mapping of D_2 into $\mathbb{R}^3$ is sufficient to address them all. The misorientation space of the D_2 system can be deformed continuously and the surfaces with mirror symmetries can be glued together such that it can be embedded in $\mathbb{R}^3$ as follows (Figure 2.13). First, Figure 2.13(b) is obtained by transforming the orthographic quaternion projection into that of Rodrigues vectors, which simplifies the space by rendering all the surfaces planar. Next, Figure 2.13(c) is obtained by simply rotating the cubic space such that the body diagonal coincides with the z-axis. Figure 2.13(e) is obtained by deforming the cube into a tetrahedron, which is then deformed into a hemisphere (Figure 2.13 (h)). The hemisphere is deformed into a sphere as shown in steps Figure 2.13(i,j,k). In these final deformation steps the mirror planes fold and glue together, also leading to a coincidence along the triple line between them, and resulting in a continuous mapping. This mapping from D_2 to $\mathbb{R}^3$ is expressed analytically in **Appendix A** in Equation (A8).
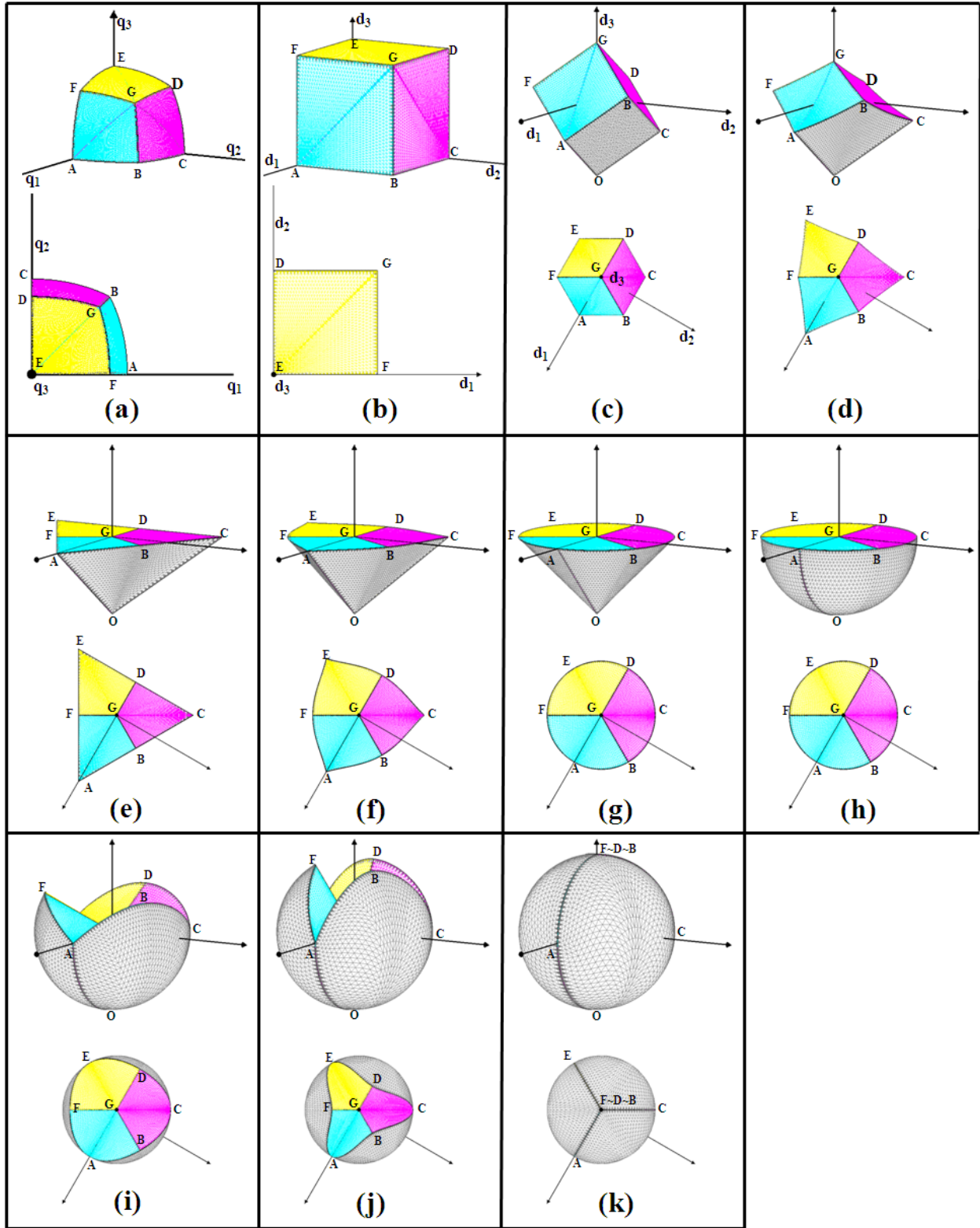
Figure 2.13 Deformation scheme representing the embedding of $D_2(222)$ grain boundary misorientation space in $\mathbb{R}^3$.

Hence, the systems D_2, D_4 and D_6 can be represented in a bijective and continuous manner using only three variables. These three variables can be used as color variables, and grain boundaries for these systems can be graphically represented using colors.

The fundamental zone of the tetragonal point group $T(23)$ is shown in Figure 2.10(d). The connectivity of the misorientation space for this system is different from the previous ones in the sense that only one mirror-line symmetry is present. The embedding of this system is shown through simple deformation schemes in Figure 2.14. The mapping is given in **Appendix A** in Equation (A9).

To obtain a one-to-one continuous mapping for the $O(432)$-misorientation space into the color space, the former must be deformed continuously so that the path discontinuities are removed. We have developed such a mapping, as illustrated in Figure 2.15, which shows a sequence of deformations that maps the 432-misorientation space into the shape of a cone, with no surfaces that induce path discontinuities. The cone shape was selected so that it can be directly fitted to the HSV color cone (see Figure 1.4c) to obtain a coloring scheme for misorientations. The most critical of the deformation steps is the folding of the space shown in frames Figure 2.15(h-j), which leads to the closure of the surface ABD upon itself in such a way that the path discontinuities are healed; the original two triangular planes ABC and ADC are glued together. The deformations shown graphically in Figure 2.15 may also be expressed analytically as shown in **Appendix A** in Equation (A10).
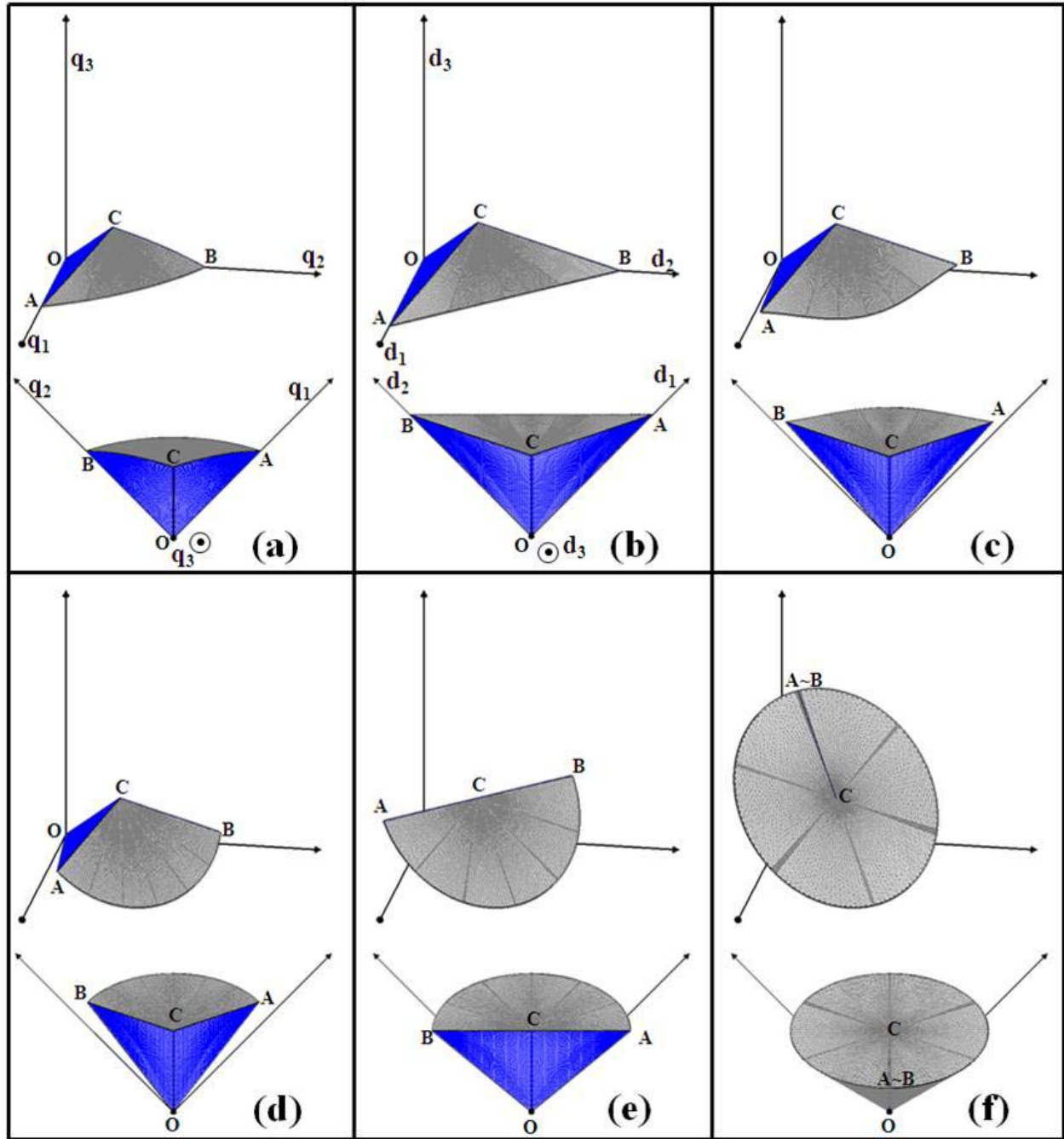
Figure 2.14 Deformation scheme representing the embedding of the grain boundary misorientation space of point group $T(23)$ in $\mathbb{R}^3$. Fundamental zone of $T(23)$ misorientation space in (a) orthographic projection of quaternion space and in (b) Rodrigues-vector representation. (c)-(e) The space is deformed continuously into a cone such that the surfaces related to each other with mirror symmetry are glued together.
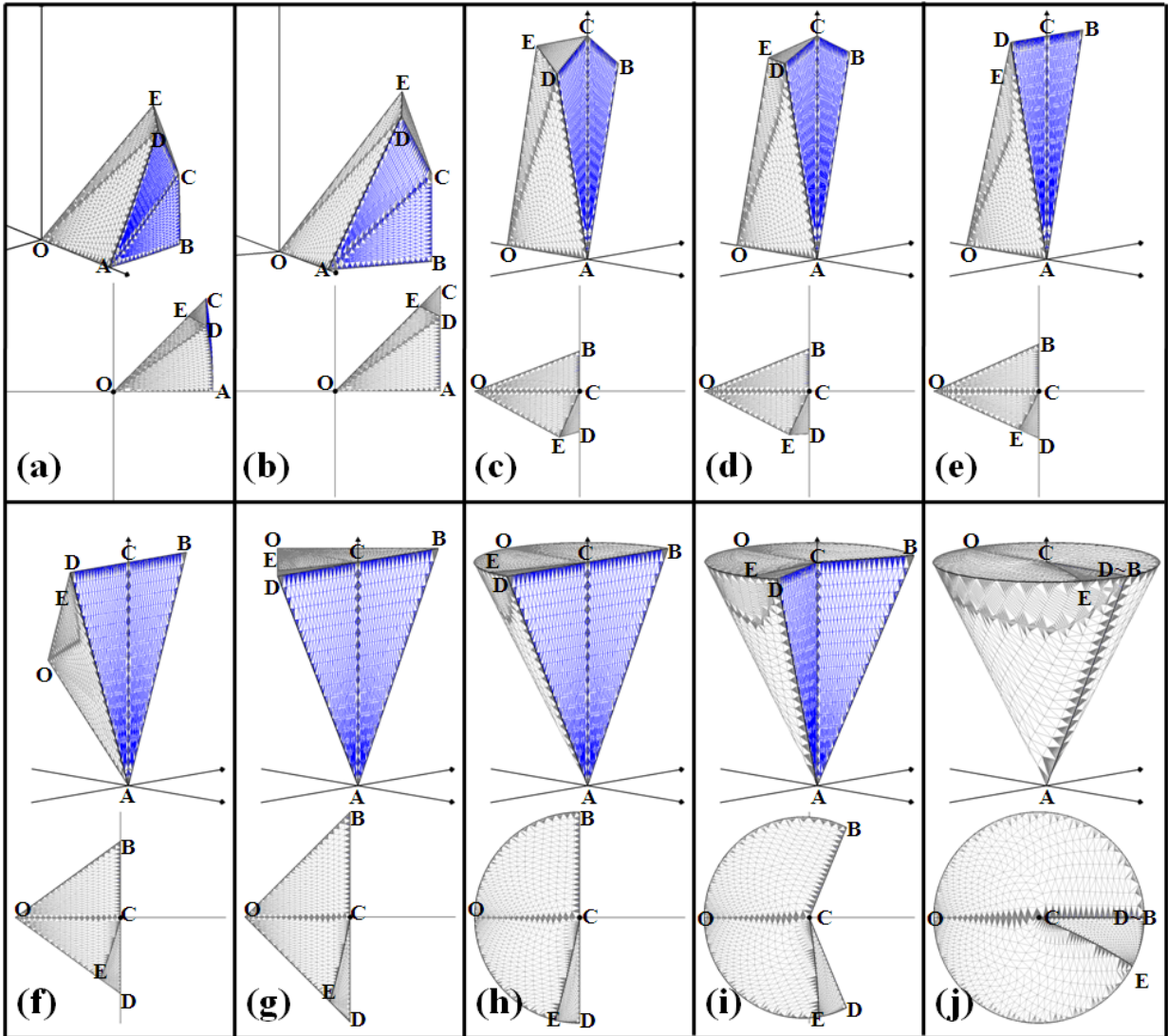
Figure 2.15 Continuous deformation of the 432-misorientation space. (a) Orthographic projection of 432-misorientation space (432-MS). (b) A continuous mapping into a Rodrigues-vector representation of 432-MS with straight edges and planes. (c-e) the same space subsequently rotated and surfaces flattened. (e-g) Continuous deformation of (e) into a prism. (g-h) Prism to a half-cone. (h-j) Half-cone to a cone. This deformation is an embedding of 432-MS in $\mathbb{R}^3$ and the final cone obtained is a simply connected space in $\mathbb{R}^3$.

2.4. Conclusions

The topological properties of orientation and grain boundary misorientation spaces have been examined. In the case of orientation spaces, the equivalence relations involve only rotational symmetries associated with the point symmetry of the crystals. These equivalence relations can be transformed to an action by a finite subgroup Γ of the four-dimensional rotations $SO(4)$ on the 3-sphere S^3. Hence, all the orientation spaces can be classified under the so-called spherical 3-manifolds with finite fundamental group Γ. These spaces are closed 3-manifolds; they are not simply connected and hence cannot be embedded in $\mathbb{R}^3$.

The topology of misorientation spaces between crystals of the same point group, however, is fundamentally different from the orientation spaces because of the "grain exchange symmetry", $M \sim M^{-1}$, which simplifies the topology and produces a boundary in the space. These grain boundary misorientation spaces can be divided into two groups. The first group comprises the systems $C_1(1)$, $C_2(2)$, $C_3(3)$, $C_4(4)$, $C_6(6)$ and D_3 (32), which are shown here to be topologically equivalent and simply connected. These cannot be embedded in $\mathbb{R}^3$, but can be embedded in $\mathbb{R}^5$ [89]. The second group consists of grain boundary misorientation spaces for systems $D_2(222)$, $D_4(422)$, $D_6(622)$, $T(23)$ and $O(432)$. These systems were also shown here to be topologically equivalent and simply connected, and they can be embedded in a three-dimensional Euclidean space. A three parameter representation that is continuous and bijective has been presented for these systems.

This is the first time parameterizations using three variables which are continuous and bijective have been proposed for the misorientation spaces of point groups $D_2(222)$, $D_4(422)$, $D_6(622)$, $T(23)$ and $O(432)$. Interestingly, these systems comprise orthorhombic, tetragonal, hexagonal and cubic crystals, which are the most common types of crystals in engineering materials. The results therefore apply quite broadly to the characterization, mapping, and study of grain boundaries in such systems. For example the three-dimensional parameterizations can be used as color variables to represent grain boundary information for these systems.

3. Application to EBSD Data

3.1. Introduction

In the previous chapter we proved that the grain boundary misorientation spaces of crystal systems with rotational point groups $D_2(222)$, $D_4(422)$, $D_6(622)$, $T(23)$ and $O(432)$ can be embedded in $\mathbb{R}^3$. The grain boundary misorientation spaces of point groups $D_2(222)$, $D_4(422)$ and $D_6(622)$ are continuously deformed into a sphere and misorientation spaces of point groups $T(23)$ and $O(432)$ are deformed into a cone. It is natural to map the sphere and the cone to the HSL color sphere HSV color cone respectively. The mapping sequence for grain boundary misorientation spaces of different point groups is summarized in the Figure 3.1 below.
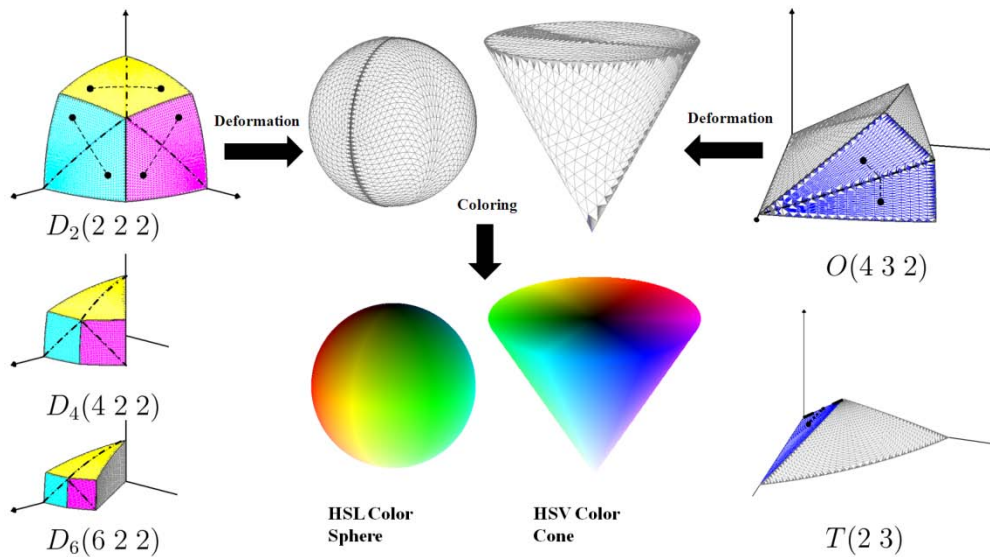
Figure 3.1 The grain boundary misorientation spaces that can be embedded in $\mathbb{R}^3$ are mapped to either the HSL Color Sphere or the HSV Color Cone.

Equipped with a continuous and one-to-one mapping from grain boundary misorientation spaces to the color space, we can represent grain boundary misorientation information more intuitively. A micrograph consisting of grain boundaries colored according to their misorientations with a legend for interpretation is called the "Grain Boundary Misorientation Map". In the following sections, we discuss how to visualize misorientation information and construct color legends for misorientation maps. The mappings of misorientations to three-dimensional Euclidean space may also be used to develop better coloring schemes for the orientations of individual grains. Improved representation schemes for orientations are discussed in section 3.4.

3.2. Visualization of the Misorientation Space

To infer misorientation information from color it is necessary to build a color legend. This is similar to the commonly used colored stereographic triangle as an inverse pole legend in EBSD micrographs. In order to construct a color legend, it is first necessary to visualize the misorientation space in a plane. As mentioned in section 2.2.1, we will be using the quaternion parameterization to represent rotations. Equations (2.2) show various projection schemes for projecting the unit-quaternion space into three-dimensions. We used the orthogonal projection in chapter 2 because of the simplicity of the projection scheme. But for the purpose of building a legend to infer misorientation information, we would like to use a projection scheme that will be consistently used by grain boundary engineers to represent misorientation information. Such consistency would facilitate the familiarity required with the legend for easier interpretation of the axis-angle information.

Another instance where complete misorientation information is represented is while presenting information of misorientation statistics. When it comes to the representation of statistics of rotations, i.e., populations of many rotations such as in texture analysis or misorientation distribution data, the most important criterion in choosing an appropriate projection scheme is the ability to visualize departures from randomness. Only the volume-preserving projection of Equation (2.2)(d) has the property that a random distribution of rotations appears uniformly distributed. For this reason it has been proposed [94] that the volume-preserving projection scheme should be exclusively used to map the misorientation space into $\mathbb{R}^3$. Therefore, we prefer using the same projection scheme to build color legends for grain boundary misorientation maps.

The volume projections render the misorientation space into its true form as a three-dimensional manifold, which must be further processed to present it in the plane; two-dimensional sections of the rotation space must be projected into $\mathbb{R}^2$. Usually, such sections are surfaces over which one parameter is kept constant, for example, constant Φ sections in the case of Euler angle parameterization [63]. The obvious disadvantage of such sections is the fact that the locus of points of constant Φ do not translate to any intuitive parameter of the rotation space. Instead, the most physical way of sectioning the misorientation space is using surfaces of constant misorientation angle ω. Such sections are inherently intuitive to materials scientists, because they correspond to the well-known standard stereographic triangles for the various point group

symmetries. The radius of the parametric ball (Figure 2.2) is a monotonic function of just the rotation angle and hence the locus of points of constant rotation angle is a sphere, which can be projected in $\mathbb{R}^2$ using one of the projection schemes described below in Equation (3.1). The stereographic projection and the area-preserving projection schemes are the two most common mappings of a spherical surface of radius r onto a plane. When expressed using polar coordinates (r, θ, ϕ), the mappings are:

(a) Stereographic projection: $2r \tan \frac{\theta}{2} (\cos \phi, \sin \phi)$

$$(3.1)$$

(b) Area-preserving projection: $\left[r\sqrt{2(1 - |\cos \theta|)} \right] (\cos \phi, \sin \phi)$

Keeping in mind the visualization of random distribution of misorientations, the sections of constant angle of rotation in the parametric ball (obtained using volume-preserving projection) are projected in $\mathbb{R}^2$ using the equal-area projection scheme described in Equation (3.1)(b).

In Figure 3.2, we show the steps involved in projecting the misorientation information for all the five point groups. Figures 3.2(a-e)(i) illustrate the volume-preserved projection of the fundamental zones which are colored according to mappings obtained in the previous chapter. An important point to note here is that the colors directly reflect the symmetries present on the surfaces of the fundamental zones. This is due to the fact that the mappings of the misorientation spaces to the color space are consistent with the topology (connectivity) of these spaces. Sections of constant misorientation angle in the fundamental zone and their projections in 2D (using area-preserving projection) are shown in Figures 3.2(a-e)(ii) and (a-e)(iii). Depending on the misorientation angle, two cases occur: (i) either the entire surface lies in the interior of the fundamental zone, in which case the projection is straightforward, (ii) or only a part of the surface lies within the fundamental zone. Sections that belong to the second category are shown. The area-preserving projections of these surfaces, shown in Figures 3.2(a-e)(iii), correspond to a part of the projected standard stereographic triangle. With the conventions for an intuitive projection scheme for representing and visualizing misorientation information established, we construct color legends for the grain boundary misorientation spaces of the five point groups that can be embedded in $\mathbb{R}^3$.
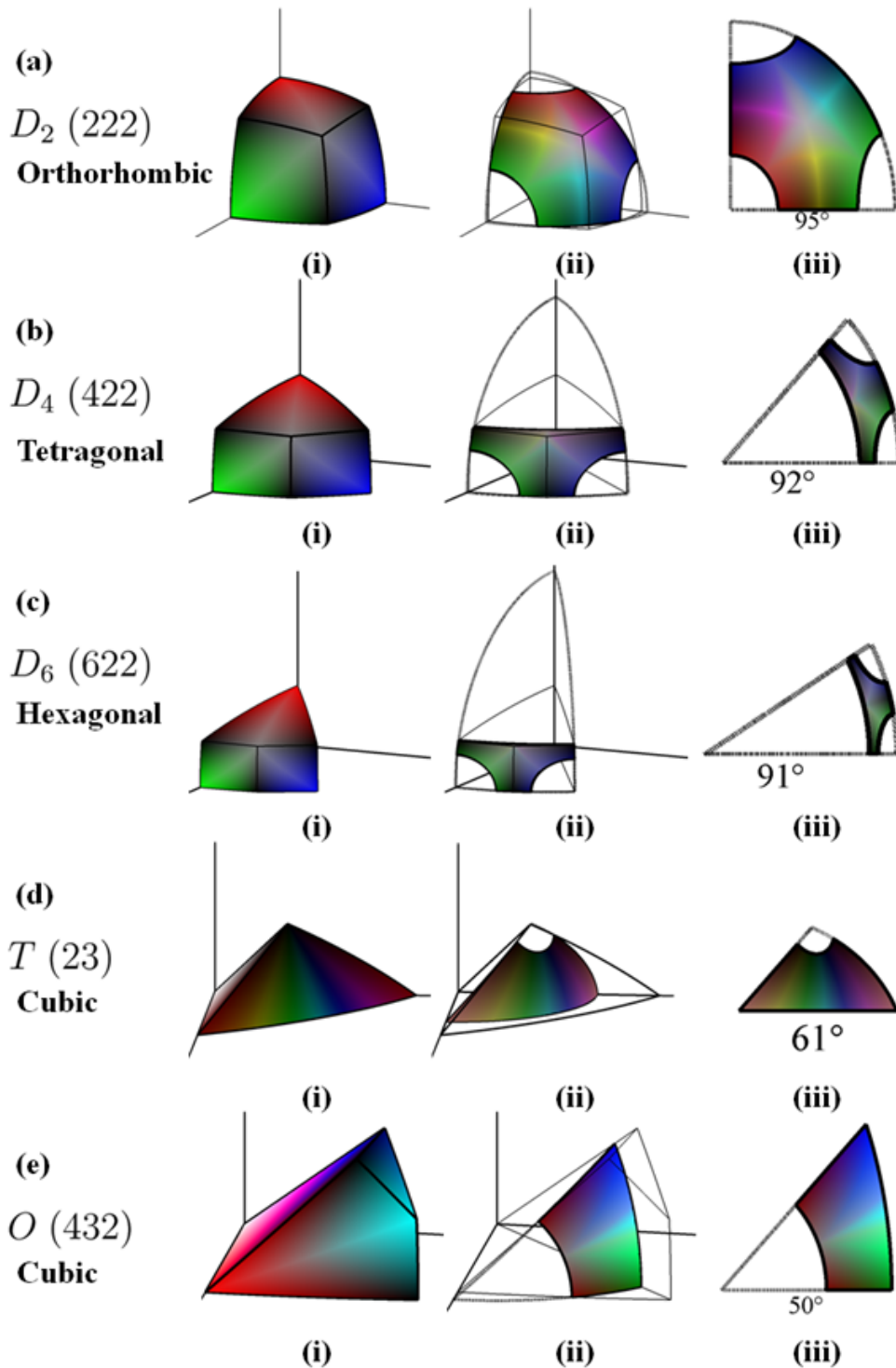
Figure 3.2 An illustration of the projection schemes used for visualizing misorientation spaces of (a) $D_2(222)$, (b) $D_4(422)$, (c) $D_6(622)$, (d) $T(23)$ and (e)$O(432)$. (i) Three-dimensional representation of the fundamental zones of misorientation spaces obtained by a volume-preserving projection of the four-dimensional quaternion space. (ii) Intersection of a surface of constant misorientation angle and the fundamental zone. (iii) Area-preserving projection of the two-dimensional section shown in (ii). In (i), (ii) and (iii) the misorientations are colored according to the mappings obtained in chapter 2.

3.2.1. Legends for Grain Boundary Misorientation Maps

The mappings in **Appendix A** are used to construct color legends for the grain boundary misorientation spaces using the aforementioned projection and sectioning schemes. The color legends are of $D_2(222)$, $D_4(422)$, $D_6(622)$, $T(23)$ and $O(432)$ misorientation spaces are presented shown in Figures 3.3, 3.4, 3.5, 3.6 and 3.7 respectively. The legends are a sequence of sections that each resembles the standard stereographic triangle of the corresponding point group; at large disorientation angles the standard region is truncated as the sectioning planes begin to exit the fundamental zone. Not only do the coloring schemes satisfy continuity and provide a unique color for every point in the space, but they have been constructed with several additional conveniences for intuitive interpretation. For example, the contrast maps generally to the disorientation angle: high angle misorientations have darker colors, and low angles correspond to lighter colors, with white being located at the apex ($\omega = 0$). Red, green, and blue colors are located at the corners of the standard triangles.
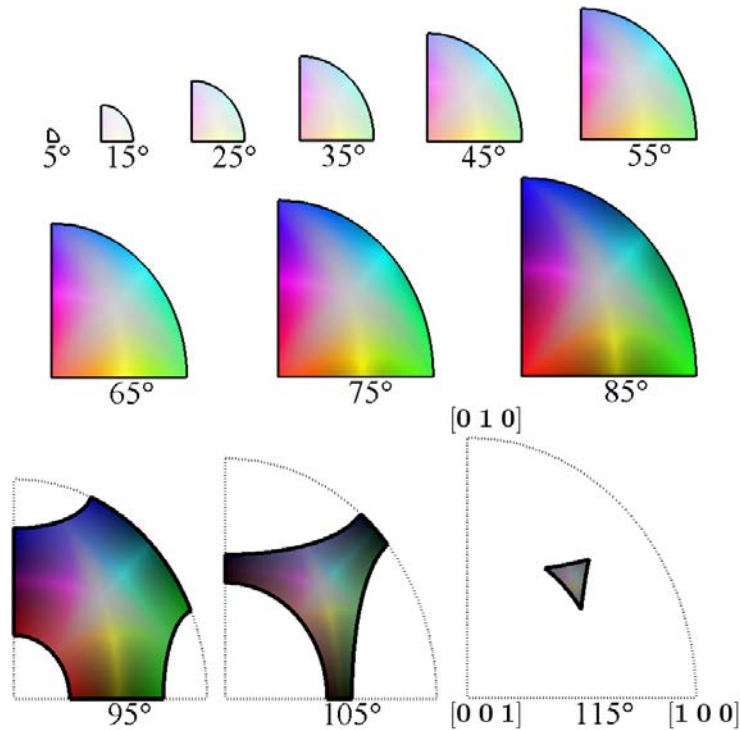
Figure 3.3 Color legend for grain boundary misorientations of crystals with $D_2(222)$ rotational point group symmetry. Each triangle is the well-known standard stereographic triangle for 222 point group.

63
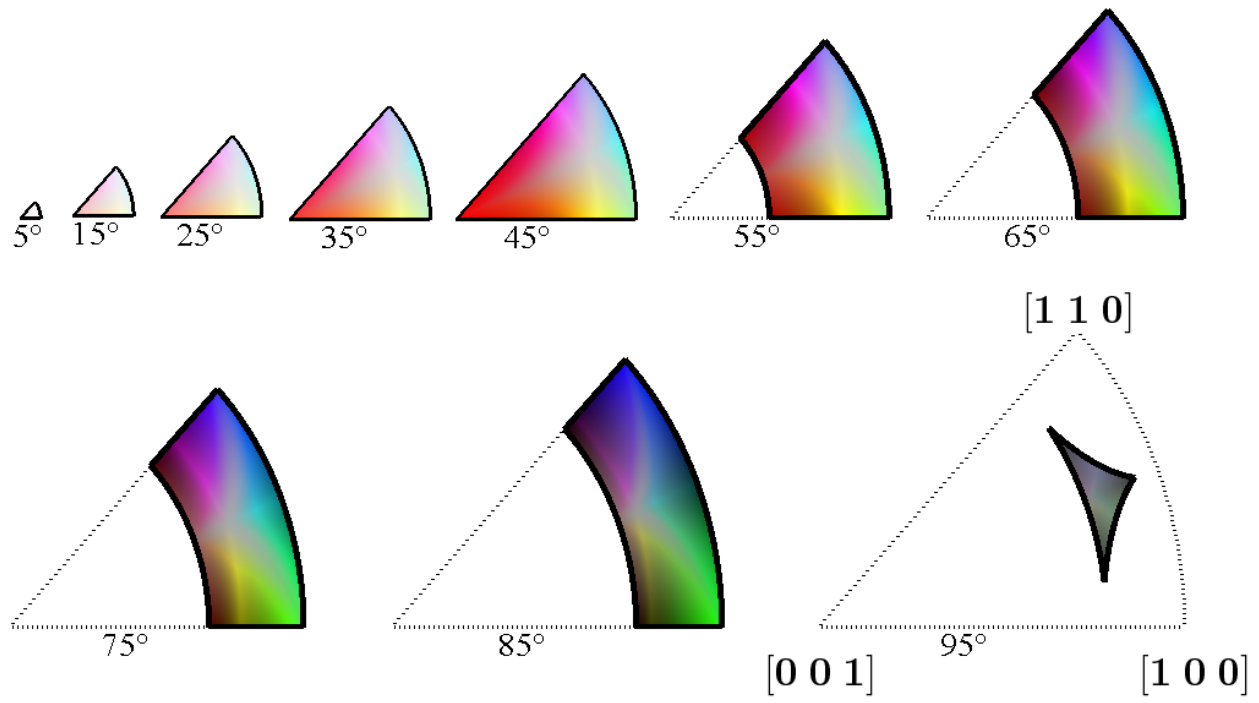
Figure 3.4 Color legend for grain boundary misorientations of crystals with $D_4(422)$ rotational point group symmetry.
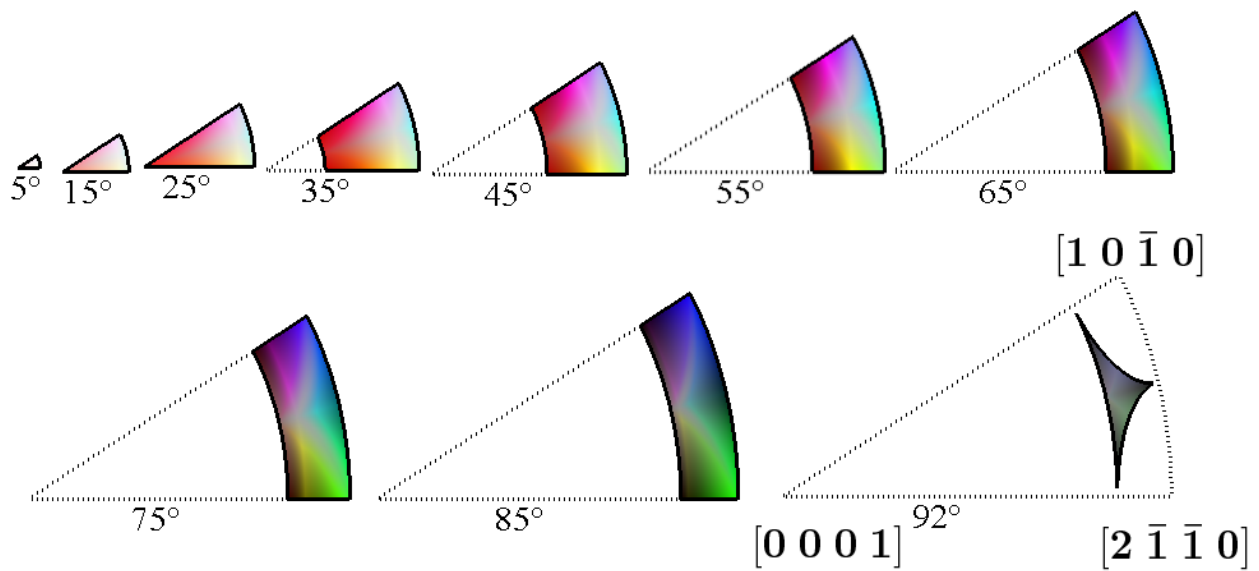
Figure 3.5 Color legend for grain boundary misorientations of crystals with $D_6(622)$ rotational point group symmetry.
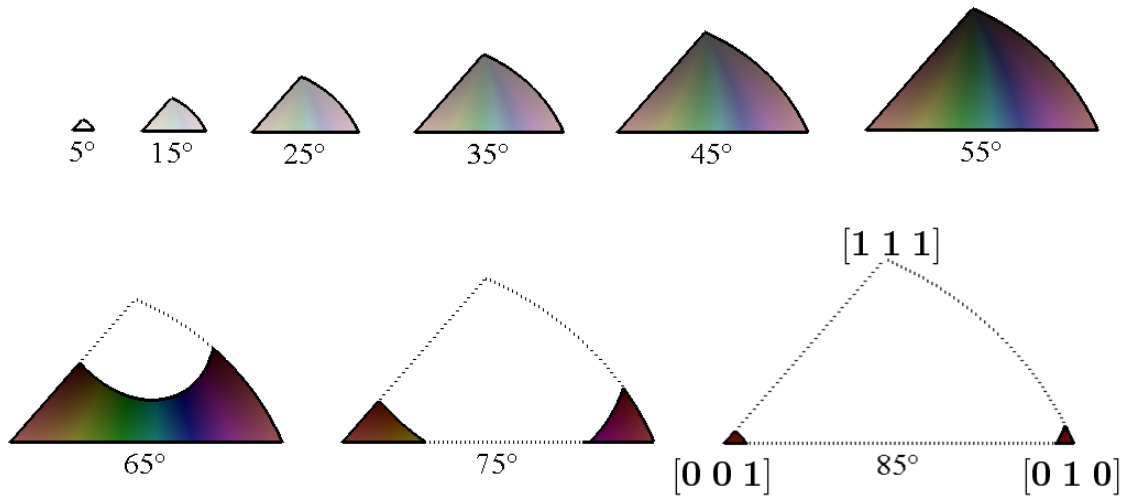
Figure 3.6 Color legend for grain boundary misorientations of crystals with $T(23)$ rotational point group symmetry.
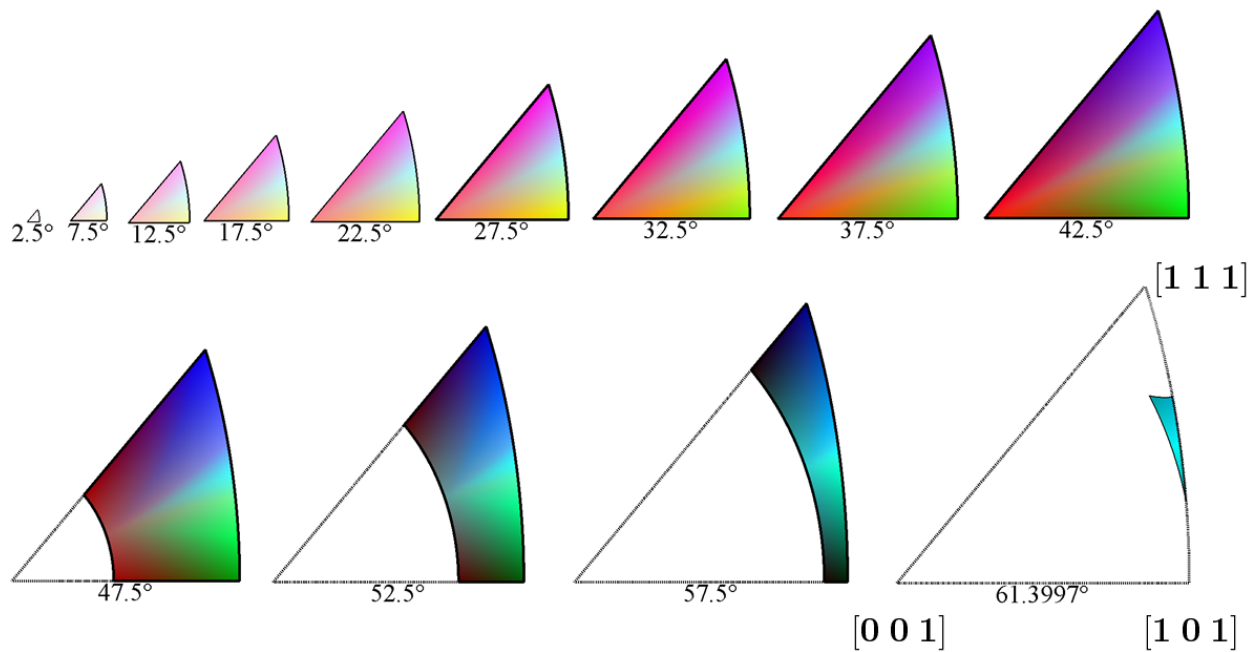
Figure 3.7 Color legend for grain boundary misorientations of crystals with $O(432)$ rotational point group symmetry, built using area-preserving projection of surfaces of constant misorientation angle ω. Each triangle is the well-known standard stereographic triangle.

3.3. Grain Boundary Misorientation Maps

With the legends shown in Figures 3.3, 3.4, 3.5, 3.6 and 3.7, we may now create grain boundary misorientation maps that contain complete misorientation information. Examples of such maps are shown in Figures 3.8 and 3.9, for the same sets of EBSD data already presented in Figure 1.3. The misorientation information can be directly inferred from the legend by matching the boundary color, reading the misorientation angle from the standard stereographic triangle in which it falls, and the misorientation axis from its position in the triangle. Comparing Figures 3.8 and 3.9 to either of the two representations in Figure 1.3 reveals the qualitative power of the new mapping; whereas Figure 1.3 bins misorientations into classes and neglects most of the misorientation information, the grain boundary misorientation maps involve no loss of information and cover the entire misorientation spectrum. The discovery of a continuous mapping of colors to misorientations also guarantees that boundaries of similar misorientation are colored similarly, and vice versa.
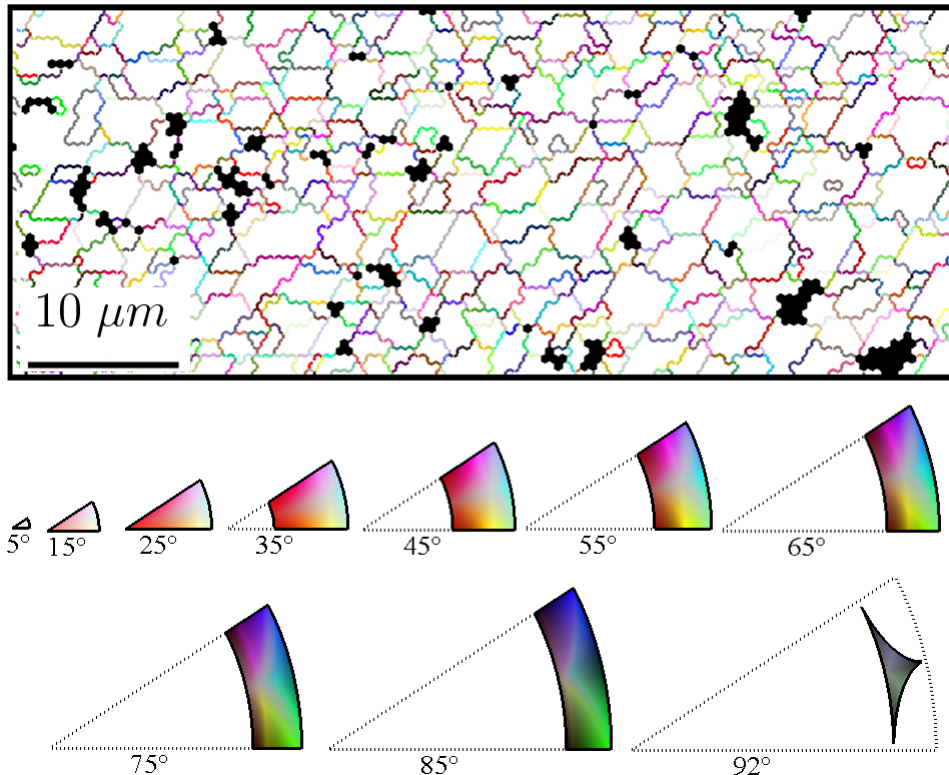
Figure 3.8 Grain boundary misorientation map for a hexagonal closed packed material, Rhenium. The rotational point group of Rhenium is $D_6(622)$. Complete misorientation information (axis and angle) can be directly interpreted using the legend. Since the colors represent a continuous mapping, contrast in the colors represents misorientation distance.
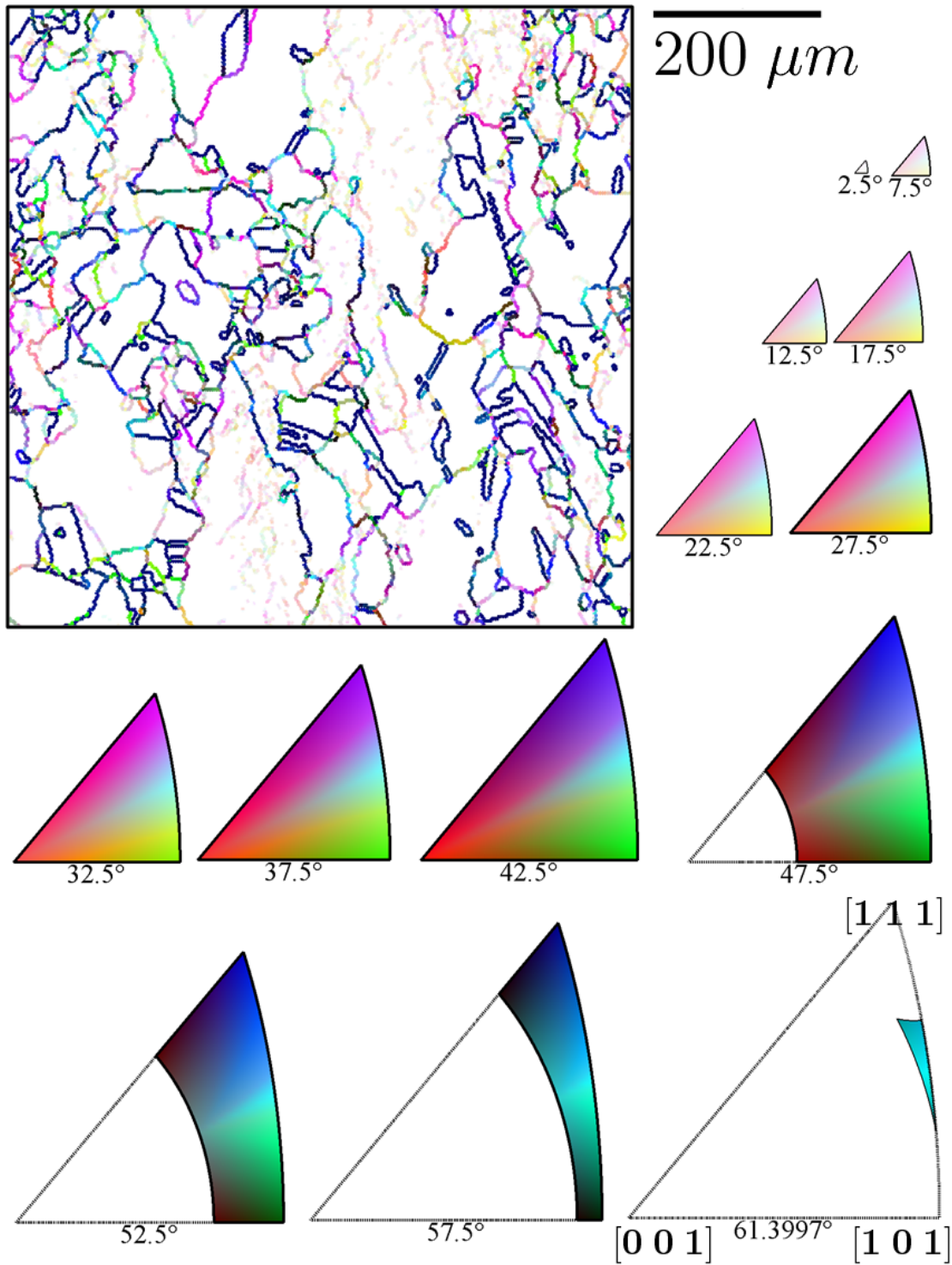
Figure 3.9 Grain boundary misorientation map for the Cu-Cr sample with a coloring scheme that is one-to-one and continuous.

3.4. Improved Representation of Orientation Maps

The mappings of misorientation spaces to $\mathbb{R}^3$ also have implications beyond the problem of coloring grain boundary maps. For example, the mapping of misorientations to three-dimensional Euclidean space can be used to develop better coloring schemes for the orientations of individual grains. Orientations lack much of the symmetry of misorientations, and occupy a larger space. As noted in section 2.3.2, the orientation spaces are not simply connected in three dimensions, so it is not formally possible to color orientations in a continuous and one-to-one manner. However, we may capture most of the orientation information using an approximation: grain orientations can be considered as misorientations with respect to a fixed reference frame. For example, given a grain orientation lying in the 432-orientation fundamental zone, additional crystal symmetries and the grain inversion symmetry can be applied to find its equivalent parameters in the misorientation fundamental zone and thus a color can be attributed. The caveat is that there are 48 distinct orientations that will be mapped to the same misorientation and hence will have the same color.

(a)   (b)
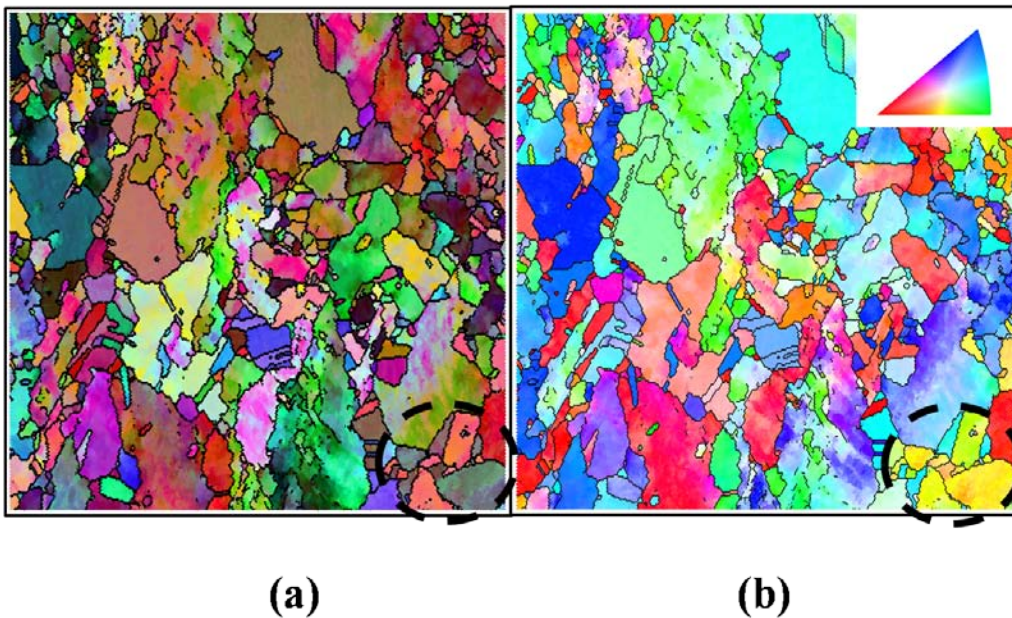
Figure 3.10 Representations of EBSD data using colors to denote grain orientations. (a) Grain orientations colored according to their misorientations with respect to the sample reference frame, using the legend from Figure 3.7. (b) Grain orientations colored using traditional inverse pole figure representation, with the legend in the upper-right corner showing the mapping of color to surface normal vector. The grains in the dashed circle are used to show the advantages of this approximate coloring scheme using misorientations as compared to the inverse pole figure representation.

We apply this method to the coloring of grain orientations in Figure 3.10(a), which is the same set of EBSD data for Cu-Cr used in Figure 1.3. We choose a reference orientation aligned with the sample axes, and plot the grain color as the disorientation with respect to this reference frame. For comparison, shown in Figure 3.10(b) are grain orientation maps using a more traditional inverse pole figure representation, with the legend shown in the inset. Whereas the map in Figure 3.10(b) only contains information about the crystallographic vector normal to the viewing plane, the coloring scheme in Figure 3.10(a) captures far more information over the misorientation space. For example, consider the grains circled in the lower right hand corner of this figure. Whereas the grains are colored in a very similar shade of yellow in (b), they abut a grain boundary and are actually oriented very differently; they are misoriented by a rotation in the plane that is not captured by examination of the surface normal vector alone. In contrast, this orientation difference is captured by the coloring scheme of (a), which, by comparison to the grain boundary map in Figure 3.9, reveals a large misorientation of 60º.

3.5. Industrial Collaboration: Incorporation in OIM^{TM} Analysis Software

Since most engineering materials belong to one of the five rotational point group symmetries, the utility of the novel grain boundary misorientation maps is very high. The coloring schemes do not discard any of the misorientation information during graphical representation and hence, these maps are of great value to the materials science community, which can recover all of the original data. This has been a significant motivating factor for us to collaborate with the industry in an effort to make the representation schemes practical and readily available. It is now possible for anybody in the field to use our newly developed coloring schemes, without the need of understanding the abstract topological details.

The complete potential of the novel grain boundary misorientation maps may be realized only through increasing familiarity with the coloring schemes among the materials science community. The coloring schemes have been incorporated into the OIM^{TM} Analysis Software during an internship lasting a week at the EDAX-TSL company (original developers of Orientation Imaging Microscopy) in Salt Lake City, Utah. Shown in Figure 3.11 is a screenshot of the GUI interface of the OIM^{TM} Analysis Software with the new coloring scheme.
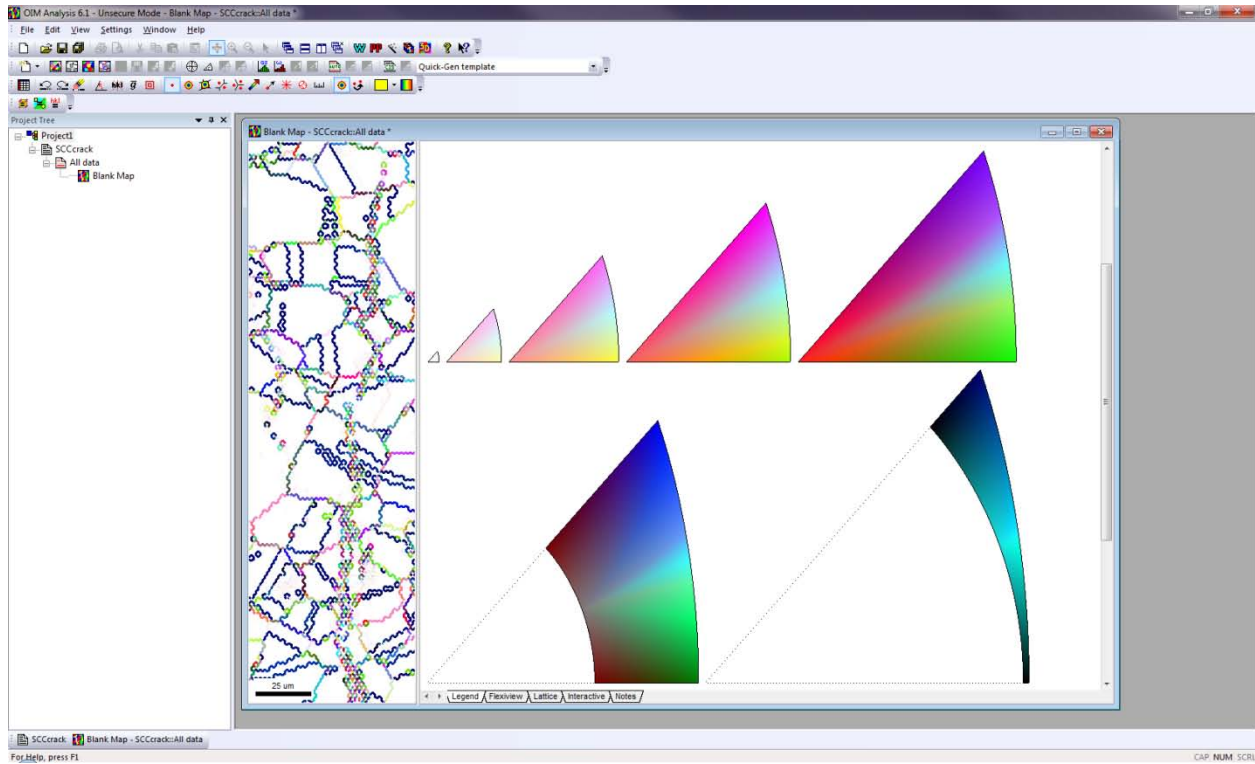
Figure 3.11 A screen-shot of the OIM^{TM} Analysis Software with the grain boundary misorientation map built using coloring schemes developed in this thesis.

3.6. Conclusions

The embeddings of the grain boundary misorientation spaces in $\mathbb{R}^3$ have immediate practical application in the representation of misorientation data from, e.g., electron backscatter diffraction, as it permits mapping of misorientations to colors with no loss of information. We have demonstrated the coloring of a grain boundary network in samples of copper and rhenium alloys as a proof of this concept. If a reference orientation is defined, the method also permits coloration of grain orientations in a new way that captures information lost in conventional "inverse pole figure" mapping common in the field.

The embedding of misorientation space in $\mathbb{R}^3$ also opens the door to more nuanced views of how misorientations are related to one another: whereas the 'distance' between two misorientations is complicated by discontinuous jumps in the misorientation space, when embedded in $\mathbb{R}^3$ the removal of discontinuities permits simple Euclidean distance calculations. The simplification of misorientations through this mapping is also a useful first step towards the development of a system for understanding the full five-parameter space of grain boundaries that

70

includes the plane normal vectors, the topology of which is presently unknown. Finally, we note that although here we have used a simple two-dimensional example to illustrate the coloring of grain boundary misorientations, the technique should naturally apply to more sophisticated three-dimensional datasets and computer simulations.

4. Topology of the Single-Axis Grain Boundary Space

4.1. Introduction

In the preceding chapters, we investigated the topology of the grain boundary misorientation spaces and developed new visualization tools for better interpretation of misorientation information. These coloring schemes are useful in representing complete misorientation information and also in elucidating the topological aspects of the grain boundary misorientation spaces. However, misorientation does not completely characterize a grain boundary and the structure of grain boundaries is determined by two macroscopic degrees of freedom: the boundary misorientation (M) and the boundary inclination $(\vec{n})$. The boundary normal vectors require two independent variables and along with the misorientation, the grain boundary parameters are uniquely specified by five independent variables. Despite current experimental capabilities that allow a complete crystallographic characterization of grain boundaries, our theoretical understanding of the grain boundary space (defined in section 1.1) remains limited.

The topology of the grain boundary space is complicated mainly due to the equivalence relations, mentioned in section 1.1.5, on this space. The equivalence relations relevant to crystallographic point groups with only rotational symmetry elements are reiterated below:

(a) $(M; \vec{n}) \sim \left(\left(S^i\right)^{-1} M\left(S^j\right);\ \mathbf{g}\left(\left(S^i\right)^{-1}\right) * \vec{n} \right)$

(b) $(M; \vec{n}) \sim \left(M^{-1}; \mathbf{g}(M^{-1}) * (-\vec{n}) \right)$ $\hspace{3cm}$ (4.1)

(c) $(I; \vec{n}) \sim \left(I, \overrightarrow{n'} \right) \hspace{1cm} \forall\ \vec{n}, \overrightarrow{n'} \in S^2$

The difficulty in understanding the topological characteristics of the complete grain boundary space arises mainly due to the equivalences imposed by the 'no-boundary' condition, which results in a cone-type singularity [95] in the space. It requires collapsing all the boundary inclinations that correspond to the zero-misorientation boundary. In this chapter, we present developments that provide insights into the role of the relations in Equation (4.1) on the topology of the complete grain boundary space.

First, we focus on the topology of the grain boundary space of two-dimensional (2D) crystal systems. The case of 2D boundaries has all the critical features of the full three-dimensional (3D) problem and permits visualization of the results in a far more transparent manner, and provides a useful first step towards understanding the full 3D problem. Although the space of grain boundaries is complicated by the existence of a 'no-boundary' singularity, we show that when the grain exchange symmetry is applied to the grain boundary space in two-dimensional systems, the complication due to the 'no-boundary' singularity is removed. As mentioned in section 1.1.6, we confine our analysis to the crystallographic point groups with only proper rotational symmetries.

4.2. Topology of the Grain Boundary Space for 2D Crystal Systems

In this section we investigate the topology of grain boundary of two-dimensional systems, i.e., the space of the parameters describing the 1D linear boundaries between 2D crystals. We start with visualizing the 2D grain boundary space without any equivalence relations associated with the space. The 2D grain boundary parameters are represented using the angles (ω, β), where ω describes the misorientation angle and β is the angle made by the normal vector with the crystallographic x-axis. Shown below in Figure 4.1 is a schematic illustrating a 2D grain boundary with boundary parameters $(\omega, \beta) = (\pi/6, 5\pi/6)$.
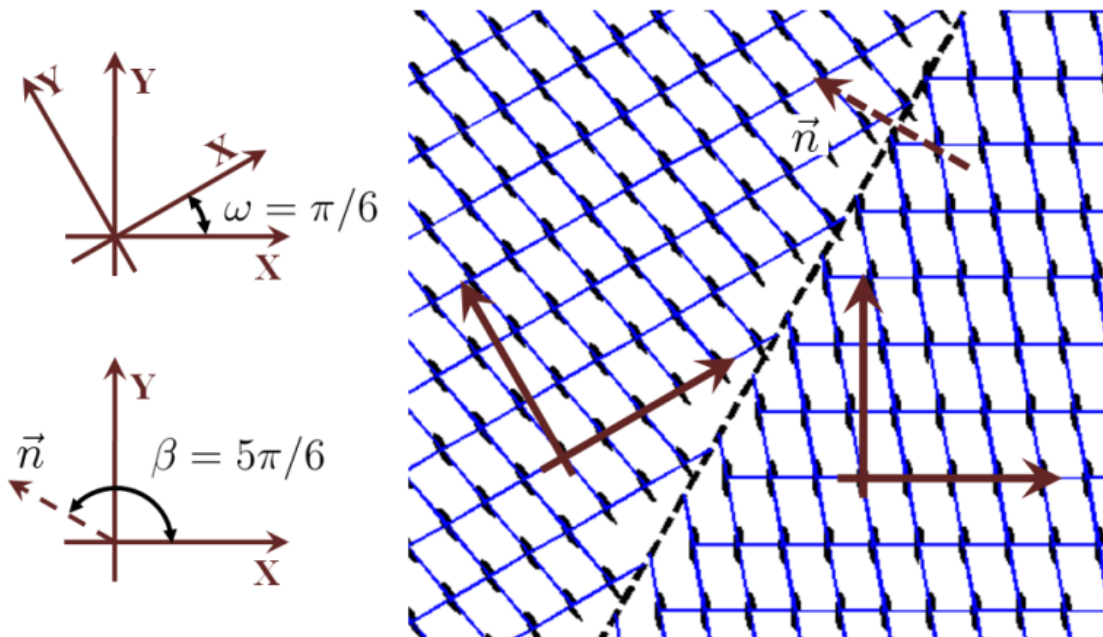
Figure 4.1 Schematic illustrating the grain boundary parameters (ω, β) of a 2D grain boundary.

The misorientation space for 2D grain boundaries defined by $\omega \in [0,2\pi)$ is equivalent to a circle (S^1) with additional symmetries from the underlying crystals. The boundary inclinations for 2D boundaries are defined by the collection of unit vectors in the plane, which belongs to the points on a circle (S^1). Since the misorientations and inclinations of a boundary are independent of each other, the 2D grain boundary parameters belong to the product space $S^1 \times S^1$ (which is a torus) as illustrated in Figure 4.2.
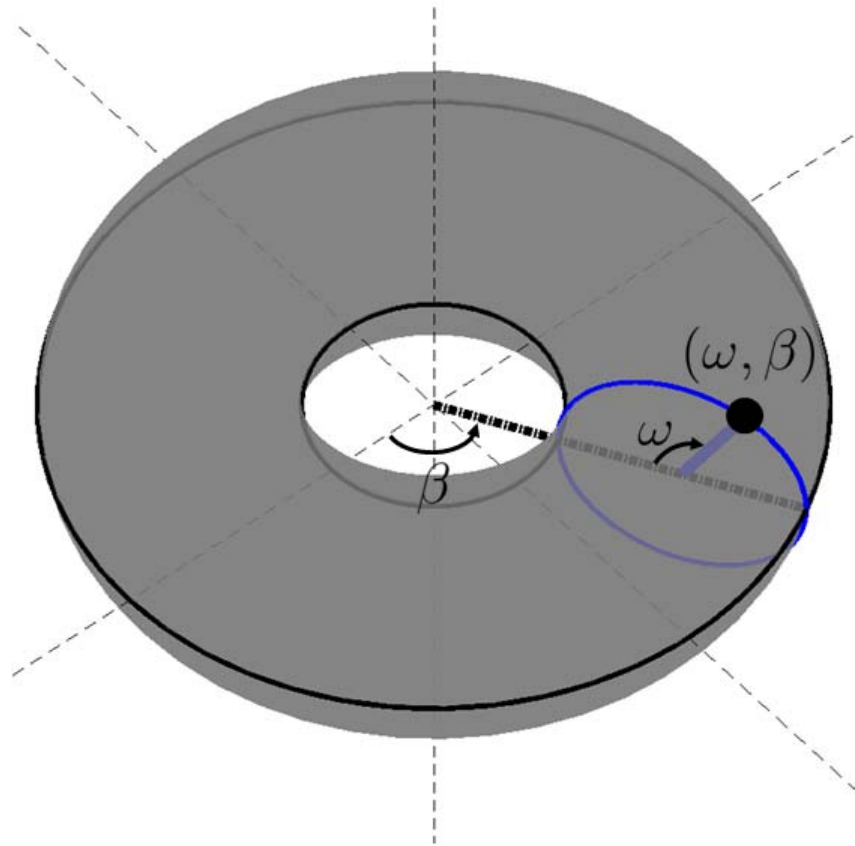
Figure 4.2 The torus represents the product space $S^1 \times S^1$. Any point on the torus can be defined using (ω, β) parameters. Here ω represents the boundary misorientation and β represents the boundary inclination and $\omega, \beta \in [0, 2\pi)$.

4.2.1. Two-dimensional Grain Boundary Space

The grain boundary space is the quotient space of the torus with the equivalence relations in Equation (4.1) applied. These equivalence relations expressed in terms of (ω, β) take the form:

(a) $(\omega, \beta) \sim \left(\omega - \frac{2\pi i}{n} + \frac{2\pi j}{m}, \beta - \frac{2\pi i}{n} \right); i, j \in \{1, \dots, n\}$

(b) $(\omega, \beta) \sim (2\pi - \omega, \pi - \omega + \beta)$ (4.2)

(c) $(0, \beta) \sim (0, \beta')$

where n is the order of the rotational point group of the crystal system under consideration. The no-boundary equivalence requires collapsing the $\{\omega = 0\} \times S^1$ region in the torus to a single point, which can be achieved by shrinking the inner radius of the torus to zero; see the difference between Figures 4.2(a) and 4.2(b). The torus so obtained in Figure 4.2(b) is called a 'horned torus', which is equivalent to a 2-sphere with two antipodal points (the north and south poles) identified. The horned torus is mapped to a 2-sphere by expressing the polar coordinates of the 2-sphere in terms of the boundary parameters as $(\theta, \phi) = (\omega/2, \beta)$, which applies for the grain boundaries of crystals with C_1 point symmetry. In the case of boundaries of crystals with C_n point group symmetry, the polar coordinates are related to the boundary parameters by the relation:

$$(\theta, \phi) = \left(\frac{n\omega}{2}, n\beta \right)$$ (4.3)

where ω and β are restricted to $[0, 2\pi/n]$. This ensures that θ is confined to $[0, \pi]$ and ϕ is confined to $[0, 2\pi]$. In the domain $\omega, \beta \in [0, 2\pi/n]$, the equivalence relations due to crystal symmetries (Equation (4.2)(a)) need not be considered, which simplifies the subsequent analysis.

In polar coordinates, the no-boundary equivalence relation takes the form $(0, \phi) \sim (\pi, \phi)$. This equivalence implies that the two poles, $(0,0,1)$ and $(0,0,-1)$ are identified. Even though the measure and metrics on a 2-sphere are familiar, the identification of the two poles makes the topology more complicated, and hence there is no immediately obvious method to define metrics. This singularity is a result of the 'no-boundary' condition at zero misorientation.
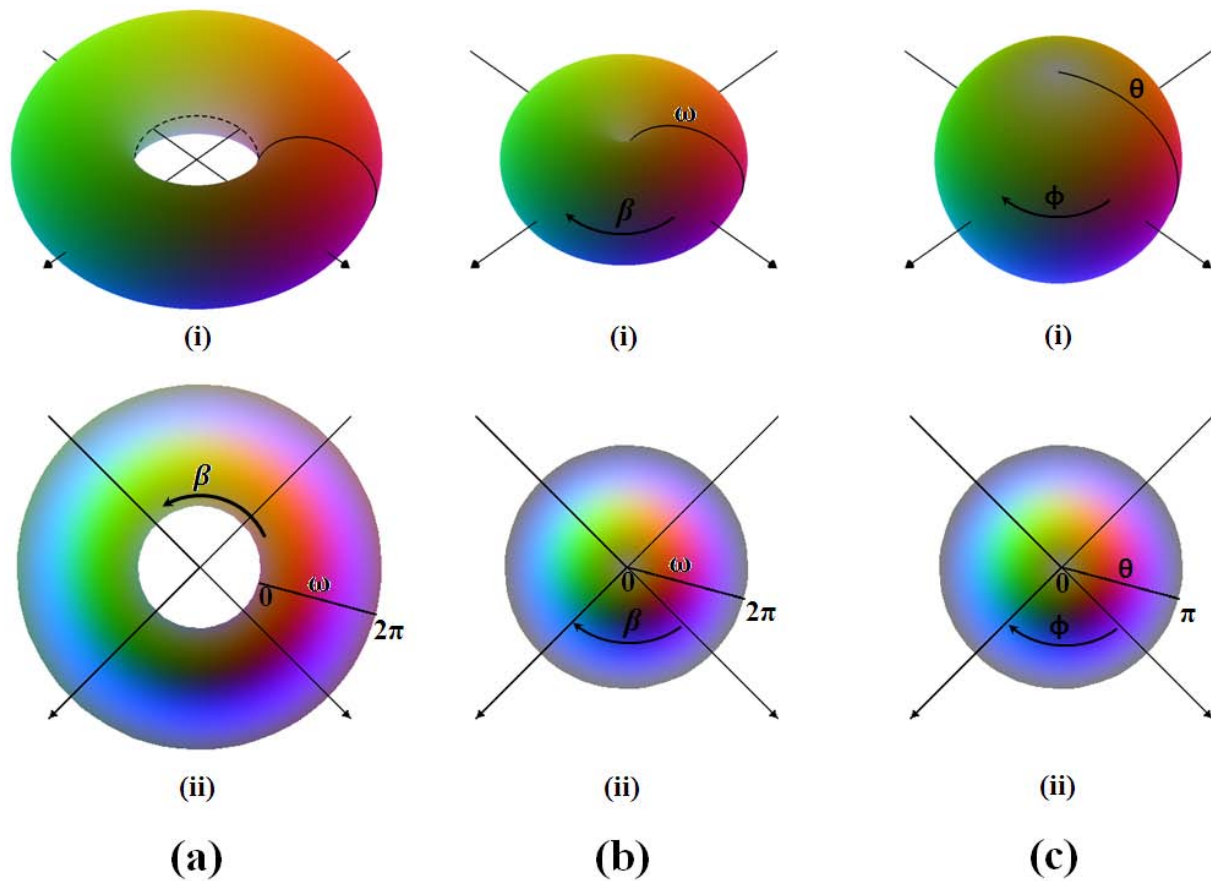
Figure 4.3 Colors are used to represents the connectivity of these spaces. (a) (i) $S^1 \times S^1$ torus and its (ii) projection onto a plane. (b) (i) The horned-tours (inner radius = 0) and its (ii) projection. As represented by the coloring scheme, the points $(\omega = 0, \beta)$ and $(\omega = 2\pi, \beta)$ are equivalent. (c) The horned-tours is mapped into a 2-sphere using the relation $(\theta, \phi) = (\omega/2, \beta)$.

We find, however, that this singularity can be resolved by invoking grain exchange symmetry. Applying the equivalence relation from Equation (4.1)(b) to the polar coordinates of the 2-sphere results in the following equivalence relation:

$$\left(\frac{2\theta}{n}, \frac{\phi}{n}\right) \sim \left(\frac{2\pi}{n} - \frac{2\theta}{n}, \pi - \frac{2\theta}{n} + \frac{\phi}{n}\right) \tag{4.4}$$

$$\Rightarrow \left(\theta, \frac{\phi}{n}\right) \sim \left(\pi - \theta, \frac{(\pi - 2\theta)}{n} + \frac{\phi}{n} + \frac{(n-1)\pi}{n}\right)$$

$$\Rightarrow (\theta, \phi) \sim (\pi - \theta, (\pi - 2\theta) + \phi + (n-1)\pi)$$

This is a complicated relation since the equivalence in the ϕ coordinate is dependent on θ. This complication can be removed by using modified parameters (θ', ϕ')

$$(\theta', \phi') = \left(\theta, \phi - \frac{(\pi - 2\theta)}{2}\right) \tag{4.5}$$

which yields the following equivalence relation:

$$\left(\theta', \phi' + \frac{(\pi - 2\theta)}{2}\right) \sim \left(\pi - \theta', \phi' + \frac{(\pi - 2\theta)}{2} + (n-1)\pi\right) \tag{4.6}$$

$$\Rightarrow (\theta', \phi') \sim (\pi - \theta', \phi' + (n-1)\pi)$$

Two situations arise when the boundary parameters are expressed in terms of (θ', ϕ'). First, if n is odd, then the equivalence relation shown in Equation (4.6) is equivalent to $(\theta', \phi') \sim (\pi - \theta', \phi')$ (since $n - 1$ is even and a multiple of 2π). Second, if n is even, then the equivalence relation is simplified to $(\theta', \phi') \sim (\pi - \theta', \phi' + \pi)$ (since $n - 1$ is an odd number). The advantage of using the modified parameters in representing the boundary information is illustrated in Figure 4.4 and Figure 4.5 for odd- and even-fold rotational symmetry systems respectively. Using the modified parameters results in simple equivalence relations corresponding to either a mirror symmetry or an inversion symmetry on the 2-sphere.
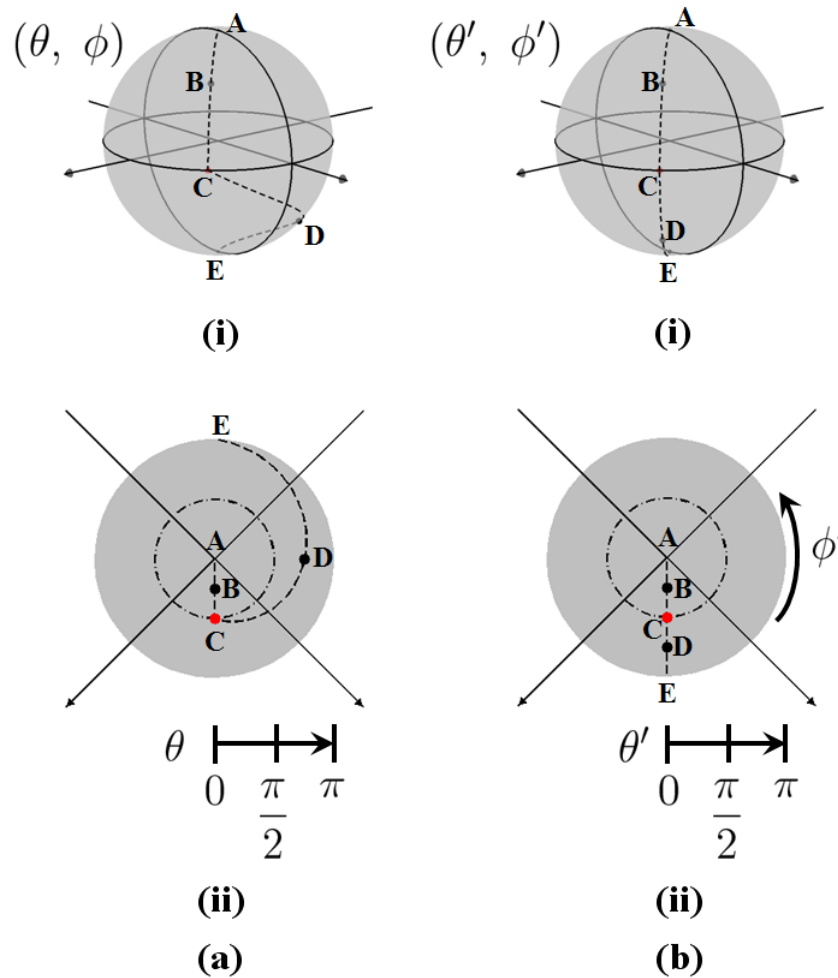
Figure 4.4 The equivalence relations corresponding to Equations (4.4) and (4.6) for odd-fold rotational symmetry systems (a) Grain boundary information using (θ, ϕ) parameters. The path ABC in the upper hemisphere is equivalent to the path CDE in the lower hemisphere. This equivalence is better represented in its (ii) projection. (b) Boundary information using (θ', ϕ') parameters. In this parameterization the paths ABC and CDE are related through mirror symmetry.
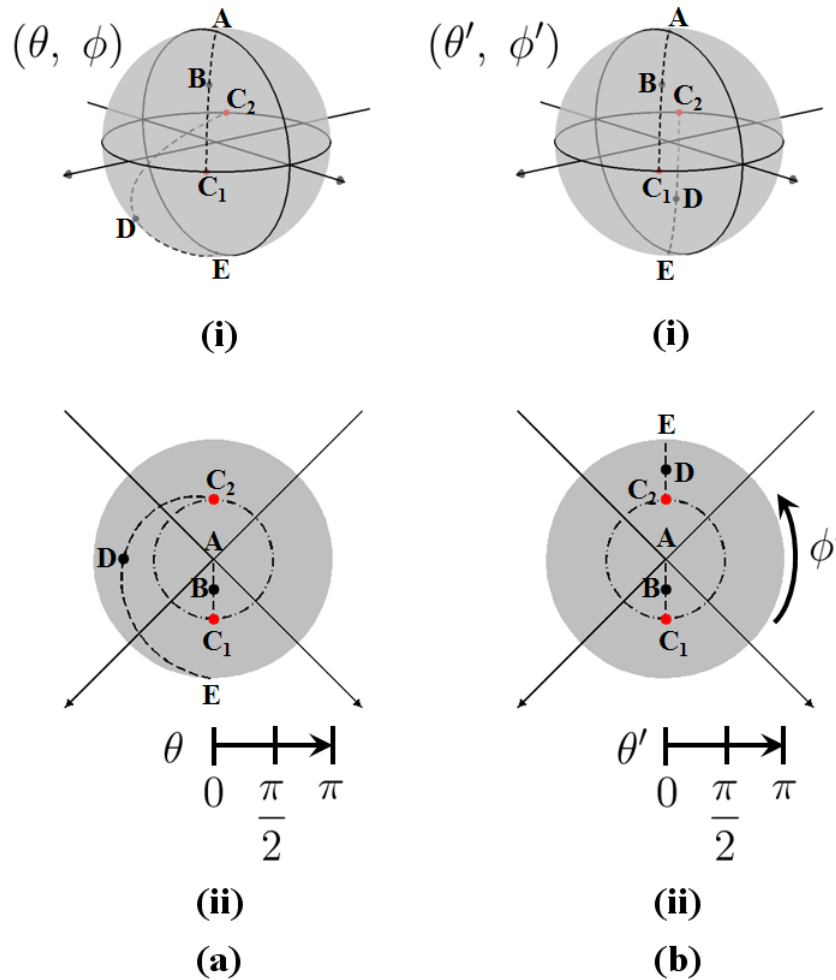
Figure 4.5 The equivalence relations corresponding to Equations (4.4) and (4.6) for even-fold rotational symmetry systems (a) Grain boundary information using (θ, ϕ) parameters. The path ABC_1 in the upper hemisphere is equivalent to the path C_2DE in the lower hemisphere. This equivalence is better represented in its (ii) projection. (b) Grain Boundary information using (θ', ϕ') parameters. In this parameterization the paths ABC_1 and C_2DE and are related by an inversion about the origin. The space is defined as the real projective plane $(\mathbb{R}P^2)$.

To summarize, modified parameters (θ', ϕ') are used to represent the grain boundary parameters. They are related to (ω, β) by the following equation:

$$(\theta', \phi') = \left(\frac{n\omega}{2}, n\beta - \frac{(\pi - n\omega)}{2}\right) \tag{4.7}$$

where ω and β are restricted to $[0, 2\pi/n]$ and n corresponds to the point group C_n of the crystal. Any boundary with parameters $\omega > 2\pi/n$ or $\beta > 2\pi/n$ has a symmetrically equivalent description in the restricted domain, which is obtained by applying appropriate crystal symmetries. Examining the above results, we observe that the grain boundary spaces of the C_1 and C_3 systems are topologically equivalent to that of a disc in the two-dimensional Euclidean plane. This is a result of the equivalence relation $(\theta', \phi') \sim (\pi - \theta', \phi')$. This relation expressed in terms of Cartesian coordinates is of the form $(x, y, z) \sim (x, y, -z)$. Hence the topology of the grain boundary space for these systems is the quotient space of the 2-sphere with the equivalence relation $(x, y, z) \sim (x, y, -z)$. This quotient space is equivalent to a disc (D^2) in two-dimensional Euclidean plane. The space is simply connected (admits a trivial fundamental group) and can be embedded in $\mathbb{R}^2$.

In the case of the C_2, C_4 and C_6 systems (see Figure 4.5) the grain boundary space is equivalent to the real projective plane ($\mathbb{R}P^2$). The equivalence relation $(\theta', \phi') \sim (\pi - \theta', \phi' + \pi)$ expressed in terms of Cartesian coordinates is of the form $(x, y, z) \sim (-x, -y, -z)$, i.e. a 2-sphere with all antipodal points identified, or the real projective plane. The topological properties of $\mathbb{R}P^2$ are well documented. The minimum number of Euclidean dimensions in which it can be embedded is four [92]. It has a non-trivial fundamental group $\mathbb{Z}_2$ [76].

The parameterization in Equation (4.5) has several immediate practical consequences. For example, the metrics on a 2-sphere can be used to express the "distance" between grain boundaries. This helps achieve meaningful answers to the question of how similar two boundaries are if they have different misorientations and boundary planes. The distance between two points denoted by (θ_1', ϕ_1') and (θ_2', ϕ_2') on a sphere is given by:

$$s = \arccos(\cos\theta_1' \cos\theta_2' + \sin\theta_1' \sin\theta_2' \cos(\phi_1' - \phi_2')) \; where \; s \in [0, \pi] \tag{4.8}$$

81

The distance between two boundaries (ω_1, β_1) and (ω_2, β_2) is obtained in three steps:

(i) The evaluation of symmetrically equivalent descriptions of (ω_1, β_1) and (ω_2, β_2) that lie in the domain $[0, 2\pi/n]$.

(ii) Evaluation of symmetrically equivalent descriptions of boundary parameters in the (θ', ϕ') parameterization using Equation (4.5).

(iii) The distance between the two boundaries is finally obtained by taking the minimum of the distances between the equivalent representations calculated using Equation (4.8).

Since the modified grain boundary parameters (θ', ϕ') reside on the surface of a unit-sphere, functions describing distributions of these parameters can be expanded as a linear combination of the Laplace spherical harmonics Y_l^m [96] which form a complete set of orthonormal functions. Any square-integrable function can be expressed as a linear combination of the spherical harmonics as:

$$f(\theta', \phi') = \sum_{l=0}^{\infty} \sum_{m=-l}^{l} C_l^m Y_l^m(\theta', \phi') \tag{4.9}$$

It is necessary that the function f inherit the symmetries of the boundary space. This is achieved by using symmetrized spherical harmonics which are commonly used in pole distributions in representing texture [97]. Symmetrized spherical harmonics must reflect the mirror symmetry in the case of C_1 and C_3 boundary systems and the inversion symmetry in the case of C_2, C_4 and C_6 boundary systems.

There are two crucial steps involved in resolving the topology of 2D grain boundaries: (a) the inner-radius of the torus is collapsed to a single point to account for the 'no-boundary' singularity and (b) the grain exchange symmetry is simplified using the modified parameters (θ', ϕ') introduced in Equation (4.5). In the following section, we develop a new parameterization for the grain boundary space of three-dimensional crystal systems, which is specifically aimed at accomplishing these two particular tasks.

4.3. New Parameterization for the Complete Grain Boundary Space

The parameterizations for the two aspects of boundary parameters, i.e. the rotations (rotation matrices, Euler angles, axis-angle parameters, quaternions etc.) and the boundary normal vectors (either Cartesian or polar coordinates), are well-defined. Hence, the parameterization for the complete grain boundary space involving these quantities is mainly concerned with combining the two quantities in a convenient way that helps simplify the equivalence relations on the grain boundary space. We first review the two relevant methods of parameterizing the complete grain boundary space; both were proposed by Morawiec [77].

Interface Matrix: The interface matrix combines the misorientation and boundary normal vector parameters of a grain boundary so that the resulting matrix can be used to express the grain exchange symmetry in a convenient way. The interface matrix $\mathbf{B}_{AB}$, describing the boundary with respect to grain A is given as:

$$\mathbf{B}_{AB} = \begin{bmatrix} 0 & (\vec{n}_{BA})^T \\ \vec{n}_{AB} & \mathbf{g}(M_{AB}) \end{bmatrix} \tag{4.10}$$

And the interface matrix with respect to grain B is given by $\mathbf{B}_{BA} = \mathbf{B}_{AB}^T$. Because the interface matrix uses 15 parameters to describe a boundary, it is not useful for analyzing the topological properties of the grain boundary space.

Symmetric Parameterization: Morawiec also proposed a symmetric way of parameterizing grain boundaries. Given boundary parameters $(M, \vec{n})$, a rotation matrix N is defined, which corresponds to the same rotation axis as M, but where the rotation angle is half of that for M, such that $N * N = M$. This definition is well-defined for rotation angles less than π. If M corresponds to a rotation of π, there exist two equivalent descriptions $(\pi, \vec{a})$ and $(\pi, -\vec{a})$ in axis-angle parameters. Hence a convention is assumed for selection of the axis if M corresponds to a rotation of π. The normal vector is defined as $\vec{r} = N^{-1} * (\vec{n})$. The advantage of this representation of grain boundaries is that the grain exchange symmetry is considerably simplified, and is expressed as:

$$(N; \vec{r}) \sim (N^{-1}; -\vec{r}) \tag{4.11}$$

Even though this parameterization is convenient for representing boundary parameters, it has some significant flaws that render it ineffective. First, it is important to note that neither the interface matrix nor the symmetric parameterization account for the 'no-boundary' singularity, since different boundary inclinations linked to $M = I$ give distinct representations. Second, no matter what convention is used to select the rotation axis for misorientations of angle π, there is a discontinuity in the mapping from $(M; \vec{n})$ to $(N; \vec{r})$ (refer to **Appendix B**). Hence the grain boundary space $\mathcal{B}$ is not equivalent to the space represented using the parameters $(N; \vec{r})$.

It is possible to remedy these problems by utilizing the quaternion parameterization of the rotation space. In order to obtain a rigorous and topologically consistent mapping from the grain boundary space to the symmetric representation, the two copies of the rotation space, i.e. the complete 3-sphere with antipodal identifications needs to be taken into consideration. We also show that the 'no-boundary singularity' is essential for a topologically consistent definition of the symmetric representation.

4.3.1. Topologically Consistent Parameters for the Grain Boundary Space

Using the quaternion parameterization, i.e. $\mathcal{B} = (\mathbf{q}; \vec{n})$, the grain boundary space is equivalent to $S^3 \times S^2 / E$, where the set of equivalence relations E include:

(a) $(\mathbf{q}; \vec{n}) \sim (-\mathbf{q}; \vec{n})$

(b) $(\mathbf{q}; \vec{n}) \sim \left(\left(S^i \right)^{-1} \mathbf{q} (S^j); \mathbf{g} \left(\left(S^i \right)^{-1} \right) * \vec{n} \right)$

(c) $(\mathbf{q}; \vec{n}) \sim \left(\mathbf{q}^{-1}; \mathbf{g}(\mathbf{q}^{-1}) * (-\vec{n}) \right)$

(d) $\left((1,0,0,0); \vec{n} \right) \sim \left((1,0,0,0); \vec{n'} \right)$

$$(4.12)$$

So far, we have only used the fact that the rotation space $SO(3)$ is homeomorphic to the 3-sphere S^3 with antipodal points identified. The equivalence relation in Equation (4.12)(a) is this antipodal symmetry which is also referred to as the trivial symmetry of the rotation space. The relations Equation (4.12)(b), (c) and (d) are obtained by expressing Equation (4.1) in the quaternion parameterization.

Since the symmetric parameterization is related to the axis-angle parameters of the misorientation, it will be useful to define the function that relates the axis-angle parameters to the quaternion space as $A: [0,2\pi] \times S^2 \rightarrow S^3$:

$$A(\omega, \vec{a}) = \left(\cos\left(\frac{\omega}{2}\right), a_x \sin\left(\frac{\omega}{2}\right), a_y \sin\left(\frac{\omega}{2}\right), a_z \sin\left(\frac{\omega}{2}\right) \right) \tag{4.13}$$

The domain of the function A is $[0,2\pi] \times S^2$, since we let $\omega \in [0,2\pi]$ and the axis $\vec{a} \in S^2$. It is important to note that A is not an injective map since $A(0, \vec{a}) = (1,0,0,0)$ and $A(2\pi, \vec{a}) = (-1,0,0,0)$ for any $\vec{a} \in S^2$. But if $\omega \neq \{0,2\pi\}$, the mapping A is injective. Now, we define the mapping $P: (\mathbf{q}; \vec{n}) \rightarrow (\mathbf{q}; \vec{r})$, where $(\mathbf{q}; \vec{r})$ is the new desired parameterization.

$$(\mathbf{q}; \vec{r}) = P(\mathbf{q}; \vec{n}) = \begin{cases} \left(\mathbf{q}; \mathbf{g}(p(\mathbf{q})) * [C(\mathbf{q})(\vec{n})] \right) & if \; q_0 \neq -1 \\ \left((-1,0,0,0); \vec{0} \right) & if \; q_0 = -1 \end{cases} \tag{4.14}$$

The scalar function $C(\mathbf{q})$ is defined as:

$$C(\mathbf{q}) = \sqrt{1 - \max\{((\mathbf{q} * \mathbf{G})_0)^2\}} \tag{4.15}$$

where $\mathbf{G}$ is the rotational point group of the crystal, $\mathbf{q} * \mathbf{G}$ is the left coset of $\mathbf{G}$ in $SO(3)$ and $(\mathbf{q} * \mathbf{G})_0$ is the set of the first quaternion components of the left coset $\mathbf{q} * \mathbf{G}$. To state it simply, $C(\mathbf{q})$ is a smooth function on the quaternion space and takes the value zero when the boundary misorientation is either the identity or symmetrically equivalent to the identity. This condition results in a parameterization that is compatible with the no-boundary singularity. In the case of the grain boundary space of a crystal with rotational point group symmetry C_1, $\mathbf{G} = C_1 = \{I\}$, $(\mathbf{q} * \mathbf{G})_0 = q_0$ and $C(\mathbf{q}) = \sqrt{1 - q_0^2}$.

The second aspect of the mapping is the definition of $p(\mathbf{q})$. There is a one-to-one correspondence between quaternions $\mathbf{q}$ and axis-angle parameters $(\omega; \vec{a})$ where $\omega \in (0,2\pi)$ and $\vec{a} \in S^2$. Hence, for all quaternions that do not correspond to identity rotations ($\omega \neq \{0,2\pi\}$ or equivalently $q_0 \neq \pm 1$), $(\omega, \vec{a}) = A^{-1}(\mathbf{q})$ is well-defined. $p(\mathbf{q})$ is defined such that $\mathbf{g}(p(\mathbf{q})) = \mathbf{g}\left(\frac{\omega}{2}; -\vec{a}\right)$, where $(\omega, \vec{a}) = A^{-1}(\mathbf{q})$. In terms of quaternion parameters, $p(\mathbf{q})$ takes the form:

$$p(\mathbf{q}) = \frac{1}{\sqrt{2(1 + q_0)}} (1 + q_0 \quad -q_1 \quad -q_2 \quad -q_3) \qquad (4.16)$$

Even though the function A^{-1} is not well defined for $\omega = 0$, i.e. $q_0 = 1$, the function $p(\mathbf{q})$ is well-defined. When $\omega = 0$, the rotation axis $\vec{a}$ is undetermined but this is not an issue in the definition of matrix $p(\mathbf{q})$. If misorientation $\mathbf{q}$ corresponds to a rotation angle $\omega = 0$, the rotation $p(\mathbf{q})$ corresponds to a rotation angle $\frac{\omega}{2} = 0$, and hence it is not necessary to determine the axis of rotation $\vec{a}$. But when $\omega = 2\pi$, i.e. $q_0 = -1$, the function $p(\mathbf{q})$ is undefined. In the definition of the function P, $p(\mathbf{q})$ appears only if $q_0 \neq -1$. The abrupt change in the definition of P in the neighborhood of $q_0 = -1$ does not result in any discontinuity of the mapping. Due to the no-boundary singularity, the function $C(\mathbf{q})$ approaches zero in the neighborhood of $q_0 = -1$, which is essential for the continuity of the mapping. These aspects of the map P, especially in the neighborhood of $q_0 = -1$, are treated in **Appendix B**.

The equivalence relations on the grain boundary space parameterized using $(\mathbf{q}; \vec{r})$ are (refer to **Appendix B** for explicit derivations):

(a) $(\mathbf{q}; \vec{r}) \sim (-\mathbf{q}; \mathbf{g}(\pi, \vec{a}) * \vec{r})$

(b) $(\mathbf{q}; \vec{r}) \sim \left(\left(S^i\right)^{-1} \mathbf{q}(S^j); \mathbf{g}\left(p\left(\left(S^i\right)^{-1} \mathbf{q}(S^j) \right) \left(S^i\right)^{-1} (p(\mathbf{q}))^{-1} \right) * \vec{r} \right)$ \qquad (4.17)

(c) $(\mathbf{q}; \vec{r}) \sim \left(\mathbf{q}^{-1}; (-\vec{r}) \right)$

The first advantage of this parameterization is the absence of an additional condition specifying the 'no-boundary' singularity. The $(\mathbf{q}; \vec{r})$ accounts for the identification of all the boundary normal vectors for zero-misorientation boundaries. The equivalence relation due to grain exchange symmetry (4.17)(c) is now simplified[6] considerably. But the equivalence relations due to the trivial symmetry (4.17)(a) of the rotation space and the relations associated with the rotational symmetries (4.17)(b) of the crystals are more complicated. The relations in Equation (4.17)(b) have a simple form only when $S^i = S^j$ and can be expressed as:

---

[6] It is important to note that by q^{-1} we only mean $(q_0, -q_1, -q_2, -q_3)$ and not $(-q_0, q_1, q_2, q_3)$

$$(\mathbf{q}; \vec{r}) \sim ((S)^{-1}\mathbf{q}(S); \mathbf{g}((S)^{-1}) * \vec{r}), \text{ where } S^i = S^j = S \qquad (4.18)$$

The relations in Equation (4.17)(a) and (b) cannot be simplified any further in a general case and it is due to these complications that the topology of the complete grain boundary space remains intractable. But the $(\mathbf{q}; \vec{r})$ parameterization is very powerful in interpreting symmetries of grain boundary inclinations along a fixed axis of misorientation and allows for the identification of this subset of the grain boundary space as the 3-sphere (S^3). In the following sections, we present the analysis for distribution of inclinations for boundaries with misorientation axis along a fixed, high-symmetry crystal direction.

4.4. Hyperspherical Harmonics for the Single-Axis Grain Boundary Space

We are primarily concerned with the collection of boundary inclinations of boundaries with misorientations confined to a fixed, high-symmetry axis. This subset of the complete grain boundary space is particularly relevant because it belongs to the collection of grain boundaries of perfect fiber-textured materials (thin films and severely extruded metals). There have also been numerous studies where statistical analyses of boundary inclinations that correspond to misorientations along a specific axis (particularly along the symmetry axis of the crystal) are of interest [41, 42, 44, 45, 49, 98-102, 51, 103, 104, 47, 105]. We use the $(\mathbf{q}; \vec{r})$ parameterization developed in the previous section where the vector $\vec{r}$ is related to the measured boundary inclination vector $\vec{n}$ by the relation $\vec{r} = \left[\mathbf{g}(p(\mathbf{q}))\right]^{-1} * C(\mathbf{q}) * \vec{n}$ (Equation (4.14)). The equivalence relations on the complete grain boundary space depend on the crystallographic point group and we begin our analysis with crystals corresponding to point group C_1. The extension to the 32 crystallographic point groups can be made by sequential addition of rotational, inversion and mirror symmetries (refer to **Appendix C**).

We revisit the C_1-misorientation fundamental zone (shown in Figure 4.6(a)) and restrict the misorientations to the fundamental zone, i.e. the misorientation angle ω lies in the range $[0, \pi]$ and the axis of misorientation $\vec{a}$ is such that $a_3 \geq 0$ ($q_0, q_3 \geq 0$). We are interested in grain boundary misorientations along a single axis and since all the axes are equivalent, we investigate the boundary space with misorientations along the z-axis. The boundary inclination space is visualized by attaching a 2-sphere of radius $C(\mathbf{q}) = \sqrt{1 - q_0^2}$ to each misorientation along this

axis. For example, the boundary normal space associated with the boundary misorientation $\mathbf{q} = (\cos(\omega/2), 0, 0, \sin(\omega/2))$, where $\omega = \pi/2$, is shown in Figure 4.6(b).

(a)

(b)

(c)

(d)

Figure 4.6 Single-axis grain boundary space for point group C_1. (a) Grain boundary misorientation fundamental zone for C_1 point group in orthogonal projection and with misorientations along the z-axis highlighted. (b) There is a boundary inclination space (2-sphere) associated with every boundary misorientation. This is represented by attaching the north-pole of a sphere (of radius $C(\mathbf{q}) = \sqrt{1 - q_0^2}$) to each boundary misorientation. Shown here is a 2-sphere of radius $\frac{1}{\sqrt{2}}$ attached to the misorientation corresponding to $(\omega, \vec{a}) = \left(\frac{\pi}{2}, [0\ 0\ 1]\right)$, .i.e. $\vec{q} = \left(0, 0, \frac{1}{\sqrt{2}}\right)$. (c) A solid parametric ball obtained by considering all the boundary inclinations with z-axis as the misorientation axis. (d) A schematic illustration of the mirror symmetry on the surface of the parametric ball; any vector $[r_1 \quad r_2 \quad r_3] \sim [r_1 \quad r_2 \quad -r_3]$.

The boundary parameters that are symmetrically equivalent to the boundary $\left((q_0, 0,0, q_3); \vec{r}\right)$ are given as:

$$\left((q_0, 0,0, q_3); \vec{r}\right) \sim \left(-(q_0, 0,0, q_3); R * \vec{r}\right) \sim \left((q_0, 0,0, -q_3); -\vec{r}\right)$$
$$\sim \left((-q_0, 0,0, q_3); R * (-\vec{r})\right) \tag{4.19}$$

$$\text{where } q_0 = \cos\left(\tfrac{\omega}{2}\right), \ q_3 = \sin\left(\tfrac{\omega}{2}\right), \ R = \mathbf{g}(\pi, [0 \quad 0 \quad 1]).$$

These equivalences are obtained from Equation (4.17) by substituting $q_2 = q_3 = 0$. None of the equivalent boundaries have misorientations that lie in the misorientation fundamental zone except for boundaries with misorientation angle $\omega = \pi$ (i.e. $q_0 = 0$). It can be observed from the above equation (by substituting $q_0 = 0$ and $q_3 = 1$) that the boundary inclination space associated with misorientation angle π has the special symmetry:

$$\left((0,0,0, 1); \vec{r}\right) \sim \left((0,0,0, 1); \mathbf{g}(\pi, [0 \quad 0 \quad 1]) * (-\vec{r})\right) \tag{4.20}$$

The operation $\mathbf{g}(\pi, [0 \quad 0 \quad 1]) * (-\vec{r})$ is a rotation by π along the z-axis and an inversion about the origin, which is equivalent to a mirror perpendicular to the z-axis. This symmetry applies only to the boundaries with misorientations of angle π. The single-axis boundary space, obtained by considering all the misorientation angles $\omega \in [0, \pi]$ along the z-axis, is simply a solid sphere (similar in concept to the parametric ball for the rotation space) where each point parameterizes the boundary; the boundary inclination lies along the vector joining the origin and the point in the solid sphere and the boundary misorientation angle is proportional to the magnitude of the vector $\left(= \sqrt{1 - q_0^2} = \sin(\omega/2)\right)$ (Figure 4.6(c)).

Any boundary associated with a misorientation angle less than π has a unique representative in this solid parametric ball. For boundaries with misorientation π, there are two distinct (yet symmetrically equivalent) representatives, which are related through a mirror perpendicular to the z-axis, as illustrated in Figure 4.6(d). This parametric ball with identifications on the surface is equivalent to a 3-sphere (S^3) with an appropriate equivalence relation. Therefore, we define parameters $(w, x, y, z) \in S^3$, such that

$$w = \cos\left(\frac{\omega}{2}\right); \ x = r_1; y = r_2; z = r_3 \tag{4.21}$$

It is necessary to extend the misorientation angle beyond π to complete the mapping of the boundary parameters to the 3-sphere. The equivalence relation that relates the boundaries in the fundamental zone $(\omega \leq \pi)$ to the boundaries with misorientation angle $\omega \geq \pi$ is obtained from Equation (4.19) and is given by:

$$\left(\left(\cos\left(\frac{\omega}{2}\right), 0,0, \sin\left(\frac{\omega}{2}\right)\right); \vec{r}\right)$$

$$\sim \left(\left(\cos\left(\frac{2\pi - \omega}{2}\right), 0,0, \sin\left(\frac{2\pi - \omega}{2}\right)\right); \mathbf{g}(\pi, [0 \quad 0 \quad 1]) * -\vec{r}\right) \tag{4.22}$$

$$\Rightarrow (w, x, y, z) \sim (-w, x, y, -z)$$

This equivalence relation is obtained by using the grain exchange symmetry and is necessary to obtain a mapping from the z-axis grain boundary space to the 3-sphere. The equivalence relation is compatible with the surface identifications on the parametric ball; the surface of the parametric ball has $w = 0$ and the equivalence relation is essentially $(0, x, y, z) \sim (0, x, y, -z)$ (a mirror-plane perpendicular to the z-axis). Hence, the z-axis boundary space is expressed as:

$$\mathcal{B}_{[0 \quad 0 \quad 1]} = S^3/[(w, x, y, z) \sim (-w, x, y, -z)] \tag{4.23}$$

This formulation can be generalized to the boundary space corresponding to any axis $\vec{a}$ by defining the parameters (w, x, y, z) such that

$$w = q_0 = \cos(\alpha); \begin{bmatrix} x \\ y \\ z \end{bmatrix} = \mathbf{g}\left(\theta, \left[\cos\left(\phi - \frac{\pi}{2}\right) \quad \sin\left(\phi - \frac{\pi}{2}\right) \quad 0\right]\right) * \begin{bmatrix} r_1 \\ r_2 \\ r_3 \end{bmatrix} \tag{4.24}$$

where (θ, ϕ) are the polar coordinates of the axis $\vec{a}$, and the rotation matrix $\mathbf{g}$ in the above equation rotates the vector described by $\vec{a}$ into coincidence with the positive z-axis. The boundary space along $\vec{a}$ is equivalent to the z-axis boundary space and is given by:

$$\mathcal{B}_{\vec{a}} = S^3/[(w, x, y, z) \sim (-w, x, y, -z)] \tag{4.25}$$

where the parameters (w, x, y, z) are defined by Equation (4.24). Summarized in Figure 4.7 are the symmetries present in the boundary inclination space (2-sphere) corresponding to each misorientation along the z-axis.
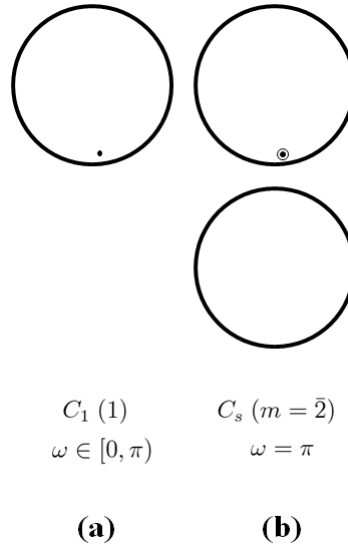
$$C_1\ (1) \qquad\qquad C_s\ (m = \bar{2})$$
$$\omega \in [0, \pi) \qquad\qquad \omega = \pi$$

(a)   **(b)**

Figure 4.7 The equivalence relations on the boundary space can used to determine the symmetries associated with the boundary inclination space (2-sphere). (a) Corresponding to any misorientation with angle $\omega \in [0, \pi)$, the boundary inclination space has no symmetries (C_1). (b) Corresponding to misorientation angle $\omega = \pi$, the boundary inclination space has the symmetry C_s.

In principle, it is possible to express the grain boundary space for any crystallographic point group along any arbitrary axis as a quotient space of the 3-sphere. The equivalence relations to be imposed on the 3-sphere depend on the location of the misorientation axis and the crystallographic point group. Due to significant amount of interest in boundary distributions that are associated only with high-symmetry axes, we confine our analysis to these special axes and the appropriate equivalence relations depend upon the point group and the type of the symmetry axis. These equivalence relations are closely related to the well-know bicrystal symmetries [78] and are discussed in great detail in **Appendix C**.

The existence of a mapping from the single-axis grain boundary space to the quotient space of the 3-sphere (S^3/E) suggests that the 'no-boundary' singularity can be resolved for perfect fiber-textured grain boundary space. Any square-integrable function defined on the 3-sphere can be expanded as a linear combination of the hyperspherical harmonics [59], which are the standard basis functions on the 3-sphere (analogous to spherical harmonics on the 2-sphere and the

Fourier series on a unit-circle). Therefore, a probability distribution of grain boundaries with misorientations along a single axis may be expanded as an infinite linear combination of the hyperspherical harmonics $Z_{l,m}^n(\alpha, \eta, \chi)$ [106] as:

$$f(\alpha, \eta, \chi) = \sum_{n=0}^{\infty} \sum_{l=0}^{n} \sum_{m=-l}^{l} z_{l,m}^n \ Z_{l,m}^n(\alpha, \eta, \chi) \tag{4.26}$$

where α corresponds to the misorientation angle and (η, χ) correspond to the polar coordinates of the boundary normal. The coefficients $z_{l,m}^n$ are determined from the inner product of the function $f(\alpha, \eta, \chi)$ and the appropriate harmonics. It is also necessary that the function f inherit the symmetries of the boundary space (tabulated in Table C.1). The symmetrization procedure of the hyperspherical harmonics has been well developed and utilized for the expansion of Orientation Distribution Functions [59]. The same formulation can be directly extended to symmetrize the hyperspherical harmonics using appropriate symmetries.

4.5. Conclusions

The grain exchange symmetry $(M; \vec{n}) \sim \left(M^{-1}; \mathbf{g}(M^{-1}) * (-\vec{n})\right)$ has profound implications for the topology of the grain boundary misorientation spaces. We have shown that for the 2-D systems, when the grain exchange symmetry is applied to the grain boundary space, the complication due to the 'no-boundary' singularity is removed. Similar analysis revealed the topology of the single-axis grain boundary space to be equivalent to the quotient space of the 3-sphere (with equivalence relations that depend on the crystal direction and crystallographic point group). With this advance, it is now possible to express continuous functions on the space of single-axis grain boundaries as a linear combination of hyperspherical harmonics.

5. Closing Remarks

Understanding the abstract mathematical space inhabited by the grain boundary parameters and the effect of various symmetries on the topology of these spaces is essential for analyzing the vast amount of experimental data available on grain boundaries. To this end, the topology of the misorientation spaces was investigated in order to improve the visualization of grain boundary misorientations. It has also been shown that the 'no-boundary singularity' can be resolved for the 2D grain boundary space and the fiber-textured grain boundary space, which are simplified subspaces of the complete five-parameter grain boundary space. Resolving the singularity is crucial for developing analytical functions relating grain boundary structure and property, for incorporating grain boundary distribution information in modeling and microstructure sensitive design of polycrystalline materials. The major results and implications are summarized below.

5.1. Visual Maps for Grain Boundary Misorientations

The first step in the analysis of grain boundary networks is usually graphical representation, since visualization is, in many cases, tantamount to understanding. Despite recent advances in characterization techniques, there remain fundamental problems in representing grain boundary network information. This situation has arisen in part because grain boundary misorientations have no known mapping to a simple Euclidean space; conventional wisdom suggests that the misorientation space is equivalent to the rotation space, which is known to require five variables for a continuous one-to-one mapping. Contrary to this expectation, it has been shown that the misorientation spaces for grain boundaries of crystals with rotational point groups $D_2(222)$, $D_4(422)$, $D_6(622)$, $T(23)$ and $O(432)$ can indeed be mapped to three-dimensional Euclidean space.

The effect of the symmetries (Equation (1.8)) on the topology of the grain boundary misorientation space is non-trivial. The grain exchange symmetry simplifies the topology of the rotation spaces and results in simply connected spaces, as demonstrated in this thesis for the first time. However, this work has also shown that a combination of the rotational symmetry operations and the grain exchange symmetry is essential for an embedding in $\mathbb{R}^3$. With this advance, grain boundary misorientation maps have been constructed where grain boundary networks can now be "colored", with every color uniquely reflecting the full misorientation information of every boundary in the network. The continuity of the coloring schemes adds to

93

the intuitiveness of these maps since it is possible to directly interpret the distance between boundary misorientations from the difference in contrast of the boundary colors.

Implication for future work: The coloring schemes developed for grain boundary misorientations may also be used for representing any information that involves rotational differences. As shown in section 3.4, the coloring schemes can be utilized to develop more accurate orientation maps. These coloring schemes may prove useful in representing changes in orientations of individual grains during phase transformations such as martensitic phase transformation, or in representing microstructural evolution during plastic deformation etc.

5.2. Topology of the Single-Axis Grain Boundary Space

Insight into the topology of the five-parameter space has been gained in this thesis by first investigating simplified subsets of the grain boundary space. Analysis of the 2D grain boundary space underscored the importance of the grain exchange symmetry in resolving the topology of the grain boundary space. This work reveals some important simplifications to this space. First, when the grain exchange symmetry is applied to the 2D grain boundary space, the complication due to the 'no-boundary' singularity is removed. New parameters (θ', ϕ') (Equation (4.5)) have been introduced to represent the grain boundary parameters and the topology of the boundary space expressed using this parameterization was found to be equivalent to the quotient space of a 2-sphere (S^2).

Since the grain exchange symmetry has a complicated form in the full five-parameter space, a new parameterization has been developed to simplify this relation to some extent (Equation (4.14)). Using this parameterization and extending the analysis of the 2D grain boundary space, the topology of the grain boundary space along a single-axis has been resolved and it was observed that this subspace can be expressed as the quotient space of the 3-sphere, with equivalence relations depending upon the crystal direction and the crystallographic point group under consideration. As a result of these findings, the round metric on the 3-sphere may be used to define distances between grain boundaries with common misorientation axis, and symmetrized hyperspherical harmonics (Equation (4.26)) can be used to express single-axis grain boundary distributions.

Implication for future work: The single-axis grain boundary space is a good approximation for the grain boundaries of fiber textured materials such as thin films. With the aid of the hyperspherical harmonic formulation it is now possible to express distributions of grain boundaries in these materials using continuous functions. Such functions are very useful in simulating microstructures of fiber-textured materials. This framework presents the possibility of expressing the energy of grain boundaries in these materials using a continuous function, and the derivatives of this energy function provide an estimate for the driving force for evolution of grain boundaries. Hence, the expansion of energy function as a linear combination of hyperspherical harmonics may prove extremely valuable in understanding microstructural evolution in these materials.

5.3. Comments on the Five-parameter Grain Boundary Space

Our analysis of the single-axis grain boundary space revealed a critical and previously unappreciated role of grain exchange symmetry in understanding the topology of the space of grain boundary parameters. A new parameterization has been developed in the effort to simplify the grain exchange symmetry but there still remain complications with the equivalence relations on the complete boundary space. The extent of simplification can be better appreciated by comparing the symmetries on the complete grain boundary space for point group C_1 in $(\mathbf{q}; \vec{n})$ and $(\mathbf{q}; \vec{r})$ parameterizations.

Equivalence relations using $(\mathbf{q}; \vec{n})$ parameterization:

(a) $\left((q_0, q_1, q_2, q_3); \vec{r}\right) \sim \left((-q_0, -q_1, -q_2, -q_3); \vec{r}\right)$

(b) $\left((q_0, q_1, q_2, q_3); \vec{r}\right) \sim \left((q_0, -q_1, -q_2, -q_3); \mathbf{g}(\omega, -\vec{a}) * \vec{r}\right)$ (5.1)

(c) $\left((q_0, q_1, q_2, q_3); \vec{r}\right) \sim \left((-q_0, q_1, q_2, q_3); \mathbf{g}(\omega, -\vec{a}) * \vec{r}\right)$

Equivalence relations using $(\mathbf{q}; \vec{r})$ parameterization:

(a) $\left((q_0, q_1, q_2, q_3); \vec{r}\right) \sim \left((-q_0, -q_1, -q_2, -q_3); \mathbf{g}(\pi, \vec{a}) * \vec{r}\right)$

(5.2)

(b) $\left((q_0, q_1, q_2, q_3); \vec{r}\right) \sim \left((q_0, -q_1, -q_2, -q_3); -\vec{r}\right)$

(c) $\left((q_0, q_1, q_2, q_3); \vec{r}\right) \sim \left((-q_0, q_1, q_2, q_3); \mathbf{g}(\pi, \vec{a}) * -\vec{r}\right)$

Whereas the relations in $(\mathbf{q}; \vec{n})$ depend on both the angle (ω) and axis $(\vec{a})$ of the misorientation, the equivalences expressed using $(\mathbf{q}; \vec{r})$ depend only on the axis of misorientation. Such a simplification suffices when the single-axis grain boundary space is under consideration since the misorientation axis $\vec{a}$ is fixed. However, in order to incorporate complete boundary information, the grain exchange symmetry needs to be simplified further. Other important aspects of the equivalence relations are the crystallographic point group symmetries, which, as observed in the analysis of the misorientation spaces, have a non-trivial effect on the topology of the grain boundary space. It is suspected that a combination of the rotational symmetry elements and the grain exchange symmetry will be necessary to resolve the 'no-boundary' singularity in the complete grain boundary space.

Appendix A: Explicit Mappings for Misorientation Spaces

The explicit mappings for grain boundary misorientation spaces are presented in this appendix. Equations (A1), (A2), (A3), (A4) and (A5) provide continuous and bijective mappings from the misorientation spaces of $C_2(2)$, $C_3(3)$, $C_4(4)$, $C_6(6)$ and $D_3(32)$ to the $C_1(1)$ misorientation space and hence demonstrate topological equivalence between them. Topological equivalence between the grain boundary misorientation spaces of point groups $D_2(222)$, $D_4(422)$ and $D_6(622)$ is provided by continuous maps from $D_4(422)$ to $D_2(222)$ in Equation (A6) and the map from $D_6(622)$ to $D_2(222)$ in Equation (A7) . The embeddings of misorientation spaces of $D_2(222)$, $T(23)$ and $O(432)$ in $\mathbb{R}^3$ are provided in Equations (A8), (A9) and (A10) respectively.

The mapping from C_2 to C_1 is given by:

1) $(x_1, y_1, z_1) \equiv \sqrt{\dfrac{q_1^2 + q_2^2 + 2q_3^2}{q_1^2 + q_2^2 + q_3^2}}(q_1, q_2, q_3)$

2) $(x_2, y_2, z_2) \equiv \left(\sqrt{x_1^2 + y_1^2} \cos 2\phi , \sqrt{x_1^2 + y_1^2} \sin 2\phi , z_1 \right);$

$\phi = \tan \dfrac{y_1}{x_1}$

$\qquad\qquad\qquad\qquad\qquad\qquad\qquad$ (A1)

3) $(x_3, y_3, z_3) \equiv \left(x_2, y_2, z_2 - \sqrt{1 - x_2^2 - y_2^2} \right)$

4) $|x_4 \quad y_4 \quad z_4\rangle \equiv \mathbf{g}(\pi, [100]) * |x_3 \quad y_3 \quad z_3\rangle;$

The mapping from C_3 to C_1 is given by:

1) $(x_1, y_1, z_1) \equiv \sqrt{\dfrac{q_1^2 + q_2^2 + 4q_3^2}{q_1^2 + q_2^2 + q_3^2}}(q_1, q_2, q_3)$

2) $(x_2, y_2, z_2) \equiv \left(\sqrt{x_1^2 + y_1^2} \cos 3\phi , \sqrt{x_1^2 + y_1^2} \sin 3\phi , z_1 \right);$

$\phi = \tan \dfrac{y_1}{x_1}$

$\qquad\qquad\qquad\qquad\qquad\qquad\qquad$ (A2)

3) $(x_3, y_3, z_3) \equiv \left(x_2, y_2, z_2 - \sqrt{1 - x_2^2 - y_2^2} \right)$

4) $|x_4 \quad y_4 \quad z_4\rangle \equiv \mathbf{g}(\pi, [100]) * |x_3 \quad y_3 \quad z_3\rangle;$

The mapping from C_4 to C_1 is given by:

1) $(x_1, y_1, z_1) \equiv \sqrt{\dfrac{q_1^2 + q_2^2 + \left(1 + (1+\sqrt{2})^2\right)q_3^2}{q_1^2 + q_2^2 + q_3^2}}\,(q_1, q_2, q_3)$

2) $(x_2, y_2, z_2) \equiv \left(\sqrt{x_1^2 + y_1^2}\cos 4\phi\,, \sqrt{x_1^2 + y_1^2}\sin 4\phi\,, z_1\right);$

$\phi = \tan\dfrac{y_1}{x_1}$

3) $(x_3, y_3, z_3) \equiv \left(x_2, y_2, z_2 - \sqrt{1 - x_2^2 - y_2^2}\right)$

4) $|x_4 \quad y_4 \quad z_4\rangle \equiv \mathbf{g}(\pi, [100]) * |x_3 \quad y_3 \quad z_3\rangle;$

(A3)

The mapping from C_6 to C_1 is given by:

1) $(x_1, y_1, z_1) \equiv \sqrt{\dfrac{q_1^2 + q_2^2 + \left(1 + (2+\sqrt{3})^2\right)q_3^2}{q_1^2 + q_2^2 + q_3^2}}\,(q_1, q_2, q_3)$

2) $(x_2, y_2, z_2) \equiv \left(\sqrt{x_1^2 + y_1^2}\cos 6\phi\,, \sqrt{x_1^2 + y_1^2}\sin 6\phi\,, z_1\right);$

$\phi = \tan\dfrac{y_1}{x_1}$

3) $(x_3, y_3, z_3) \equiv \left(x_2, y_2, z_2 - \sqrt{1 - x_2^2 - y_2^2}\right)$

4) $|x_4 \quad y_4 \quad z_4\rangle \equiv \mathbf{g}(\pi, [100]) * |x_3 \quad y_3 \quad z_3\rangle;$

(A4)

The mapping from D_3 to C_1 is given by:

1) $(x_1, y_1, z_1) \equiv \dfrac{1}{\sqrt{1-q_1^2-q_2^2-q_3^2}} (q_1, q_2, q_3)$

2) $(x_2, y_2, z_2) \equiv \left(\dfrac{x_1^2}{x_1^2+y_1^2}, \dfrac{x_1 y_1}{x_1^2+y_1^2}, z_1\left(\sqrt{\dfrac{3}{2}}\right) \right)$

3) $(x_3, y_3, z_3) \equiv \left(\sqrt{x_2^2 + y_2^2} \cos 3\phi, \sqrt{x_2^2 + y_2^2} \sin 3\phi, z_2 \right);$

$\phi = \tan\dfrac{y_2}{x_2}$

4) $(x_4, y_4, z_4) \equiv \left(x_3\sqrt{1 - z_3^2}, y_3\sqrt{1 - z_3^2}, z_3 \right)$

5) $|x_5\ y_5\ z_5\rangle \equiv \mathbf{g}\left(\dfrac{2\pi}{3}, [1\ 1\ 1] \right) * |x_4\ y_4\ z_4\rangle;$

$\qquad\qquad\qquad\qquad\qquad\qquad\qquad\qquad\qquad\qquad\qquad\qquad$ (A5)

6) $(x_6, y_6, z_6) \equiv \begin{cases} (x_5, y_5, z_5); r = \sqrt{y_5^2 + z_5^2} & for\ r \le \dfrac{1}{\sqrt{2}} \\ (x_5, r\sin(\phi_1), r\cos(\phi_1)); & for\ r > \dfrac{1}{\sqrt{2}} \end{cases}$

$\phi_1 = \dfrac{\arcsin\left(\frac{y_5}{r}\right)}{\arcsin\left(\frac{1}{\sqrt{2}r}\right)} \left(\dfrac{\pi}{2}\right)$

7) $(x_7, y_7, z_7) \equiv \left(\sqrt{x_6^2 + y_6^2} \cos 2\phi, \sqrt{x_6^2 + y_6^2} \sin 2\phi, z_6 \right);$

$\phi = \tan\dfrac{y_6}{x_6}$

8) $(x_8, y_8, z_8) \equiv \left(x_7, y_7, z_7 - \sqrt{1 - x_7^2 - y_7^2} \right)$

9) $|x_9\ y_9\ z_9\rangle \equiv \mathbf{g}(\pi, [100]) * |x_8\ y_8\ z_8\rangle;$

The mapping from D_4 to D_2 is given by:

1) $(x, y, z) \equiv \dfrac{1}{\sqrt{1-q_1^2-q_2^2-q_3^2}}(q_1, q_2, q_3)$

2) $(x_1, y_1, z_1) \equiv \begin{cases} \left(\dfrac{x^2}{\sqrt{x^2+y^2}}, \dfrac{xy}{\sqrt{x^2+y^2}}, \dfrac{z}{\tan\left(\frac{\pi}{8}\right)} \right) & for \ \tan\left(\frac{y}{x}\right) \le \dfrac{\pi}{8} \\ \left(\dfrac{x(x+y)}{\sqrt{2(x^2+y^2)}}, \dfrac{y(x+y)}{\sqrt{2(x^2+y^2)}}, \dfrac{z}{\tan\left(\frac{\pi}{8}\right)} \right) & otherwise. \end{cases}$

3) $(x_2, y_2, z_2) \equiv \left(\dfrac{x_1^2-y_1^2}{\sqrt{x_1^2+y_1^2}}, \dfrac{2x_1 y_1}{\sqrt{x_1^2+y_1^2}}, z_1 \right)$

4) $(x_3, y_3, z_3) \equiv \left(\dfrac{x_2\sqrt{x_2^2+y_2^2}}{\max(x_2,y_2)}, \dfrac{y_2\sqrt{x_2^2+y_2^2}}{\max(x_2,y_2)}, z_2 \right)$

5) $(x_4, y_4, z_4) \equiv \dfrac{1}{\sqrt{1+x_3^2+y_3^2+z_3^2}}(x_3, y_3, z_3)$

(A6)

The mapping from D_6 to D_2 is given by:

1) $(x, y, z) \equiv \dfrac{1}{\sqrt{1-q_1^2-q_2^2-q_3^2}}(q_1, q_2, q_3)$

2) $(x_1, y_1, z_1) \equiv \begin{cases} \left(\dfrac{x^2}{\sqrt{x^2+y^2}}, \dfrac{xy}{\sqrt{x^2+y^2}}, \dfrac{z}{\tan\left(\frac{\pi}{12}\right)} \right) & for \ \tan\left(\frac{y}{x}\right) \le \dfrac{\pi}{12} \\ \left(\dfrac{x(\sqrt{3}x+y)}{2\sqrt{(x^2+y^2)}}, \dfrac{y(\sqrt{3}x+y)}{2\sqrt{(x^2+y^2)}}, \dfrac{z}{\tan\left(\frac{\pi}{12}\right)} \right) & otherwise. \end{cases}$

3) $(x_2, y_2, z_2) \equiv \left(\dfrac{4x_1^3}{x_1^2+y_1^2} - 3x_1, 3y_1 - \dfrac{4y_1^3}{x_1^2+y_1^2}, z_1 \right)$

4) $(x_3, y_3, z_3) \equiv \left(\dfrac{x_2\sqrt{x_2^2+y_2^2}}{\max(x_2,y_2)}, \dfrac{y_2\sqrt{x_2^2+y_2^2}}{\max(x_2,y_2)}, z_2 \right)$

5) $(x_4, y_4, z_4) \equiv \dfrac{1}{\sqrt{1+x_3^2+y_3^2+z_3^2}}(x_3, y_3, z_3)$

(A7)

The embedding D_2 in $\mathbb{R}^3$ is given by:

1) $(x, y, z) \equiv \dfrac{1}{\sqrt{1-q_1^2-q_2^2-q_3^2}} (q_1, q_2, q_3)$

2) $(x_1, y_1, z_1) \equiv \dfrac{\sqrt{3}\,\max(x,y,z)}{x+y+z}(x, y, z)$

3) $|x_2 \quad y_2 \quad z_2\rangle \equiv R * |x_1 \quad y_1 \quad z_1\rangle$;

$R = \mathbf{g}\left(-\text{acos}\left(\dfrac{1}{\sqrt{3}}\right), [-1\,1\,0], \right) * \mathbf{g}\left(\dfrac{\pi}{12}, [1\,1\,1]\right)$

4) $(x_3, y_3, z_3) = \left(\dfrac{x_2 \sin\left(\frac{\pi}{6} + mod\left(\phi_1, \frac{2\pi}{3}\right)\right)}{\sin\left(\frac{\pi}{6}\right)}, \dfrac{y_2 \sin\left(\frac{\pi}{6} + mod\left(\phi_1, \frac{2\pi}{3}\right)\right)}{\sin\left(\frac{\pi}{6}\right)}, z_2 - 1 \right)$;

$\phi_1 = \text{atan}\left(\dfrac{y_2}{x_2}\right)$ where "mod" represents the modulo operation.

5) $(x_4, y_4, z_4) \equiv \dfrac{\left(\sqrt{x_3^2+y_3^2}-z_3\right)}{\sqrt{x_3^2+y_3^2+z_3^2}}(x_3, y_3, z_3)$

$\hspace{6cm}$ (A8)

6) $(x_5, y_5, z_5) \equiv \left(\sqrt{x_4^2 + y_4^2}\,\cos\left(\dfrac{3\left(mod\left(\phi_2, \frac{2\pi}{3}\right)\right)}{2}\right), \sqrt{x_4^2 + y_4^2}\,\sin\left(\dfrac{3\left(mod\left(\phi_2, \frac{2\pi}{3}\right)\right)}{2}\right), z_4 \right)$;

$$\phi_2 = \text{atan}\left(\dfrac{y_4}{x_4}\right)$$

7) $(x_6, y_6, z_6) \equiv \left(x_5, \sqrt{y_5^2 + z_5^2}\,\sin(2\phi_3), -\sqrt{y_5^2 + z_5^2}\,\cos(2\phi_3) \right)$;

$$\phi_3 = \text{atan}\left(\dfrac{y_5}{-z_5}\right)$$

8) $(x_7, y_7, z_7) \equiv \left(\sqrt{x_6^2 + y_6^2}\,\cos\left(\dfrac{2\phi_4}{3} + \left(\phi_2 - mod\left(\phi_2, \frac{2\pi}{3}\right)\right)\right), \right.$

$\left. \sqrt{x_6^2 + y_6^2}\,\sin\left(\dfrac{2\phi_4}{3} + \left(\phi_2 - mod\left(\phi_2, \frac{2\pi}{3}\right)\right)\right), z_6 \right)$; $\phi_4 = \text{atan}\left(\dfrac{y_6}{x_6}\right)$

The embedding T in $\mathbb{R}^3$ is given by:

1) $(x, y, z) \equiv \dfrac{1}{\sqrt{1-q_1^2-q_2^2-q_3^2}}(q_1, q_2, q_3)$

2) $|x_1 \quad y_1 \quad z_1\rangle \equiv R * |x \quad y \quad z\rangle;$

$R = \mathbf{g}\left(-\mathrm{acos}\left(\frac{1}{\sqrt{3}}\right), [-110]\right) * \mathbf{g}\left(\frac{-\pi}{4}, [1\,1\,1]\right)$

3) $(x_2, y_2, z_2) \equiv \left(\dfrac{x_1(\sqrt{3}y_1+x_1)(x_1+\sqrt{3}y_1)(x_1-\sqrt{3}y_1)}{2(x_1^2+y_1^2)^{\frac{3}{2}}}, \dfrac{y_1(\sqrt{3}y_1+x_1)(y_1+\sqrt{3}x_1)(\sqrt{3}x_1-y_1)}{2(x_1^2+y_1^2)^{\frac{3}{2}}}, z_1\right)$

(A9)

The embedding O in $\mathbb{R}^3$ is given by:

1) $(x, y, z) \equiv \dfrac{1}{\sqrt{1-q_1^2-q_2^2-q_3^2}}(q_1, q_2, q_3)$

2) $(x_1, y_1, z_1) \equiv \begin{cases} \left(x, \dfrac{x(y+z)}{(1-x)}, \dfrac{xz(y+z)}{y(1-x)}\right) & for\ x \geq \frac{1}{3}\ and\ \tan\left(\frac{z}{y}\right) \geq \left(\frac{1-2x}{x}\right) \\ (x, y, z) & otherwise \end{cases}$

3) $|x_2, y_2, z_2\rangle \equiv \mathbf{g}\left([100], \frac{3\pi}{8}\right) * |x_1 - \tan\left(\frac{\pi}{8}\right), y_1, z_1\rangle$

4) $(x_3, y_3, z_3) \equiv \left(x_2, y_2\left(1 + \frac{y_2}{z_2}\tan\left(\frac{\pi}{8}\right)\right), z_2 + y_2 \tan\left(\frac{\pi}{8}\right)\right)$

5) $(x_4, y_4, z_4) \equiv \left(x_3, \dfrac{y_3\cos\left(\frac{\pi}{8}\right)}{\tan\left(\frac{\pi}{8}\right)}, z_3 - \dfrac{x_3}{\cos\left(\frac{\pi}{8}\right)}\right)$

(A10)

6) $(x_5, y_5, z_5) \equiv (x_4(\sin\phi + |\cos\phi|), y_4(\sin\phi + |\cos\phi|), z_4);$

$$\phi = \mathrm{atan}\left(-\frac{x_4}{y_4}\right)$$

7) $(x_6, y_6, z_6) \equiv \left(-\sqrt{x_5^2 + y_5^2}\cos 2\phi_1, \sqrt{x_5^2 + y_5^2}\sin 2\phi_1, z_5\right);$

$$\phi_1 = \mathrm{atan}\left(-\frac{y_5}{x_5}\right)$$

Appendix B: Mathematical Aspects of the Symmetric Parameterization

B.1. Discontinuity in Morawiec's Symmetric Parameterization

The discontinuity in the symmetric parameterization arises due to the convention necessary to define this representation. For example, consider two grain boundary parameters $(M_1; \ \vec{n}) = ((\omega, \vec{a}); \ \vec{n})$ and $(M_2; \ \vec{n}) = ((\omega, -\vec{a}); \ \vec{n})$. As $\omega \to \pi$, $(M_1; \ \vec{n}) \to (M; \ \vec{n}) = ((\pi, \vec{a}); \ \vec{n})$ and $(M_2; \ \vec{n}) \to (M; \ \vec{n}) = ((-\pi, \vec{a}); \ \vec{n})$. Since $(\pi, \vec{a}) \sim (-\pi, \vec{a})$, which is the trivial symmetry of the rotation space, the distance $d((M_1; \ \vec{n}), (M_2; \ \vec{n}))$ approaches zero as $\omega \to \pi$. If the mapping $f : (M; \ \vec{n}) \to (N; \ \vec{r})$ is continuous then $d(f(M_1; \ \vec{n}), f(M_2; \ \vec{n}))$ must approach zero as $\omega \to \pi$. But,

$$\lim_{\omega \to \pi} (N_1; \ \vec{r_1}) = \left(\mathbf{g}\left(\frac{\pi}{2}, \vec{a}\right); \ \left(\frac{\pi}{2}, -\vec{a}\right) * \vec{n} \right)$$

$$\lim_{\omega \to \pi} (N_2; \ \vec{r_2}) = \left(\mathbf{g}\left(\frac{\pi}{2}, -\vec{a}\right); \ \left(\frac{\pi}{2}, \vec{a}\right) * \vec{n} \right)$$

(B1)

And,

$$\lim_{\omega \to \pi} d(f(M_1; \ \vec{n}), f(M_2; \ \vec{n})) = d((N_1; \ \vec{r}), (N_2; \ \vec{r})) \neq 0 \tag{B2}$$

Since $d(N_1, N_2) \neq 0$ and $d(r_1, r_2) \neq 0$. Hence the mapping proposed for the symmetric representation is not continuous and is not topologically consistent (not a homeomorphism).

B.2. Continuity of the (q; r) parameterization in the neighborhood of $\omega = 2\pi$

The topological consistency of the mapping defined in section 4.3.1 hinges on the definition of the mapping in the neighborhood of $\omega = 2\pi$. To prove that the mapping is continuous we prove the following condition:

$$\lim_{\omega \to 2\pi} P(\mathbf{q}; \ \vec{n}) = P\big((-1,0,0,0); \vec{n}\big) = \Big((-1,0,0,0); \vec{0}\Big) \tag{B3}$$

$$\text{for all } \vec{a} \in S^2 \text{ where } A^{-1}(\mathbf{q}) = (\omega, \vec{a})$$

Since $P(\mathbf{q}; \ \vec{n}) = \big(\mathbf{q}; \mathbf{g}(p(\mathbf{q})) * [C(\mathbf{q})(\vec{n})]\big)$, we obtain

$$\lim_{\omega \to 2\pi} P(\mathbf{q}; \ \vec{n}) = \lim_{\omega \to 2\pi} \big(\mathbf{q}; \mathbf{g}(p(\mathbf{q})) * [C(\mathbf{q})(\vec{n})]\big)$$

$$= \lim_{\omega \to 2\pi} \Big(\mathbf{q}; \mathbf{g}\Big(\frac{\omega}{2}, \vec{a}\Big) * [C(\mathbf{q})(\vec{n})]\Big) \tag{B4}$$

$$= \Big((-1,0,0,0); \mathbf{g}(\pi, \vec{a}) * \Big[\lim_{\omega \to 2\pi} C(\mathbf{q})(\vec{n})\Big]\Big)$$

The important requirement here is $\lim_{\omega \to 2\pi} C(\mathbf{q}) = 0$, which is trivially satisfied since $q_0 \to -1$ and $\max\{((\mathbf{q} * \mathbf{G})_0)^2\} \to 1$ as $\omega \to 1$. Even though the matrix $\mathbf{g}(\pi, \vec{a})$ depends on the choice of $\vec{a}$, the scaling function approaches zero as $\omega \to 0$ and hence the mapping is continuous in the neighborhood of $q_0 = -1$.

B.3. Equivalence Relations in the (q; r) parameterization

The equivalence relations expressed using the symmetric parameters $(\mathbf{q}; \vec{r})$ depend upon the type of symmetry under consideration. For example, the trivial symmetry of the rotation space in the quaternion parameterization implies that $P(\mathbf{q}; \vec{n}) \sim P(-\mathbf{q}; \vec{n})$. This equivalence relation expressed in terms of the parameters $(\mathbf{q}; \vec{r})$ is:

$$P(\mathbf{q}; \vec{n}) \sim P(-\mathbf{q}; \vec{n}) \Rightarrow \left(\mathbf{q}; \; \mathbf{g}\left(\frac{\omega}{2}, -\vec{a}\right) * \vec{n}\right) \sim \left(-\mathbf{q}; \; \mathbf{g}\left(\pi - \frac{\omega}{2}, \vec{a}\right) * \vec{n}\right) \qquad \text{(B5)}$$

where $A^{-1}(\mathbf{q}) = (\omega, \vec{a})$. According to the definition of $(\mathbf{q}; \vec{r})$, we observe that

$$\vec{r} = \mathbf{g}\left(\frac{\omega}{2}, -\vec{a}\right) * \vec{n} \Rightarrow \vec{n} = \left[\mathbf{g}\left(\frac{\omega}{2}, -\vec{a}\right)\right]^{-1} * \vec{r} \text{ and } \vec{r}' = \mathbf{g}\left(\pi - \frac{\omega}{2}, \vec{a}\right) * \vec{n} \qquad \text{(B6)}$$

By substituting $\vec{n}$ in the equation of $\vec{r}'$, we obtain

$$\vec{r}' = \mathbf{g}\left(\pi - \frac{\omega}{2}, \vec{a}\right) * \left[\mathbf{g}\left(\frac{\omega}{2}, -\vec{a}\right)\right]^{-1} * \vec{r} = \mathbf{g}(\pi, \vec{a}) * \vec{r}$$

$$\qquad \text{(B7)}$$

$$(\mathbf{q}; \vec{r}) \sim (-\mathbf{q}; \vec{r}') \Rightarrow (\mathbf{q}; \vec{r}) \sim (-\mathbf{q}; \mathbf{g}(\pi, \vec{a}) * \vec{r})$$

Hence, the relation $(\mathbf{q}; \vec{r}) \sim (-\mathbf{q}; \mathbf{g}(\pi, \vec{a}) * \vec{r})$ is the trivial symmetry of the rotation space expressed in the symmetric parameterization.

The grain exchange symmetry can be derived in a similar fashion. If $\mathbf{q} = (q_0, q_1, q_2, q_3)$ then there are two possibilities for $\mathbf{q}^{-1} = \pm(q_0, -q_1, -q_2, -q_3)$, which are related to each other by the trivial symmetry. In this formulation, we use $\mathbf{q}^{-1} = (q_0, -q_1, -q_2, -q_3)$. Hence, if $A^{-1}(\mathbf{q}) = (\omega, \vec{a})$, then $A^{-1}(\mathbf{q}^{-1}) = (\omega, -\vec{a})$. The grain exchange symmetry is now obtained as follows:

$$P(\mathbf{q}; \vec{n}) \sim P(\mathbf{q}^{-1}; \mathbf{g}(\mathbf{q}^{-1}) * -\vec{n})$$

$$\qquad \text{(B8)}$$

$$\Rightarrow \left(\mathbf{q}; \; \mathbf{g}\left(\frac{\omega}{2}, -\vec{a}\right) * \vec{n}\right) \sim \left(\mathbf{q}^{-1}; \; \mathbf{g}\left(\pi - \frac{\omega}{2}, \vec{a}\right) * \mathbf{g}(\omega, -\vec{a}) * -\vec{n}\right)$$

And,

$$\vec{r} = \mathbf{g}\left(\frac{\omega}{2}, -\vec{a}\right) * \vec{n} \Rightarrow \vec{n} = \left[\mathbf{g}\left(\frac{\omega}{2}, -\vec{a}\right)\right]^{-1} * \vec{r}$$

$$\vec{r}\,' = \mathbf{g}\left(\pi - \frac{\omega}{2}, \vec{a}\right) * \mathbf{g}(\omega, -\vec{a}) * -\vec{n}$$

$$= \mathbf{g}\left(\pi - \frac{\omega}{2}, \vec{a}\right) * \mathbf{g}(\omega, -\vec{a}) * \left[\mathbf{g}\left(\frac{\omega}{2}, -\vec{a}\right)\right]^{-1} * -\vec{r}$$

$$= -\vec{r}$$

(B9)

Therefore, the grain exchange symmetry is given by:

$$\left((q_0, q_1, q_2, q_3); \vec{r}\right) \sim \left((q_0, -q_1, -q_2, -q_3); -\vec{r}\right)$$

(B10)

Similarly, the equivalence relations due to the rotational symmetry operations can be expressed as:

$$P(\mathbf{q}; \ \vec{n}) \sim P(\mathbf{q}^{-1}; \mathbf{g}(\mathbf{q}^{-1}) * -\vec{n}) \Rightarrow$$

$$(\mathbf{q}; \vec{r}) \sim \left(\left(S^i\right)^{-1}\mathbf{q}(S^j); \mathbf{g}\left(p\left(\left(S^i\right)^{-1}\mathbf{q}(S^j)\right)\left(S^i\right)^{-1}(p(\mathbf{q}))^{-1}\right) * \vec{r}\right)$$

(B11)

Appendix C: Bicrystal Symmetries

In section 4.4, we presented the mapping between the single-axis grain boundary space for any crystal direction and the quotient space of the 3-sphere for crystals that belong to crystallographic point group C_1. In order to extend this formulation to the single-axis grain boundary space for any crystallographic point group, it is essential to derive the bicrystal symmetries pertaining to the crystal direction and the point group under consideration. In this section we derive the relevant symmetries of the grain boundary space with the misorientation axis confined to a high-symmetry axis in all the remaining rotational point group symmetries using the $(\mathbf{q}; \vec{r})$ parameterization.

C.1. Point Groups C_2, C_3, C_4 and C_6

Analogous to the analysis of the single-axis grain boundary space of C_1 point group, we restrict the grain boundary misorientations to the fundamental zone of the C_2 point group (shown in Figure 2.6(a)), i.e. $q_0 \geq 0$, $0 \leq q_3 \leq q_0$ and $q_2 \geq 0$. In the case of C_2 point group, boundary distributions along the z-axis are of interest. The boundary parameters have the form $(\mathbf{q}; \vec{r}) = \left(\left(\cos \left(\frac{\omega}{2} \right), 0,0, \sin \left(\frac{\omega}{2} \right) \right); \vec{r} \right)$, where $\omega \in \left[0, \frac{\pi}{2} \right]$. The relevant symmetries, such that the misorientations of the symmetrically equivalent boundaries fall within the fundamental zone, obtained from Equation (4.17) are the following:

(a) $\left((q_0, 0,0, q_3); \vec{r} \right) \sim \left((q_0, 0,0, q_3); R * \vec{r} \right)$

(b) $\left(\left(\cos \left(\frac{\pi}{4} \right), 0,0, \sin \left(\frac{\pi}{4} \right) \right); \vec{r} \right) \sim \left(\left(\cos \left(\frac{\pi}{4} \right), 0,0, \sin \left(\frac{\pi}{4} \right) \right); \mathbf{g} \left(\frac{\pi}{2}; [0 \quad 0 \quad 1] \right) * (-\vec{r}) \right)$

(C1)

where $q_0 = \cos \left(\frac{\omega}{2} \right)$, $q_3 = \sin \left(\frac{\omega}{2} \right)$, $\omega \in [0, \pi/2]$, $R = \mathbf{g}(\pi, [0 \quad 0 \quad 1])$.

The first equivalence relation suggests that the boundary inclination space (2-sphere) associated with any boundary misorientation along the z-axis has a two-fold rotational symmetry (i.e. C_2 point symmetry). The second equivalence relation, confined to the misorientation $(\omega, \vec{a}) = (\pi/2, [0 \quad 0 \quad 1])$, has the symmetry $S_4(\bar{4})$. The symmetries on the inclination space for different misorientation angles are summarized in Figure C.1.
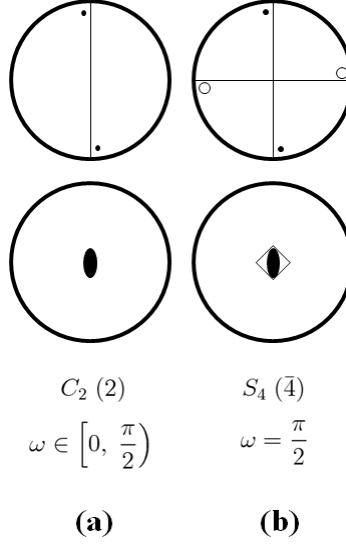
The collection of all the boundary inclinations for misorientation angles $\omega \in [0, \pi/2]$ along the z-axis is a solid parametric ball of outer radius $\sin(\pi/4)$, with additional symmetries on the surface. The equivalence between this z-axis boundary space and the 3-sphere can be established by using the parameters $(w, x, y, z) \in S^3$ such that

$$w = \frac{\sqrt{q_0^2 - \left(\cos\left(\frac{\omega_{max}}{2}\right)\right)^2}}{\sin\left(\frac{\omega_{max}}{2}\right)} \quad ; \quad \vec{v} = \begin{bmatrix} x \\ y \\ z \end{bmatrix} = \frac{1}{\sin\left(\frac{\omega_{max}}{2}\right)} \begin{bmatrix} r_1 \\ r_2 \\ r_3 \end{bmatrix} \text{ where } (w, x, y, z) \in S^3$$

$$\mathcal{B} = S^3/E$$

$$\text{(C2)}$$

$$\text{(a) } (w, \vec{v}) \sim (w, \vec{v}') \qquad \vec{v}' = \mathbf{g}\left(\omega_{max}; \vec{b}\right) * \vec{v}$$

$$\text{(b) } (w, \vec{v}) \sim (-w, -\vec{v}'') \qquad \vec{v}'' = \mathbf{g}\left(\frac{\omega_{max}}{2}; \vec{b}\right) * \vec{v}$$

$$\text{where } \omega_{max} = \pi \text{ and } \vec{b} = [0 \quad 0 \quad 1]$$

The above formulation can be generalized to point group C_n, .i.e. the grain boundary space along the z-axis for crystals with point group C_n is equivalent to the quotient space S^3/E and the equivalence can be established by using the parameters $(w, x, y, z) \in S^3$ such that

$$w = \frac{\sqrt{q_0^2 - \left(\cos\left(\frac{\omega_{max}}{2}\right)\right)^2}}{\sin\left(\frac{\omega_{max}}{2}\right)} \quad ; \quad \vec{v} = \begin{bmatrix} x \\ y \\ z \end{bmatrix} = \frac{1}{\sin\left(\frac{\omega_{max}}{2}\right)} \begin{bmatrix} r_1 \\ r_2 \\ r_3 \end{bmatrix} \text{ where } (w, x, y, z) \in S^3$$

$$\mathcal{B} = S^3/E$$

(C3)

(a) $(w, \vec{v}) \sim (w, \vec{v}')$ $\qquad \vec{v}' = \mathbf{g}\left(\omega_{max}; \vec{b}\right) * \vec{v}$

(b) $(w, \vec{v}) \sim (-w, -\vec{v}'')$ $\qquad \vec{v}'' = \mathbf{g}\left(\frac{\omega_{max}}{2}; \vec{b}\right) * \vec{v}$

where $\omega_{max} = \frac{2\pi}{n}$ and $\vec{b} = \begin{bmatrix} 0 & 0 & 1 \end{bmatrix}$

The symmetry relations imply an n-fold rotational symmetry (C_n) for the boundary inclination space (2-sphere) for all misorientation angles $\omega \in [0, \pi/n)$ and $\overline{2n}$ (rotation of π/n followed by inversion) symmetry for the boundary inclination space corresponding to a misorientation angle of $\omega = \pi/n$. The symmetries of the boundary inclination space for point groups C_3, C_4 and C_6 are summarized in Figure C.2.
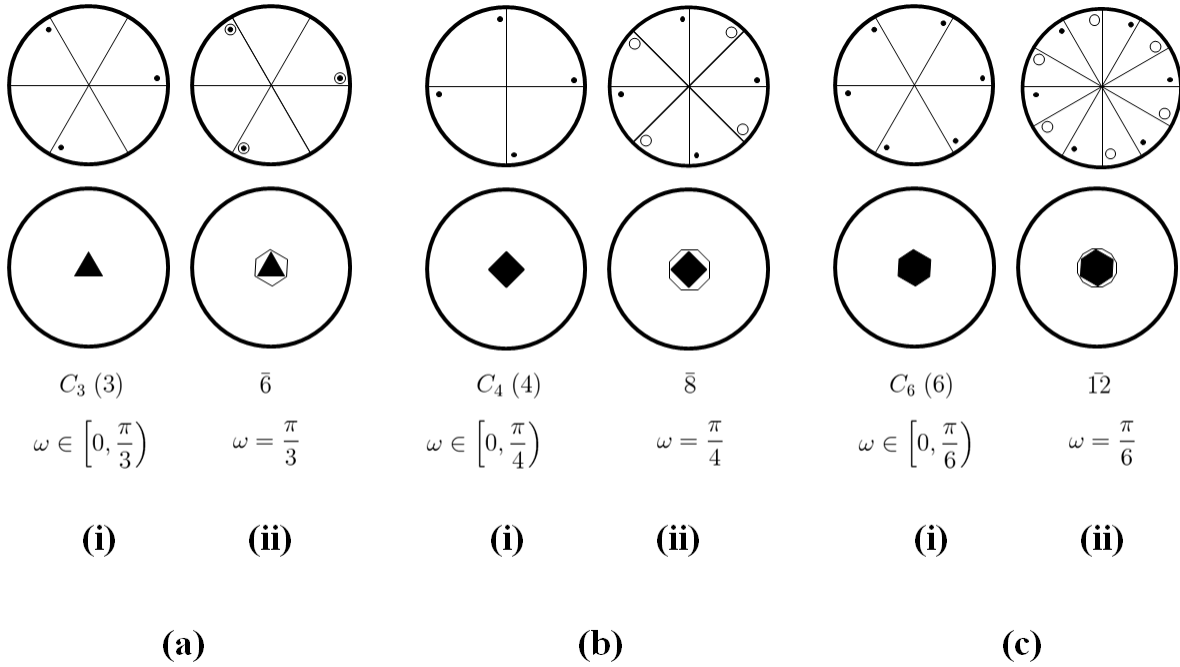
Figure C.2 Symmetries associated with the boundary inclination space for misorientations along the z-axis for crystals with point group C_n: (a) $C_3 (n = 3)$, (b) $C_4 (n = 4)$, and (c) $C_6 (n = 6)$. (i) Corresponding to any misorientation with angle $\omega \in [0, \pi/n)$, the boundary inclination space has no symmetries (C_n). (ii) Corresponding to misorientation angle $\omega = \pi/n$, the boundary inclination space has the symmetry $\overline{2n}$.

C.2. Point Groups D_2, D_3, D_4, D_6, T and O

In the case of D_2 point group symmetry, boundary distributions along the x, y and z-axes, which are the 2-fold rotational symmetry axes, are of interest. Since these three high-symmetry axes are equivalent to each other, we consider the distributions only along the z-axis here. The boundary parameters have the form $(\mathbf{q}; \vec{r}) = \left(\left(\cos\left(\frac{\omega}{2}\right), 0, 0, \sin\left(\frac{\omega}{2}\right)\right); \vec{r}\right)$, where $\omega \in \left[0, \frac{\pi}{2}\right]$. The boundary space is similar to the z-axis boundary space of the C_2 point group but there exist additional symmetries due to the 2-fold symmetries along the x and y-axes. The relevant symmetries obtained from Equation (4.17) are the following:

(a) $\left((q_0, 0, 0, q_3); \vec{r}\right) \sim \left((q_0, 0, 0, q_3); R_1 * \vec{r}\right)$

(b) $\left((q_0, 0, 0, q_3); \vec{r}\right) \sim \left((q_0, 0, 0, q_3); R_2 * -\vec{r}\right)$

(c) $\left(\left(\cos\left(\frac{\pi}{4}\right), 0, 0, \sin\left(\frac{\pi}{4}\right)\right); \vec{r}\right) \sim \left(\left(\cos\left(\frac{\pi}{4}\right), 0, 0, \sin\left(\frac{\pi}{4}\right)\right); R_3 * (-\vec{r})\right)$ (C4)

where $q_0 = \cos\left(\frac{\omega}{2}\right)$, $q_3 = \sin\left(\frac{\omega}{2}\right)$, $R_1 = \mathbf{g}(\pi, [0 \quad 0 \quad 1])$, $R_2 = \mathbf{g}(\pi, [0 \quad 1 \quad 0])$,
$R_3 = \mathbf{g}\left(\frac{\pi}{2}, [1 \quad 0 \quad 0]\right)$

The equivalence relations in (a) and (b) suggest that the boundary inclination space (2-sphere) associated with boundary misorientation $(\omega, [0 \quad 0 \quad 1])$ and $\omega \in [0, \pi/2)$ has the symmetry C_{2v} or $mm2$ (illustrated in Figure C.3). The equivalence relation (c) needs to be considered in addition to (a) and (b) for the boundary inclination space corresponding to the misorientation $\left(\frac{\pi}{2}, [0 \quad 0 \quad 1]\right)$, which results in $D_{2d}(\bar{4} \, 2 \, m)$ symmetry on the 2-sphere. The equivalence between this z-axis boundary space and the 3-sphere can be established by using the parameters $(w, x, y, z) \in S^3$ such that

$$w = \frac{\sqrt{q_0^2 - \left(\cos\left(\frac{\omega_{max}}{2}\right)\right)^2}}{\sin\left(\frac{\omega_{max}}{2}\right)} \quad ; \quad \vec{v} = \begin{bmatrix} x \\ y \\ z \end{bmatrix} = \frac{1}{\sin\left(\frac{\omega_{max}}{2}\right)} \begin{bmatrix} r_1 \\ r_2 \\ r_3 \end{bmatrix} \text{ where } (w, x, y, z) \in S^3$$ (C5)

$$\mathcal{B} = S^3/E$$

(a) $(w, \vec{v}) \sim (w, \vec{v}')$ $\qquad \vec{v}' = g\left(\omega_{max}; \vec{b}_1\right) * \vec{v}$

(b) $(w, \vec{v}) \sim (w, -\vec{v}'')$ $\qquad \vec{v}'' = g\left(\pi; \vec{b}_2\right) * \vec{v}$

(c) $(w, \vec{v}) \sim (-w, -\vec{v}''')$ $\qquad \vec{v}''' = g\left(\frac{\omega_{max}}{2}; \vec{b}_1\right) * \vec{v}$

where $\omega_{max} = \pi$, $\vec{b}_1 = [0 \quad 0 \quad 1]$ and $b_2 = [1 \quad 0 \quad 0]$
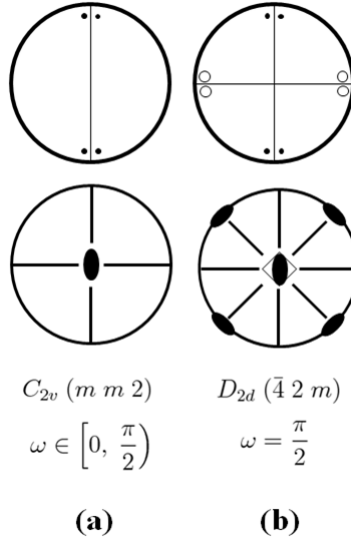
C_{2v} $(m\ m\ 2)$ $\qquad D_{2d}$ $(\bar{4}\ 2\ m)$

$\omega \in \left[0, \dfrac{\pi}{2}\right)$ $\qquad \omega = \dfrac{\pi}{2}$

(a) $\qquad\qquad$ (b)

Figure C.3 Symmetries associated with the boundary inclination space for crystals with point group symmetry D_2, (a) corresponding to any misorientation with angle $\omega \in [0, \pi/2)$ and misorientation axis $\vec{a} = [0\ 0\ 1]$, the boundary inclination space has the symmetry C_{2v}. (b) Corresponding to misorientation angle $\omega = \pi/2$, the boundary inclination space has the symmetry D_{2d}.

The x-axis boundary space is equivalent to the z-axis boundary space and is obtained by replacing $\vec{b}_1$ by $[1 \quad 0 \quad 0]$ and $\vec{b}_2$ by $[0 \quad 0 \quad 1]$. Similarly, the y-axis boundary space is obtained by replacing $\vec{b}_1$ by $[0 \quad 1 \quad 0]$ and $\vec{b}_2$ by $[0 \quad 0 \quad 1]$.

Similar analysis reveals the grain boundary space along the z-axis for crystals with point group D_n (where $n \in \{3,4,6\}$) to be equivalent to the quotient space S^3/E. This equivalence can be established by using the parameters $(w, x, y, z) \in S^3$ such that

$$w = \frac{\sqrt{q_0^2 - \left(\cos\left(\frac{\omega_{max}}{2}\right)\right)^2}}{\sin\left(\frac{\omega_{max}}{2}\right)} \quad ; \quad \vec{v} = \begin{bmatrix} x \\ y \\ z \end{bmatrix} = \frac{1}{\sin\left(\frac{\omega_{max}}{2}\right)} \begin{bmatrix} r_1 \\ r_2 \\ r_3 \end{bmatrix} \text{ where } (w, x, y, z) \in S^3$$

$$\boldsymbol{B} = S^3/E$$

(a) $(w, \vec{v}) \sim (w, \vec{v}')$ $\qquad \vec{v}' = \mathbf{g}\left(\omega_{max}; \vec{b}_1\right) * \vec{v}$ $\qquad\qquad$ (C6)

(b) $(w, \vec{v}) \sim (w, -\vec{v}'')$ $\qquad \vec{v}'' = \mathbf{g}\left(\pi; \vec{b}_2\right) * \vec{v}$

(c) $(w, \vec{v}) \sim (-w, -\vec{v}''')$ $\qquad \vec{v}''' = \mathbf{g}\left(\frac{\omega_{max}}{2}; \vec{b}_1\right) * \vec{v}$

where $\omega_{max} = \frac{2\pi}{n}$, $\vec{b}_1 = \begin{bmatrix} 0 & 0 & 1 \end{bmatrix}$ and $b_2 = \begin{bmatrix} 1 & 0 & 0 \end{bmatrix}$

The equivalence relations (a) and (b) suggest that the boundary inclination space (2-sphere) associated with boundary misorientation $(\omega, \begin{bmatrix} 0 & 0 & 1 \end{bmatrix})$ and $\omega \in [0, \pi/n)$ has the symmetry C_{nv}. Corresponding to the misorientation $\left(\frac{\pi}{n}, \begin{bmatrix} 0 & 0 & 1 \end{bmatrix}\right)$, the equivalence relation (c) needs to be considered in addition to (a) and (b), which results in $D_{3h}(\bar{6}\,m\,2)$, $D_{4d}(\bar{8}\,2\,m)$ and $D_{6d}(\overline{12}\,2\,m)$ symmetry for point groups D_3, D_4 and D_6 respectively (Figure C.4).
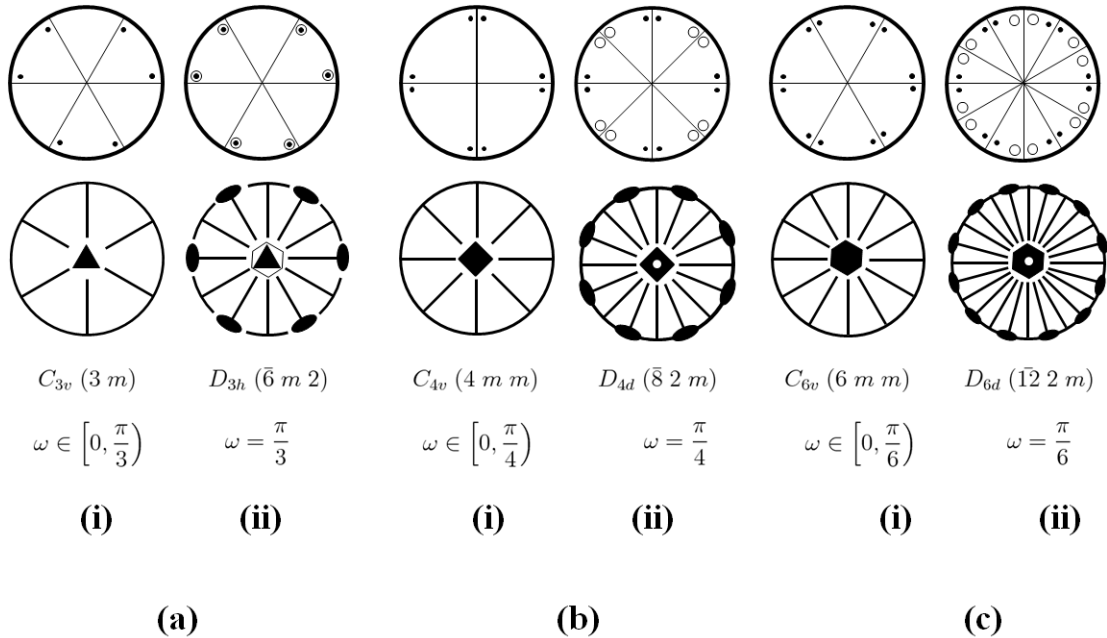
$C_{3v}\ (3\ m)$ $\qquad$ $D_{3h}\ (\bar{6}\ m\ 2)$ $\qquad$ $C_{4v}\ (4\ m\ m)$ $\qquad$ $D_{4d}\ (\bar{8}\ 2\ m)$ $\qquad$ $C_{6v}\ (6\ m\ m)$ $\qquad$ $D_{6d}\ (\overline{12}\ 2\ m)$

$\omega \in \left[0, \frac{\pi}{3}\right)$ $\quad$ $\omega = \frac{\pi}{3}$ $\quad$ $\omega \in \left[0, \frac{\pi}{4}\right)$ $\quad$ $\omega = \frac{\pi}{4}$ $\quad$ $\omega \in \left[0, \frac{\pi}{6}\right)$ $\quad$ $\omega = \frac{\pi}{6}$

(i) $\qquad$ **(ii)** $\qquad$ **(i)** $\qquad$ **(ii)** $\qquad$ **(i)** $\qquad$ **(ii)**

(a) $\qquad\qquad$ **(b)** $\qquad\qquad$ **(c)**

Figure C.4 Symmetries associated with the boundary inclination space for misorientations along the z-axis for crystals with point group D_n: (a) D_3 ($n = 3$), (b) D_4($n = 4$), and (c) D_6($n = 6$). (i) Corresponding to any misorientation with angle $\omega \in [0, \pi/n)$, the boundary inclination space has no symmetries (C_{nv}). (ii) Corresponding to misorientation angle $\omega = \pi/n$, the boundary inclination space has the symmetry D_{3h} ($n = 3$), D_{4d} ($n = 4$) and D_{6d} ($n = 6$).

In fact, the mapping from any high-symmetry axis grain boundary space to the 3-sphere can be classified into two categories: (i) Type I has symmetries that can be expressed as Equation (C3), where the parameters ω_{max} and $\vec{b}$ depend on the point group symmetry and (ii) Type II has symmetries that be expressed as Equation (C6) with variables ω_{max}, $\vec{b}_1$ and $\vec{b}_2$. These two types are mentioned in the equations below:

Type I Boundary Space with variables ω_{max} and $\vec{b}$

$$w = \frac{\sqrt{q_0^2 - \left(\cos\left(\frac{\omega_{max}}{2}\right)\right)^2}}{\sin\left(\frac{\omega_{max}}{2}\right)} \quad ; \quad \vec{v} = \begin{bmatrix} x \\ y \\ z \end{bmatrix} = \frac{1}{\sin\left(\frac{\omega_{max}}{2}\right)} \begin{bmatrix} r_1 \\ r_2 \\ r_3 \end{bmatrix} \text{ where } (w, x, y, z) \in S^3$$

$$\boldsymbol{B} = S^3/E$$

(C7)

(a) $(w, \vec{v}) \sim (w, \vec{v}')$ $\qquad \vec{v}' = \mathbf{g}\left(\omega_{max}; \vec{b}\right) * \vec{v}$

(b) $(w, \vec{v}) \sim (-w, -\vec{v}'')$ $\qquad \vec{v}'' = \mathbf{g}\left(\frac{\omega_{max}}{2}; \vec{b}\right) * \vec{v}$

Type II Boundary Space with variables ω_{max} and $\vec{b}_1, \vec{b}_2$

$$w = \frac{\sqrt{q_0^2 - \left(\cos\left(\frac{\omega_{max}}{2}\right)\right)^2}}{\sin\left(\frac{\omega_{max}}{2}\right)} \quad ; \quad \vec{v} = \begin{bmatrix} x \\ y \\ z \end{bmatrix} = \frac{1}{\sin\left(\frac{\omega_{max}}{2}\right)} \begin{bmatrix} r_1 \\ r_2 \\ r_3 \end{bmatrix} \text{ where } (w, x, y, z) \in S^3$$

$$\boldsymbol{B} = S^3/E$$

(C8)

(a) $(w, \vec{v}) \sim (w, \vec{v}')$ $\qquad \vec{v}' = \mathbf{g}\left(\omega_{max}; \vec{b}_1\right) * \vec{v}$

(b) $(w, \vec{v}) \sim (w, -\vec{v}'')$ $\qquad \vec{v}'' = \mathbf{g}\left(\pi; \vec{b}_2\right) * \vec{v}$

(c) $(w, \vec{v}) \sim (-w, -\vec{v}''')$ $\qquad \vec{v}''' = \mathbf{g}\left(\frac{\omega_{max}}{2}; \vec{b}_1\right) * \vec{v}$

The table below summarizes the mapping type and the symmetries of the grain boundary inclination space (2-sphere) for various point groups and high-symmetry axes.

Table C.1 Mappings for the grain boundary space with misorientations confined to a single high-symmetry axis in various point groups and crystal directions. The mappings corresponds to either Equation (C7) (Type I with variables $\omega_{max}, \vec{b}$) or Equation (C8) (Type II with variables $\omega_{max}, \vec{b}_1$ and $\vec{b}_2$).

Point Group	Symmetry Axes	Mapping (ω_{max})	$\vec{b}/(\vec{b}_1,\vec{b}_2)$	Symmetries for Inclination Space
C_1	$\forall\, \vec{a} \in S^2$	Type I (2π)	$\vec{b} = \vec{a}$	$C_1\big(\omega \in [0,\pi)\big)$ $\overline{2}(\omega = \pi)$
C_2	$\vec{a} = [0\,0\,1]$	Type I (π)	$\vec{b} = [0\,0\,1]$	$C_2\left(\omega \in \left[0,\frac{\pi}{2}\right)\right)$ $\overline{4}\left(\omega = \frac{\pi}{2}\right)$
C_3	$\vec{a} = [0\,0\,1]$	Type I $\left(\frac{2\pi}{3}\right)$	$\vec{b} = [0\,0\,1]$	$C_3\left(\omega \in \left[0,\frac{\pi}{3}\right)\right)$ $\overline{6}\left(\omega = \frac{\pi}{3}\right)$
C_4	$\vec{a} = [0\,0\,1]$	Type I $\left(\frac{\pi}{2}\right)$	$\vec{b} = [0\,0\,1]$	$C_4\left(\omega \in \left[0,\frac{\pi}{4}\right)\right)$ $\overline{8}\left(\omega = \frac{\pi}{4}\right)$
C_6	$\vec{a} = [0\,0\,1]$	Type I $\left(\frac{\pi}{3}\right)$	$\vec{b} = [0\,0\,1]$	$C_6\left(\omega \in \left[0,\frac{\pi}{6}\right)\right)$ $\overline{12}\left(\omega = \frac{\pi}{6}\right)$
D_2	$\vec{a} \in$ 2-fold Symmetry axes	Type II (π)	$\vec{b}_1 = \vec{a}$ $\vec{b}_2 = \begin{cases}[0\,0\,1] & if\ \vec{a} \neq [0\,0\,1] \\ [1\,0\,0] & if\ \vec{a} = [1\,0\,0]\end{cases}$	$C_{2v}\left(\omega \in \left[0,\frac{\pi}{2}\right)\right)$ $D_{2d}\left(\omega = \frac{\pi}{2}\right)$

D_3	$\vec{a} = [0\ 0\ 1]$ 3-fold Symmetry axes	Type II $\left(\frac{2\pi}{3}\right)$	$\vec{b}_1 = [0\ 0\ 1]$ $\vec{b}_2 = [1\ 0\ 0]$	$C_{3v}\left(\omega \in \left[0, \frac{\pi}{3}\right)\right)$ $D_{3h}\left(\omega = \frac{\pi}{3}\right)$
	$\vec{a} \in$ 2-fold Symmetry axes	Type I (π)	$\vec{b} = \vec{a}$	$C_2\left(\omega \in \left[0, \frac{\pi}{2}\right)\right)$ $\overline{4}\left(\omega = \frac{\pi}{2}\right)$
D_4	$\vec{a} = [0\ 0\ 1]$ 4-fold Symmetry axes	Type II $\left(\frac{\pi}{2}\right)$	$\vec{b}_1 = [0\ 0\ 1]$ $\vec{b}_2 = [1\ 0\ 0]$	$C_{4v}\left(\omega \in \left[0, \frac{\pi}{4}\right)\right)$ $D_{4d}\left(\omega = \frac{\pi}{4}\right)$
	$\vec{a} \in$ 2-fold Symmetry axes	Type II (π)	$\vec{b}_1 = \vec{a}$ $\vec{b}_2 = [0\ 0\ 1]$	$C_{2v}\left(\omega \in \left[0, \frac{\pi}{2}\right)\right)$ $D_{2d}\left(\omega = \frac{\pi}{2}\right)$
D_6	$\vec{a} = [0\ 0\ 1]$ 4-fold Symmetry axes	Type II $\left(\frac{\pi}{3}\right)$	$\vec{b}_1 = [0\ 0\ 1]$ $\vec{b}_2 = [1\ 0\ 0]$	$C_{6v}\left(\omega \in \left[0, \frac{\pi}{6}\right)\right)$ $D_{6d}\left(\omega = \frac{\pi}{6}\right)$
	$\vec{a} \in$ 2-fold Symmetry axes	Type II (π)	$\vec{b}_1 = \vec{a}$ $\vec{b}_2 = [0\ 0\ 1]$	$C_{2v}\left(\omega \in \left[0, \frac{\pi}{2}\right)\right)$ $D_{2d}\left(\omega = \frac{\pi}{2}\right)$
T	$\vec{a} \in$ 2-fold Symmetry axes	Type II (π)	$\vec{b}_1 = \vec{a}$ $\vec{b}_2 = \begin{cases}[0\ 0\ 1] & if\ \vec{a} \neq [0\ 0\ 1] \\ [1\ 0\ 0] & if\ \vec{a} = [1\ 0\ 0]\end{cases}$	$C_{2v}\left(\omega \in \left[0, \frac{\pi}{2}\right)\right)$ $D_{2d}\left(\omega = \frac{\pi}{2}\right)$

	$\vec{a} \in$ 3-fold Symmetry axes	Type I $\left(\frac{2\pi}{3}\right)$	$\vec{b} = \vec{a}$	$C_3\left(\omega \in \left[0, \frac{\pi}{3}\right)\right)$ $\overline{6}\left(\omega = \frac{\pi}{3}\right)$
O	$\vec{a} \in$ 4-fold Symmetry axes	Type II $\left(\frac{\pi}{2}\right)$	$\vec{b}_1 = \vec{a}$ $\vec{b}_2 = \begin{cases} [0\ 0\ 1] & if\ \vec{a} \neq [0\ 0\ 1] \\ [1\ 0\ 0] & if\ \vec{a} = [1\ 0\ 0] \end{cases}$	$C_{4v}\left(\omega \in \left[0, \frac{\pi}{4}\right)\right)$ $D_{4d}\left(\omega = \frac{\pi}{4}\right)$
	$\vec{a} \in$ 3-fold Symmetry axes	Type II $\left(\frac{2\pi}{3}\right)$	$\vec{b}_1 = \vec{a}$ $\vec{b}_2 = \begin{cases} [\overline{1}\ 1\ 0] & if\ \vec{a} = [1\ 1\ 1] \\ [1\ 1\ 0] & if\ \vec{a} = [\overline{1}\ 1\ 1] \\ [\overline{1}\ 1\ 0] & if\ \vec{a} = [\overline{1}\ \overline{1}\ 1] \\ [1\ 1\ 0] & if\ \vec{a} = [1\ \overline{1}\ 1] \end{cases}$	$C_{3v}\left(\omega \in \left[0, \frac{\pi}{3}\right)\right)$ $D_{3h}\left(\omega = \frac{\pi}{3}\right)$
	$\vec{a} \in$ 2-fold Symmetry axes	Type II (π)	$\vec{b}_1 = \vec{a}$ $\vec{b}_2 = \begin{cases} [0\ 0\ 1] & if\ a_3 = 0 \\ [0\ 1\ 0] & if\ a_2 = 0 \\ [1\ 0\ 0] & if\ a_1 = 0 \end{cases}$	$C_{2v}\left(\omega \in \left[0, \frac{\pi}{2}\right)\right)$ $D_{2d}\left(\omega = \frac{\pi}{2}\right)$

The symmetries of the grain boundary inclination space listed in the table above can be derived from the well-known bicrystal symmetries for grain boundaries [78, 107]. The purpose of deriving these symmetries in this appendix is to show the utility of the $(\mathbf{q}; \vec{r})$ parameterization and to present the mappings of these grain boundary spaces to the 3-sphere. We only considered the 11 point groups with rotational symmetry operations in this appendix. The symmetries of the grain boundary space for the remaining crystallographic point groups are obtained by considering the relations in Equation (1.10).

References

[1]   P. J. E. Forsyth, R. King, G. J. Metcalfe, and B. Chalmers, "Grain Boundaries in Metals," *Nature*, vol. 158, no. 4024, pp. 875-876, 1946.

[2]   C. W. Haynes and R. Smoluchowski, "Grain boundary diffusion in a body-centered cubic lattice," *Acta Metallurgica*, vol. 3, no. 2, p. 130–134, 1955.

[3]   J. P. Hirth, "The influence of grain boundaries on mechanical properties," *Metallurgical Transactions*, vol. 3, no. 12, pp. 3047-3067, 1972.

[4]   R. Smoluchowski, "Theory of Grain Boundary Diffusion," *Physical Review*, vol. 87, no. 3, p. 482, 1952.

[5]   T. Watanabe, "An approach to grain boundary design for strong and ductile polycrystals," *Res Mechanica*, vol. 11, no. 1, p. 47–84, 1984.

[6]   C. Cheung, U. Erb, and G. Palumbo, "Application of grain boundary engineering concepts to alleviate intergranular cracking in alloys 600 and 690," *Materials Science and Engineering: A*, vol. 185, no. 1-2, p. 39–43, 1994.

[7]   A. J. Schwartz, "The potential engineering of grain boundaries through thermomechanical processing," *Journal of the Minerals, Metals and Materials Society*, vol. 50, no. 2, p. 50–55, 1998.

[8]   I. Weiss and S. L. Semiatin, "Thermomechanical processing of alpha titanium alloys–an overview," *Materials Science and Engineering A*, vol. 263, no. 2, p. 243–256, 1999.

[9]   T. Watanabe and S. Tsurekawa, "The control of brittleness and development of desirable mechanical properties in polycrystalline systems by grain boundary engineering," *Acta Materialia*, vol. 47, no. 15-16, p. 4171–4185, 1999.

[10]   R. Ding, Z. X. Guo, and A. Wilson, "Microstructural evolution of a Ti-6Al-4V alloy during thermomechanical processing," *Materials Science and Engineering A*, vol. 327, no. 2, p. 233–245, 2002.

[11]   M. Michiuchi, H. Kokawa, Z. J. Wang, Y. S. Sato, and K. Sakai, "Twin-induced grain boundary engineering for 316 austenitic stainless steel," *Acta Materialia*, vol. 54, no. 19, p. 5179–5184, 2006.

[12]   L. Tan, K. Sridharan, and T. R. Allen, "Effect of thermomechanical processing on grain boundary character distribution of a Ni-based superalloy," *Journal of Nuclear Materials*, vol. 371, no. 1-3, p. 171–175, 2007.

[13]   T. Watanabe, S. Tsurekawa, X. Zhao, L. Zuo, and C. Esling, "A new challenge: grain boundary engineering for advanced materials by magnetic field application," *Journal of Materials Science*, vol. 41, no. 23, p. 7747–7759, 2006.

[14]   T. Watanabe, S. Tsurekawa, X. Zhao, and L. Zuo, "Grain boundary engineering by magnetic field application," *Scripta Materialia*, vol. 54, no. 6, p. 969–975, 2006.

[15]   W. Bollmann, *Crystal Defects and Crystalline Interfaces, 1970*. Berlin: Springer, 1982.

[16]   E. M. Lehockey, G. Palumbo, and P. Lin, "Improving the weldability and service performance of nickel-and iron-based superalloys by grain boundary engineering," *Metallurgical and Materials Transactions A*, vol. 29, no. 12, p. 3069–3079, 1998.

[17]   E. M. Lehockey and G. Palumbo, "On the creep behaviour of grain boundary engineered nickel," *Materials science & engineering. A, Structural materials: properties, microstructure and processing*, vol. 237, no. 2, p. 168–172, 1997.

[18]   E. M. Lehockey, D. Limoges, G. Palumbo, J. Sklarchuk, K. Tomantschger, and A. Vincze, "On improving the corrosion and growth resistance of positive Pb-acid battery grids by grain boundary engineering," *Journal of Power Sources*, vol. 78, no. 1-2, pp. 79-83, Mar. 1999.

[19]   D. P. Norton et al., "Epitaxial YBa2Cu3O7 on biaxially textured nickel (001): An approach to superconducting tapes with high critical current density," *Science*, vol. 274, no. 5288, p. 755, 1996.

[20]   L. Lu, R. Schwaiger, Z. W. Shan, M. Dao, K. Lu, and S. Suresh, "Nano-sized twins induce high rate sensitivity of flow stress in pure copper," *Acta materialia*, vol. 53, no. 7, p. 2169–2179, 2005.

[21]   M. Dao, L. Lu, Y. F. Shen, and S. Suresh, "Strength, strain-rate sensitivity and ductility of copper with nanoscale twins," *Acta materialia*, vol. 54, no. 20, p. 5421–5432, 2006.

[22]   L. Lu, X. Chen, X. Huang, and K. Lu, "Revealing the maximum strength in nanotwinned copper," *Science*, vol. 323, no. 5914, p. 607, 2009.

[23]   K. Lu, L. Lu, and S. Suresh, "Strengthening materials by engineering coherent internal boundaries at the nanoscale," *Science*, vol. 324, no. 5925, p. 349, 2009.

[24]   M. Kumar, W. E. King, and A. J. Schwartz, "Modifications to the microstructural topology in fcc materials through thermomechanical processing," *Acta Materialia*, vol. 48, no. 9, p. 2081–2091, 2000.

[25]   R. W. Minich, C. A. Schuh, and M. Kumar, "Role of topological constraints on the statistical properties of grain boundary networks," *Physical Review B*, vol. 66, no. 5, p. 52101, 2002.

[26]   M. Frary and C. A. Schuh, "Grain boundary networks: Scaling laws, preferred cluster structure, and their implications for grain boundary engineering," *Acta Materialia*, vol. 53, no. 16, p. 4323–4335, 2005.

[27]   X. Guo, "Physical origin of the intrinsic grain-boundary resistivity of stabilized-zirconia: role of the space-charge layers," *Solid State Ionics*, vol. 81, no. 3-4, p. 235–242, 1995.

[28]   S. E. Babcock and J. L. Vargas, "The nature of grain boundaries in the high-Tc superconductors," *Annual Review of Materials Science*, vol. 25, no. 1, p. 193–222, 1995.

[29]   H. Hilgenkamp and J. Mannhart, "Grain boundaries in high-Tc superconductors," *Reviews of Modern Physics*, vol. 74, no. 2, p. 485–549, 2002.

[30]   N. L. Peterson, "Grain-boundary diffusion in metals," *International Materials Reviews*, vol. 28, no. 1, p. 65–91, 1983.

[31]   R. W. Balluffi, "Grain boundary diffusion mechanisms in metals," *Metallurgical and Materials Transactions B*, vol. 13, no. 4, p. 527–553, 1982.

[32]   E. M. Lehockey, G. Palumbo, A. Brennenstuhl, and P. Lin, "Mitigating intergranular attack and growth in lead-acid battery electrodes for extended cycle and operating life," *Metallurgical and Materials Transactions A*, vol. 29, no. 1, p. 387–396, 1998.

[33]   B. Alexandreanu, B. H. Sencer, V. Thaveeprungsriporn, and G. S. Was, "The effect of grain boundary character distribution on the high temperature deformation behavior of Ni-16Cr-9Fe alloys," *Acta materialia*, vol. 51, no. 13, p. 3831–3848, 2003.

[34]   D. Bika and C. J. McMahon, others, "A model for dynamic embrittlement," *Acta Metallurgica et Materialia*, vol. 43, no. 5, p. 1909–1916, 1995.

[35]   C. A. Schuh, M. Kumar, and W. E. King, "Analysis of grain boundary networks and their evolution during grain boundary engineering," *Acta Materialia*, vol. 51, no. 3, p. 687–700, 2003.

[36]   A. J. Schwartz, W. E. King, and M. Kumar, "Influence of processing method on the network of grain boundaries," *Scripta materialia*, vol. 54, no. 6, p. 963, 2006.

[37]   M. von Heimendahl, W. Bell, and G. Thomas, "Applications of Kikuchi Line Analyses in Electron Microscopy," *Journal of Applied Physics*, vol. 35, no. 12, p. 3614, 1964.

[38]   B. L. Adams, S. I. Wright, and K. Kunze, "Orientation imaging: The emergence of a new microscopy," *Metallurgical Transactions A*, vol. 24, no. 4, pp. 819-831, 1993.

[39]   S. Schmidt, S. F. Nielsen, C. Gundlach, L. Margulies, X. Huang, and D. J. Jensen, "Watching the Growth of Bulk Grains During Recrystallization of Deformed Metals," *Science*, vol. 305, no. 5681, pp. 229 -232, Jul. 2004.

[40]   D. J. Jensen et al., "X-ray microscopy in four dimensions," *Materials Today*, vol. 9, no. 1-2, p. 18–25, 2006.

[41]   D. M. Saylor, A. Morawiec, and G. S. Rohrer, "Distribution of grain boundaries in magnesia as a function of five macroscopic parameters," *Acta materialia*, vol. 51, no. 13, p. 3663–3674, 2003.

[42]   C. S. Kim, A. D. Rollett, and G. S. Rohrer, "Grain boundary planes: New dimensions in the grain boundary character distribution," *Scripta materialia*, vol. 54, no. 6, p. 1005–1009, 2006.

[43]   S. Zaefferer, S. I. Wright, and D. Raabe, "Three-Dimensional Orientation Microscopy in a Focused Ion Beam–Scanning Electron Microscope: A New Dimension of Microstructure Characterization," *Metallurgical and Materials Transactions A*, vol. 39, no. 2, p. 374–389, 2008.

[44]   G. S. Rohrer, D. M. Saylor, B. S. El-Dasher, B. L. Adams, A. D. Rollett, and P. Wynblatt, "The distribution of internal interfaces in polycrystals," *Z. Metall*, vol. 95, p. 197–214, 2004.

[45]   G. S. Rohrer, V. Randle, C. S. Kim, and Y. Hu, "Changes in the five-parameter grain boundary character distribution in alpha-brass brought about by iterative thermomechanical processing," *Acta Materialia*, vol. 54, no. 17, p. 4489–4502, 2006.

[46]   G. S. Rohrer, "The distribution of grain boundary planes in polycrystals," *JOM Journal of the Minerals, Metals and Materials Society*, vol. 59, no. 9, p. 38–42, 2007.

[47]   V. Randle, "Role of grain boundary plane in grain boundary engineering," *Materials Science and Technology*, vol. 26, no. 7, p. 774–780, 2010.

[48]   D. M. Saylor, B. S. El Dasher, A. D. Rollett, and G. S. Rohrer, "Distribution of grain boundaries in aluminum as a function of five macroscopic parameters," *Acta Materialia*, vol. 52, no. 12, p. 3649–3655, 2004.

[49]   D. M. Saylor, B. Dasher, T. Sano, and G. S. Rohrer, "Distribution of grain boundaries in SrTiO3 as a function of five macroscopic parameters," *Journal of the American Ceramic Society*, vol. 87, no. 4, p. 670–676, 2004.

[50]   V. Randle, G. S. Rohrer, and Y. Hu, "Five-parameter grain boundary analysis of a titanium alloy before and after low-temperature annealing," *Scripta Materialia*, vol. 58, no. 3, p. 183–186, 2008.

[51]   V. Randle, G. S. Rohrer, H. M. Miller, M. Coleman, and G. T. Owen, "Five-parameter grain boundary distribution of commercially grain boundary engineered nickel and copper," *Acta Materialia*, vol. 56, no. 10, p. 2363–2373, 2008.

[52]   D. L. Olmsted, S. M. Foiles, and E. A. Holm, "Survey of computed grain boundary properties in face-centered cubic metals: I. Grain boundary energy," *Acta Materialia*, vol. 57, no. 13, p. 3694–3703, 2009.

[53]   G. S. Rohrer, J. Li, S. Lee, A. D. Rollett, M. Groeber, and M. D. Uchic, "Deriving grain boundary character distributions and relative grain boundary energies from three-dimensional EBSD data," *Materials Science and Technology*, vol. 26, no. 6, p. 661–669, 2010.

[54]   J. W. Cahn and J. E. Taylor, "Metrics, measures, and parametrizations for grain boundaries: a dialog," *Journal of Materials Science*, vol. 41, no. 23, p. 7669–7674, 2006.

[55]   D. L. Olmsted, E. A. Holm, and S. M. Foiles, "Survey of computed grain boundary properties in face-centered cubic metals–II: Grain boundary mobility," *Acta Materialia*, vol. 57, no. 13, p. 3704–3713, 2009.

[56]   H. Grimmer, "Disorientations and coincidence rotations for cubic lattices," *Acta Crystallographica Section A: Crystal Physics, Diffraction, Theoretical and General Crystallography*, vol. 30, no. 6, p. 685–688, 1974.

[57]   J. Stuelpnagel, "On the parametrization of the three-dimensional rotation group," *SIAM review*, vol. 6, no. 4, p. 422–430, 1964.

[58]   F. C. Frank, "Orientation mapping," *Metallurgical and Materials Transactions A*, vol. 19, no. 3, p. 403–408, 1988.

[59]   J. K. Mason and C. A. Schuh, "Hyperspherical harmonics for the representation of crystallographic texture," *Acta Materialia*, vol. 56, no. 20, p. 6141–6155, 2008.

[60]   J. K. Mason and C. A. Schuh, "Representations of Texture," in *Schwartz AJ, Kumar M, Adams BL, Field DP, editors. Electron Backscatter Diffraction in Materials Science.*, Springer, 2009, pp. 35-53.

[61]   M. Artin, "Linear Transformations," in *Algebra*, Prentice Hall, 1991, p. 123.

[62]   L. Euler, "Formulae generales pro translatione quacunque corporum rigidorum," *Novi Acad. Sci. Petrop*, vol. 20, p. 189–207, 1775.

[63]   H. J. Bunge, *Texture analysis in materials science: mathematical methods*. Butterworths, 1982.

[64]   B. T. M. Willis, "Use of a three-circle goniometer for diffraction measurements," *British Journal of Applied Physics*, vol. 13, p. 548, 1962.

[65]   R. J. Roe, "Description of crystallite orientation in polycrystalline materials. III. General solution to pole figure inversion," *Journal of Applied Physics*, vol. 36, no. 6, p. 2024–2031, 1965.

[66]   R. J. Roe, "Inversion of pole figures for materials having cubic crystal symmetry," *Journal of Applied Physics*, vol. 37, no. 5, p. 2069–2072, 1966.

[67]   M. Dahms and H. J. Bunge, "The iterative series-expansion method for quantitative texture analysis. I. General outline," *Journal of Applied Crystallography*, vol. 22, no. 5, pp. 439-447, 1989.

[68]   L. Euler, "Nova methodus motum corporum rigidorum determinandi," *Novi Commentari Academiae Scientiarum Imperialis Petropolitanae*, vol. 20, p. 208–238, 1775.

[69]   W. R. Hamilton, "On quaternions; or on a new system of imaginaries in Algebra," *Philosophical Magazine Series 3*, vol. 25, no. 169, p. 489–495, 1844.

[70]   A. Morawiec and J. Pospiech, "Some Information on Ouaternions Useful in Texture," *Textures and Microstructures*, vol. 10, p. 211–216, 1989.

[71]   P. Neumann, "Representation of orientations of symmetrical objects by Rodrigues vectors," *Textures and Microstructures*, vol. 14, no. 18, p. 53–8, 1991.

[72]   H. Grimmer, "A unique description of the relative orientation of neighbouring grains," *Acta Crystallographica Section A: Crystal Physics, Diffraction, Theoretical and General Crystallography*, vol. 36, no. 3, p. 382–389, 1980.

[73]   A. Heinz and P. Neumann, "Representation of orientation and disorientation data for cubic, hexagonal, tetragonal and orthorhombic crystals," *Acta Crystallographica Section A: Foundations of Crystallography*, vol. 47, no. 6, p. 780–789, 1991.

[74]   M. Humbert, N. Gey, J. Muller, and C. Esling, "Determination of a mean orientation from a cloud of orientations. Application to electron back-scattering pattern measurements," *Journal of applied crystallography*, vol. 29, no. 6, p. 662–666, 1996.

[75]   J. C. Glez and J. Driver, "Orientation distribution analysis in deformed grains," *Journal of applied crystallography*, vol. 34, no. 3, p. 280–288, 2001.

[76]   J. Munkres, *Topology*, 2nd ed. Prentice Hall, 2000.

[77]   A. Morawiec, "Models of uniformity for grain boundary distributions," *Journal of Applied Crystallography*, vol. 42, no. 5, p. 783–792, 2009.

[78]   R. C. Pond and D. S. Vlachavas, "Bicrystallography," *Proceedings of the Royal Society of London. A. Mathematical and Physical Sciences*, vol. 386, no. 1790, p. 95, 1983.

[79]   A. Morawiec and K. L. Merkle, "Symmetries of grain boundary distributions," in *Proceedings of the Third International Conference on Grain Growth. Warrendale (PA): TMS*, 1998, p. 509.

[80]   S. L. Altmann, "The Topology of Rotations," in *Rotations, quaternions, and double groups*, vol. 3, Clarendon Press Oxford, England:, 1986, pp. 164-174.

[81]   H. Hopf, "Systeme symmetrischer Bilinearformen und euklidische Modelle der projektiven Raüme," *Vjschr. naturf. Ges. Zurich*, vol. 85, p. 165–177, 1940.

[82]   R. Gilmore, *Lie groups, Lie algebras, and some of their applications*. Dover Publications, 2005.

[83]   E. P. Wigner, *Group Theory and Its Application to the Quantum Mechanics of Atomic Spectra*, Expanded & improved. Academic Press, 1959.

[84]   W. P. Thurston, "The structure of discrete groups," in *Three-Dimensional Geometry and Topology*, Princeton University Press, 1997, p. 209.

[85]   I. M. James, "3-dimensional topology up to 1960," in *History of Topology*, 1st ed., North Holland, 2006, p. 449.

[86]   G. E. Bredon, *Topology and Geometry*, Corrected. Springer, 1993.

[87]   E. J. Brody, "The topological classification of the lens spaces," *The Annals of Mathematics*, vol. 71, no. 1, p. 163–184, 1960.

[88]   W. Hantzsche, "Einlagerung von Mannigfaltigkeiten in euklidische Räume," *Mathematische Zeitschrift*, vol. 43, no. 1, p. 38–58, 1938.

[89]   M. W. Hirsch, "On imbedding differentiable manifolds in euclidean space," *The Annals of Mathematics*, vol. 73, no. 3, p. 566–571, 1961.

[90]   H. S. M. Coxeter, *Introduction to Geometry*, 2nd ed. Wiley, 1989.

[91]   J. J. Rotman, "Some basic topological notions," in *An Introduction to Algebraic Topology*, Springer, 1988, p. 23.

[92]   R. Kirby, "WHAT IS... Boy's Surface?," *Notices-American Mathematical Society*, vol. 54, no. 10, p. 1306, 2007.

[93]   A. Morawiec, "Misorientation-Angle Distribution of Randomly Oriented Symmetric Objects," *Journal of Applied Crystallography*, vol. 28, no. 3, pp. 289-293, 1995.

[94] U. F. Kocks, C. N. Tomé, H.-R. Wenk, and H. Mecking, *Texture and anisotropy: preferred orientations in polycrystals and their effect on materials properties*. Cambridge University Press, 2000.

[95] B. Botvinnik and S. Preston, "Conformal Laplacian and Conical Singularities," in *High-dimensional manifold topology: proceedings of the School, ICTP, Trieste, Italy, 21 May-8 June 2001*, 2003, p. 22.

[96] A. F. Nikiforov, V. B. Uvarov, and R. P. Boas, *Special functions of mathematical physics*. Birkhäuser, 1988.

[97] N. C. Popa, "Texture in Rietveld refinement," *Journal of applied crystallography*, vol. 25, no. 5, p. 611–616, 1992.

[98] D. M. Saylor, A. Morawiec, and G. S. Rohrer, "Distribution and energies of grain boundaries in magnesia as a function of five degrees of freedom," *Journal of the American Ceramic Society*, vol. 85, no. 12, p. 3081–3083, 2002.

[99] D. M. Saylor, B. S. El-Dasher, B. L. Adams, and G. S. Rohrer, "Measuring the five-parameter grain-boundary distribution from observations of planar sections," *Metallurgical and Materials Transactions A*, vol. 35, no. 7, p. 1981–1989, 2004.

[100] C. S. Kim, Y. Hu, G. S. Rohrer, and V. Randle, "Five-parameter grain boundary distribution in grain boundary engineered brass," *Scripta materialia*, vol. 52, no. 7, p. 633–637, 2005.

[101] V. Randle, "'Five-parameter'analysis of grain boundary networks by electron backscatter diffraction," *Journal of microscopy*, vol. 222, no. 2, p. 69–75, 2006.

[102] V. Randle, "Application of electron backscatter diffraction to grain boundary characterisation," *International Materials Reviews*, vol. 49, no. 1, p. 1–11, 2004.

[103] G. M. Pennock, M. Coleman, M. R. Drury, and V. Randle, "Grain boundary plane populations in minerals: the example of wet NaCl after low strain deformation," *Contributions to Mineralogy and Petrology*, vol. 158, no. 1, p. 53–67, 2009.

[104] A. J. Schwartz and M. Kumar, "Measurement of the Five-Parameter Grain Boundary Distribution from Planar Sections," in *Electron Backscatter Diffraction in Materials Science*, Springer, 2009, pp. 215-229.

[105] G. S. Rohrer, "Measuring and Interpreting the Structure of Grain-Boundary Networks," *Journal of the American Ceramic Society*.

[106] J. K. Mason, "The relationship of the hyperspherical harmonics to SO (3), SO (4) and orientation distribution functions," *Acta Crystallographica Section A: Foundations of Crystallography*, vol. 65, no. 4, p. 259–266, 2009.

[107] G. L. Kalonji, "Symmetry principles in the physics of crystalline interfaces," Massachusetts Institute of Technology, 1982.